MIT Libraries | DSpace@MIT

MIT Open Access Articles

Lineage tracing reveals the phylodynamics, plasticity, and paths of tumor evolution

Massachusetts Institute of Technology

Lineage tracing reveals the phylodynamics, plasticity, and paths of tumor evolution

Graphical abstract
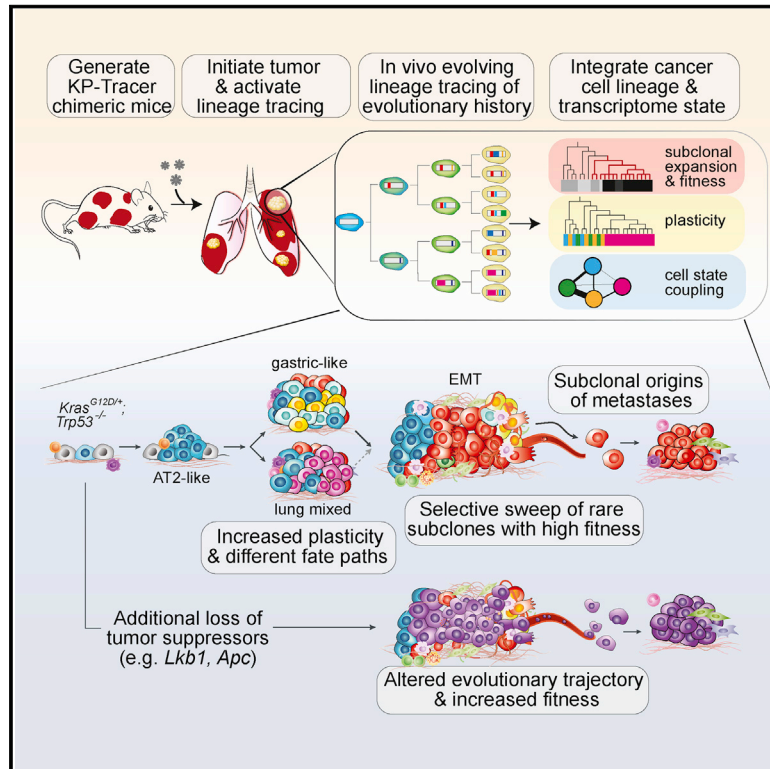
Authors

Dian Yang, Matthew G. Jones, Santiago Naranjo, ..., Nir Yosef, Tyler Jacks, Jonathan S. Weissman

Correspondence

niryosef@berkeley.edu (N.Y.), tjacks@mit.edu (T.J.), weissman@wi.mit.edu (J.S.W.)

In brief

Yang et al. developed a genetically engineered mouse model of lung cancer capable of continuous lineage tracing with single-cell RNA-seq readout. They identified the subclonal dynamics of tumors, gene modules underlying expansion, transient increases in cellular plasticity, stereotypical evolutionary paths to aggressiveness across tumor genotypes, and the spatial and phylogenetic origins of metastases.

Highlights

- KP-tracer mice enable continuous, high-resolution *in vivo* cancer lineage tracing

- Rare subclones with distinct expression programs expand during tumor evolution

- Lineage tracing reveals cellular plasticity and evolutionary paths

- Metastases are derived from spatially localized, expanding subclones of the tumor

Cell

Article

Lineage tracing reveals the phylodynamics, plasticity, and paths of tumor evolution

Dian Yang,[1,2,3,7,27] Matthew G. Jones,[1,2,3,4,5,6,7,27] Santiago Naranjo,[7,8] William M. Rideout III,[7] Kyung Hoi (Joseph) Min,[3,7,9] Raymond Ho,[1,2,3,7] Wei Wu,[10,11] Joseph M. Replogle,[1,2,3,12,13] Jennifer L. Page,[14] Jeffrey J. Quinn,[1,2,28] Felix Horns,[15] Xiaojie Qiu,[1,2,3,7] Michael Z. Chen,[3,16] William A. Freed-Pastor,[7,17] Christopher S. McGinnis,[13,18] David M. Patterson,[18,29] Zev J. Gartner,[18,19,20] Eric D. Chow,[21,22] Trever G. Bivona,[10,11] Michelle M. Chan,[23,24] Nir Yosef,[6,19,25,26,*] Tyler Jacks,[7,8,*] and Jonathan S. Weissman[1,2,3,7,8,30,*]

[1]Department of Cellular and Molecular Pharmacology, University of California, San Francisco, San Francisco, CA 94158, USA
[2]Howard Hughes Medical Institute, Massachusetts Institute of Technology, Cambridge, MA 02142, USA
[3]Whitehead Institute for Biomedical Research, Massachusetts Institute of Technology, Cambridge, MA 02142, USA
[4]Biological and Medical Informatics Graduate Program, University of California, San Francisco, San Francisco, CA 94158, USA
[5]Integrative Program in Quantitative Biology, University of California, San Francisco, San Francisco, CA 94158, USA
[6]Center for Computational Biology, University of California, Berkeley, Berkeley, CA 94720, USA
[7]David H. Koch Institute for Integrative Cancer Research, Massachusetts Institute of Technology, Cambridge, MA 02142, USA
[8]Department of Biology, Massachusetts Institute of Technology, Cambridge, MA 02142, USA
[9]Department of Electrical Engineering and Computer Science, Massachusetts Institute of Technology, Cambridge, MA 02142, USA
[10]Department of Medicine, University of California, San Francisco, San Francisco, CA 94158, USA
[11]Helen Diller Family Comprehensive Cancer Center, University of California, San Francisco, San Francisco, CA 94158, USA
[12]Medical Scientist Training Program, University of California, San Francisco, San Francisco, CA 94158, USA
[13]Tetrad Graduate Program, University of California, San Francisco, San Francisco, CA 94158, USA
[14]Cell and Genome Engineering Core, University of California San Francisco, San Francisco, CA 94158, USA
[15]Division of Biology and Biological Engineering, California Institute of Technology, Pasadena, CA 91125, USA
[16]Medical Scientist Training Program, Harvard Medical School, Boston, MA 02115, USA
[17]Department of Medical Oncology, Dana-Farber Cancer Institute, Harvard Medical School, Boston, MA 02215, USA
[18]Department of Pharmaceutical Chemistry, University of California, San Francisco, San Francisco, CA 94158, USA
[19]Chan Zuckerberg BioHub Investigator, University of California, San Francisco, San Francisco, CA 94158, USA
[20]Center for Cellular Construction, University of California, San Francisco, San Francisco, CA 94158, USA
[21]Department of Biochemistry and Biophysics, University of California, San Francisco, San Francisco, CA 94158, USA
[22]Center for Advanced Technology, University of California, San Francisco, San Francisco, CA 94158, USA
[23]Lewis-Sigler Institute for Integrative Genomics, Princeton University, Princeton, NJ 08544, USA
[24]Department of Molecular Biology, Princeton University, Princeton, NJ 08544, USA
[25]Department of Electrical Engineering and Computer Science, University of California Berkeley, Berkeley, CA 94720, USA
[26]Ragon Institute of Massachusetts General Hospital, MIT and Harvard University, Cambridge, MA, USA
[27]These authors contributed equally
[28]Present address: Inscripta Inc., Boulder, CO 80301, USA
[29]Present address: 10X Genomics Inc., Pleasanton, CA 94566, USA
[30]Lead contact
*Correspondence: niryosef@berkeley.edu (N.Y.), tjacks@mit.edu (T.J.), weissman@wi.mit.edu (J.S.W.)
https://doi.org/10.1016/j.cell.2022.04.015

SUMMARY

Tumor evolution is driven by the progressive acquisition of genetic and epigenetic alterations that enable uncontrolled growth and expansion to neighboring and distal tissues. The study of phylogenetic relationships between cancer cells provides key insights into these processes. Here, we introduced an evolving lineage-tracing system with a single-cell RNA-seq readout into a mouse model of *Kras;Trp53*(KP)-driven lung adenocarcinoma and tracked tumor evolution from single-transformed cells to metastatic tumors at unprecedented resolution. We found that the loss of the initial, stable alveolar-type2-like state was accompanied by a transient increase in plasticity. This was followed by the adoption of distinct transcriptional programs that enable rapid expansion and, ultimately, clonal sweep of stable subclones capable of metastasizing. Finally, tumors develop through stereotypical evolutionary trajectories, and perturbing additional tumor suppressors accelerates progression by creating novel trajectories. Our study elucidates the hierarchical nature of tumor evolution and, more broadly, enables in-depth studies of tumor progression.

INTRODUCTION

Cancer is an evolutionary process characterized by the dynamic interplay of cellular subpopulations, each driven by progressive genetic and epigenetic changes (Nowell, 1976). Throughout this process, cancer cells can acquire phenotypic heterogeneity that increases fitness by enabling them to grow more aggressively, invade neighboring tissues, evade the immune system and therapeutic challenges, and metastasize to distant sites (Hanahan and Weinberg, 2011; Vogelstein et al., 2013; McGranahan and Swanton, 2017). Interrogating the molecular bases of subclonal selection and metastatic seeding, the origins of and transitions between transcriptional states as well as the identities and genetic determinants of evolutionary paths that tumors undergo will not only illuminate fundamental principles governing tumor evolution but also have immediate clinical implications (Black and McGranahan, 2021). To fully understand these processes, it is essential to study the evolutionary dynamics giving rise to a tumor in its native setting, preferably in experimentally defined conditions (Amirouchene-Angelozzi et al., 2017).

Tumor phylogenetic analysis, the study of lineage relationships among the cells comprising the tumor population descended from a single-transformed progenitor, can provide key insights into the dynamics of tumor progression. Classically, phylogenies have been constructed using naturally occurring somatic genomic variations (mutations or copy number variations [CNVs]) as natural lineage tracers. These efforts have illuminated several key evolutionary processes underpinning tumor development (Vogelstein et al., 1988; Sjöblom et al., 2006; Schwartz and Schäffer, 2017; Ludwig et al., 2019; Gao et al., 2021; Gerstung et al., 2020; Sottoriva et al., 2015), including the acquisition of critical subclonal genetic or epigenetic changes (Gerlinger et al., 2014; Williams et al., 2018; Neftel et al., 2019), the timing and routes of metastatic dissemination (Turajlic and Swanton, 2016; Hu and Curtis, 2020), and the development of therapeutic resistance (Maynard et al., 2020; Powles et al., 2021; Abbosh et al., 2017; Kim et al., 2018; Salehi et al., 2021). Although progress has been enabled by innovative computational methods (Potter et al., 2013; El-Kebir et al., 2016; Malikic et al., 2019; Satas et al., 2020), these studies are limited by the inherent variation in naturally occurring somatic mutations, incomplete or low cell sampling, and other confounding variables (e.g. environmental exposures and genetic background) and are not amenable to further perturbations or functional studies.

Genetically engineered mouse models (GEMMs) of cancer provide a critical tool for modeling tumor progression as they allow one to study tumor evolution in its native microenvironment and experimentally defined conditions (Hann and Balmain, 2001; Frese and Tuveson, 2007). The $Kras^{LSL-G12D/+}$; $Trp53^{fl/fl}$ (KP) model of lung adenocarcinoma allows tumor initiation via viral delivery of Cre recombinase to a small number of lung epithelial cells, leading to activation of oncogenic Kras, homozygous deletion of the p53 tumor suppressor gene, and clonal tumor outgrowth. It faithfully models the major steps of tumor evolution from nascent cell transformation to aggressive metastasis, recapitulating human lung adenocarcinoma progression both molecularly and histopathologically (Jackson et al., 2001; Jackson et al., 2005; Winslow et al., 2011). Moreover, recent work has re-

vealed that substantial transcriptomic and epigenomic heterogeneities emerge during tumor evolution in this model (Marjanovic et al., 2020; LaFave et al., 2020), consistent with human tumors (Laughney et al., 2020). The tractability of this model provides an appealing opportunity to probe several unanswered but crucial questions regarding how tumors evolve including the following: how a single-transformed cell expands into an aggressive tumor, how various cell states relate to one another and contribute to tumor evolution, how different transcriptional states transition between each other, and how metastases and primary tumors are evolutionarily related.

Approaches that permit simultaneous measurements of cell lineage and cell state information have the potential to provide unique insights into these questions (Tammela and Sage, 2020; Wagner and Klein, 2020; Stadler et al., 2021). Although previous studies have used synthetic "static" barcoding techniques to study clonal relationships (Bhang et al., 2015; Livet et al., 2007; Lan et al., 2017; Pei et al., 2017; Driessens et al., 2012; Schepers et al., 2012), studying the evolution of individual tumors at subclonal resolution remains challenging. This limitation is in large part due to the low mutational burden in GEMM tumors, thus offering little lineage resolution within individual tumors (Westcott et al., 2015; McFadden et al., 2016). The recent development of high-resolution CRISPR/Cas9-evolving lineage tracing paired with single-cell RNA-seq (scRNA-seq) readouts overcomes these limitations. Generally, such continuous lineage-tracing approaches leverage Cas9-induced DNA cleavage and subsequent repair to progressively generate heritable insertions and deletions ("indels") at synthetic DNA target sites engineered into the genomes of living cells (McKenna et al., 2016; Frieda et al., 2017; Kalhor et al., 2018; Chan et al., 2019; McKenna and Gagnon, 2019). Importantly, these DNA target sites are transcribed into polyadenylated mRNAs, allowing them to be captured and profiled along with all other cellular mRNAs using scRNA-seq. In doing so, this approach makes it possible to directly link the current cell state (as measured by scRNA-seq) with its inferred or putative past lineage history (as captured by the lineage tracer) and to do so on a massive scale (Alemany et al., 2018; Spanjaard et al., 2018; Raj et al., 2018; Chan et al., 2019; Bowling et al., 2020). Recently, this technology has been introduced into cancer cell lines before transplanting them into mice to track metastatic behaviors in vivo (Simeonov et al., 2021; Quinn et al., 2021; Zhang et al., 2021).

Here, we have developed an autochthonous "KP-Tracer" mouse model that allows us to simultaneously initiate an engineered lineage-tracing system and induce Kras and Trp53 oncogenic mutations in individual lung epithelial cells. This enabled continuous and comprehensive monitoring of the processes by which a single-cell harboring oncogenic mutations evolves into an aggressive tumor. The resulting tumor phylogenies reveal that rare subclones drive tumor expansion by adopting distinct fitness-associated transcriptional programs. By integrating lineage and transcriptome data, we uncovered changes in cancer cell plasticity and parallel evolutionary paths of tumor evolution in this model, which could be profoundly altered by perturbing additional tumor suppressor genes commonly mutated in human tumors. We have also identified the subclonal origins, spatial locations, and cellular states of metastatic progression.

Collectively, this technology allowed us to reconstruct the lifespan of a tumor from a single-transformed cell to a complex and aggressive tumor population at unprecedented scale and resolution.

RESULTS

KP-Tracer mouse enables continuous and high-resolution lineage tracing of tumor initiation and progression

To generate high-resolution tumor phylogenies, we developed a lineage-tracing competent mouse model of lung adenocarcinoma capable of months-long continuous cell lineage tracing (Figure 1A). Specifically, we engineered mouse embryonic stem cells (mESCs) harboring the conditional alleles $Kras^{LSL-G12D/+}$ and $Trp53^{fl/fl}$ (KP) to additionally encode conditional SpCas9 and mNeonGreen fluorophore at the Rosa26 locus; $Rosa26^{LSL-Cas9-P2A-mNeonGreen}$ (KPCas9). We then engineered these mESCs with a refined version of our lineage-tracing technology (Chan et al., 2019; Quinn et al., 2021). Specifically, we introduced a library of piggyBac transposon-based lineage-tracing vector containing two essential components: first, target sites for lineage tracing, consisting of three cut sites positioned within the 3′ UTR of a mCherry fluorescent reporter and a 14-base-pair randomer integration barcode ("intBC") to distinguish individual copies; second, three constitutively expressed single-guide RNAs (sgRNAs) for directing Cas9 to each of the three individual cut sites within the target sites, thereby generating indels for lineage tracing (Figure S1A). A key enabling feature is that the speed of tracing (i.e., indel generation kinetics) can be tuned to match the tumor developmental timescale by engineering mismatches between sgRNAs and target sites (Chan et al., 2019; Quinn et al., 2021). We isolated engineered mESC clones by fluorescence-activated cell sorting (FACS) based on high mCherry expression (Figures S1B and S1C) and selected clones with 10–30 integrated target sites by quantitative PCR (qPCR) and DNA sequencing (Figures S1D and S1E). Finally, we generated chimeric mice (hereafter "KP-Tracer" mice) from five validated mESC clones to ensure that evolutionary behavior was not idiosyncratic to a specific clone (Zhou et al., 2010; Premsrirut et al., 2011).

In KP-Tracer mice, intratracheal administration of lentivirus expressing Cre recombinase simultaneously initiates lung tumors by activating conditional oncogenic alleles and lineage tracing by inducing the expression of Cas9 that, together with the expressed sgRNAs, causes accumulation of indels in the target sites (DuPage et al., 2009). Previous static lineage tracing studies, using lentiviral barcoding or multicolor reporters, have shown that KP tumors induced with this strategy are clonal and homogenously contain oncogenic Kras;p53 mutations (Chuang et al., 2017; Caswell et al., 2014). To validate tumor clonality, we induced tumors with a barcoded lentiviral-Cre construct (lenti-Cre-BC) providing a unique clonal barcode for each tumor (Adamson et al., 2016).

Individual tumors with strong mCherry and mNeonGreen expression (indicating target site and Cre, respectively) and clear boundary separation from adjacent tumors were harvested 5–6 months after tumor initiation, microdissected, and dissoci-

ated completely to ensure unbiased cell sampling (Figure 1B; Table S1). After being labeled with Multiplexing Using Lipid-Tagged Indices for scRNA-seq (MULTI-seq) (McGinnis et al., 2019) and purified by FACS (STAR Methods), cancer cells were subjected to scRNA-seq analysis to measure cell state, lineage, sample identity, and tumor clonality. After integrating all four datasets for each cell (Figure 1C; STAR Methods), we proceeded with paired lineage and transcriptome measurements for 40,386 cells with a median of 9,680 UMIs and 2,877 genes detected across 35 tumors (29 primary tumors and 6 metastases; a median of 511 cells were detected per primary tumor). Importantly, target sites were consistently expressed across tumors (Figures 1D, S1F, and S1G).

After preprocessing target site data based on lineage-tracing sequencing quality control and ensuring tumor clonality with lenti-Cre-BC information (Figure 1C; STAR Methods), we reconstructed phylogenies for each tumor with Cassiopeia (Jones et al., 2020). Figure 1E displays the inferred phylogeny and its corresponding indel status (summarized in an "allele heatmap") of a single-representative tumor, consisting of 772 cells. The resulting tree revealed a rich subclonal structure and deep lineage relationships, with a median depth of 12 and a maximum depth of 15. As a validation of the integrity of our lineage reconstruction, we observed strong correlations between phylogenetic and allelic distances across our trees (Figure 1F; Table S1). With these high-resolution tumor phylogenies, we next turned to studying the relationship between subclonal dynamics and cellular state as determined by gene expression.

Rare subclones expand during tumor progression, marked by increased DNA copy number variation, cell-cycle score, and fitness score

A key question in tumor evolution is how subclonal selection, based on the acquisition of growth-promoting genetic or epigenetic changes, and the resulting population dynamics lead to the expansion of aggressive subclones relative to other parts of the same tumor (Nowell, 1976; McGranahan and Swanton, 2017; Davis et al., 2017; Sottoriva et al., 2015). To examine the subclonal dynamics in KP tumors, we adapted a statistical test that compares the relative size of each subclone with what would be expected in a "neutral" model of evolution where no subclone is under selection (STAR Methods (Griffiths and Tavaré, 1998; Speidel et al., 2019)). Using this method on a high-quality subset (21/29) of primary tumors (Figure S1H; STAR Methods), we found examples of tumors that appeared to be neutrally evolving (i.e., with no evidence for positive selection) and tumors with subclones showing clear signs of positive selection (Figure 2A). Tumors predominantly had one or sometimes two subclones undergoing expansion, and across tumors, there was a broad distribution in the proportion of cells within expansions (Figure 2B). The proportion of expanding cells in each tumor was poorly explained by individual technical covariates, including the age of the tumor ($R^2 = 0.25 \pm 0.14$), the depth of the tumor phylogeny ($R^2 = 0.23 \pm 0.15$), the number of cells in the tumor ($R^2 = 0.09 \pm 0.07$), and the proportion of unique cell lineage states ($R^2 = 0.28 \pm 0.15$, Figures S2A–S2D), although an additive linear model with all of these covariates was a stronger predictor ($R^2 = 0.52$).
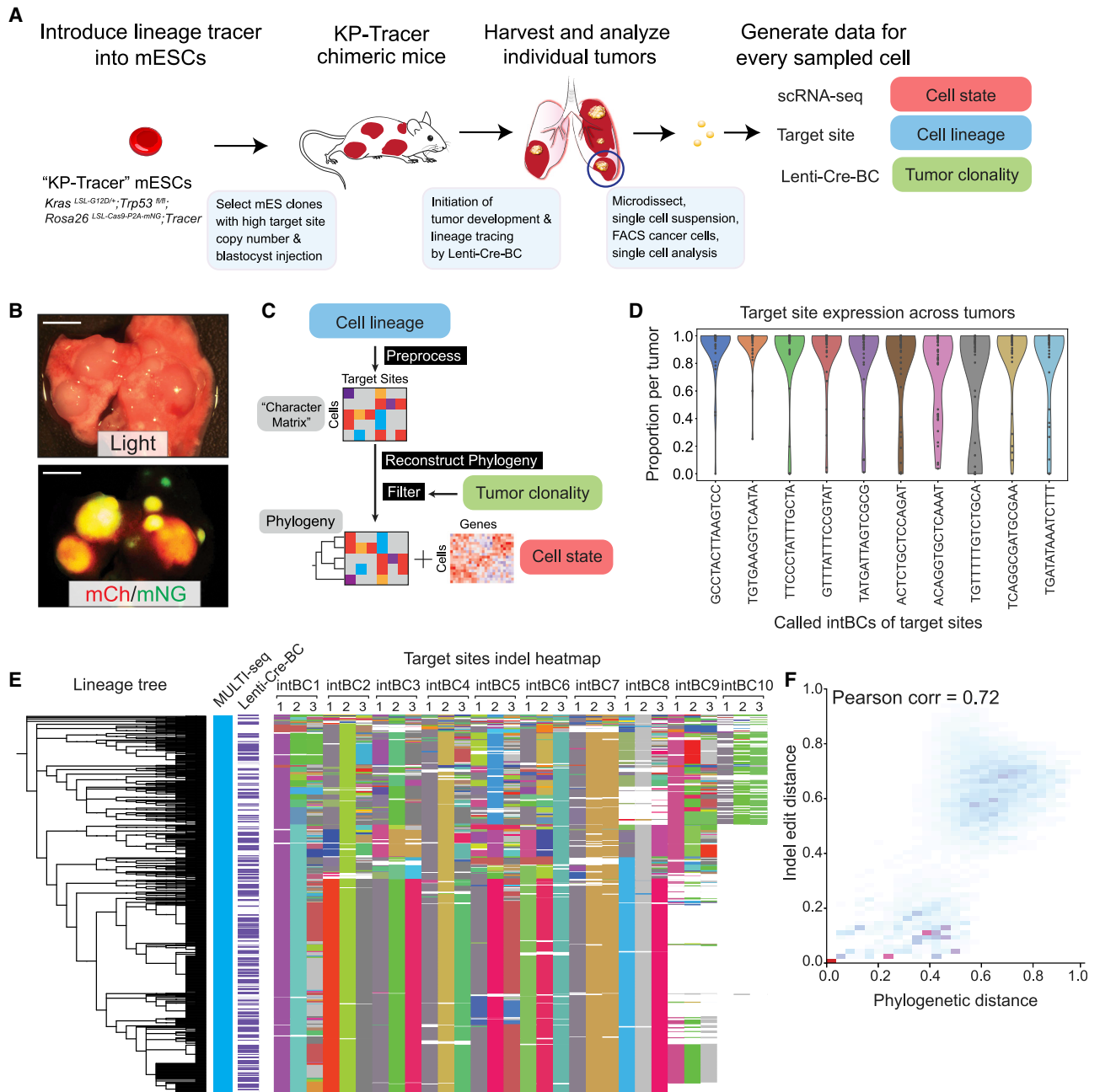
Figure 1. KP-Tracer mouse enables continuous and high-resolution lineage tracing of tumor initiation and progression

(A) Generation of the KP-Tracer chimeric mouse and initiation of KP-Tracer tumors (STAR Methods). Five to six months after tumor initiation, individual tumors are dissociated into single-cell suspension and single-cell sequencing libraries are prepared.

(B) Representative images of tumors from KP-Tracer mouse. Tumors are positive for mCherry and mNeonGreen. Scale bars, 5 mm.

(C) Tumor lineage reconstruction data analysis pipeline.

(D) Target site capture efficiency across tumors from mice generated from one representative mESC clone (2E1). Dots represent the average capture rate of a specific target site in a tumor.

(E) Phylogeny with MULTI-seq, lenti-Cre-BC, and target site information for an example tumor. Each row represents a single cell, and each column indicates barcode or target site information (ordered by the percentage of target sites detected across cells). Unique colors represent unique barcodes or indels, uncut sites are shown in light gray, and missing data are indicated in white.

(F) Comparison of phylogenetic distance (from the reconstructed tree) and allele edit distance (from target sites) for the example tumor in (E).
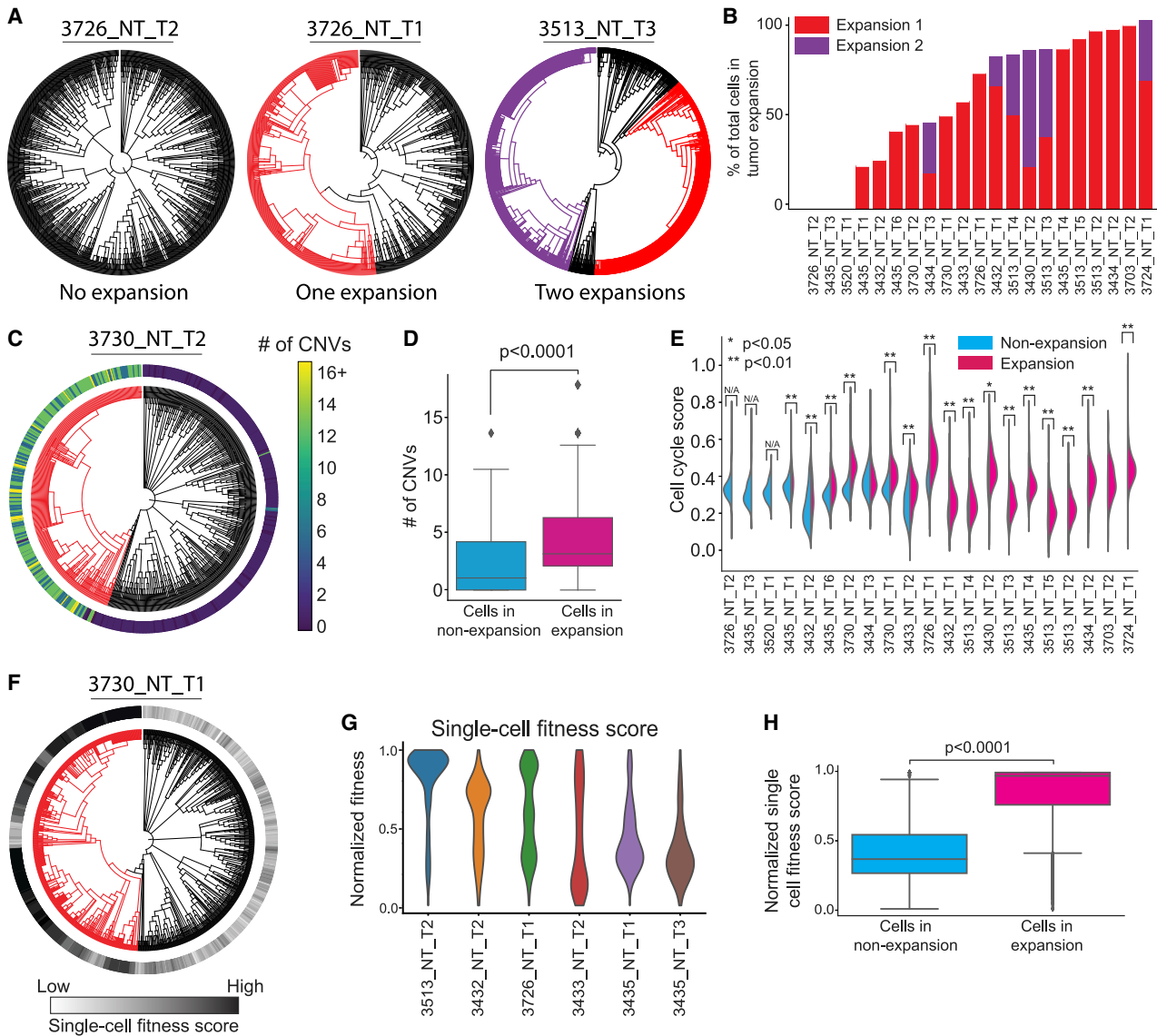
See also Figure S1 and Table S1.

Figure 2. Rare subclones expand during tumor progression, marked by increased DNA copy number variation, cell-cycle score, and fitness score

(A) Example tumor phylogenies with expansions highlighted with red or purple branches.

(B) The number of expansions and percentage of expanding cells across tumors. Tumors are ranked by the total percentage of cells in expanding subclones.

(C) CNV numbers per cell (outer bar) in expanding (red) versus nonexpanding (black) cells of an example tumor.

(D) Comparison of CNV number per cell in expansions versus nonexpansions (permutation test, p < 0.0001).

(E) Comparison of cell-cycle transcriptional scores of cells from the expanding and nonexpanding subclones (two-sided Mann-Whitney U test, * p < 0.05, ** p < 0.01). Tumors without expansions are labeled as N/A.

(F–H) Phylogenetic single-cell fitness scores in expansions.

(F) A representative tumor phylogeny with single-cell fitness scores overlaid.

(G) Single-cell fitness scores in representative tumors.

(H) Cancer cells from expansions have significantly higher single-cell fitness scores (two-sided Mann-Whitney U test, p < 0.0001).

See also Figure S2.

Several lines of evidence support the accuracy of the inferred phylogenies and subclonal dynamics. First, lineage trees inferred by an alternative phylogenetic reconstruction algorithm, Neighbor Joining, revealed consistent subclonal expansion proportions (Saitou and Nei, 1987; Pearson's ρ = 0.87, Figure S2E). Second,

copy number variation (CNV)—a common feature for inferring subclonal structure in tumors (Tarabichi et al., 2021)—corroborated tumor subclonal structure. Specifically, despite the low-resolution lineages inferred from detected CNVs, in the majority of tumors (20/21), the relationships from subclonal CNVs were
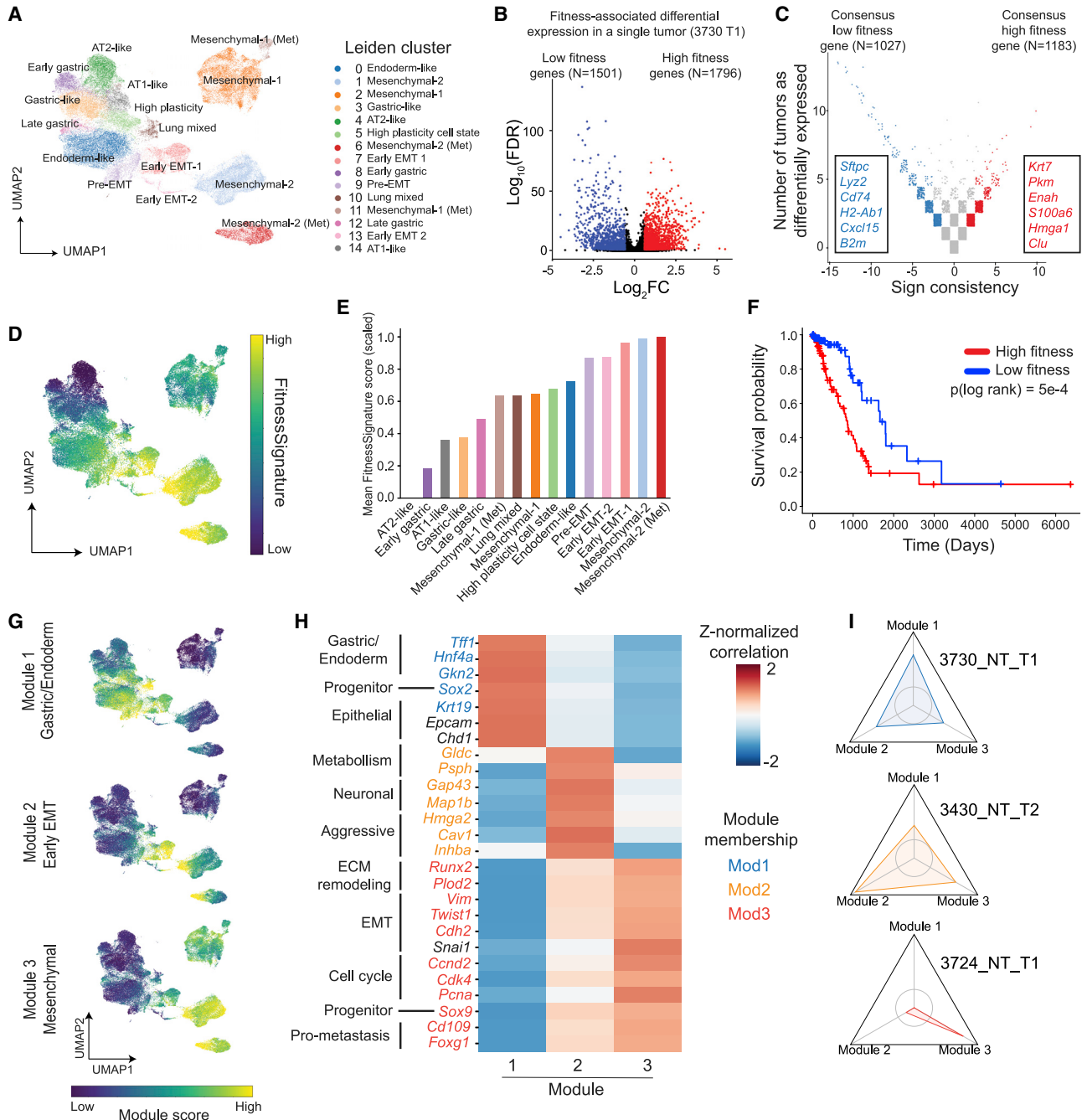
Figure 3. Integration of phylodynamics and transcriptome uncovers fitness-associated gene programs for KP tumors

(A) Gene expression UMAP (McInnes et al., 2018) and clustering of cancer cells from KP-Tracer tumors.

(B and C) Identification of a transcriptional FitnessSignature.

(B) Differential expression analysis identifies genes positively (red) and negatively (blue) associated with single-cell fitness.

(C) Meta-analysis of fitness-associated genes across all KP tumors.

(D) Gene expression UMAP annotated by individual cells' single-cell FitnessSignature scores (normalized to a 0–1 scale).

(E) Average FitnessSignature scores of each Leiden cluster (normalized to 0–1). Colors reflect the Leiden clusters in (A).

(F) Kaplan-Meier survival analysis of TCGA lung adenocarcinoma patients (n=495) stratified into high (red) and low (blue) groups based on gene expression of the derived transcriptional FitnessSignature. (Log-rank test, p = 5e−4).

(G) Gene expression UMAP annotated with transcriptional scores of the three fitness gene modules. (H) Heatmap of Z-normalized Pearson's correlations between marker gene expression and fitness module scores for selected differentially expressed genes with manual annotations. Genes are colored by assigned fitness gene module; genes in black indicate helpful markers that did not appear in a fitness module.

significantly similar to the relationships inferred from our Cas9 lineage-tracing trees (Figures S2G–S2I; Permutation Test; see STAR Methods). Furthermore, expanding subclones were significantly enriched for CNVs (Mann-Whitney U test p < 0.0001, Figures 2C, 2D, and S2J), and independent subclonal expansions from the same tumor could harbor distinct CNV patterns (Figure S2K). Third, cancer cells in expansions had significantly higher expression of cell-cycle genes (Mann-Whitney U test; Figures 2E and S2F; STAR Methods). Together with our tumor spatial-lineage analysis (see below), these orthogonal data strongly support the fidelity of our tumor phylogeny and expansion calling and indicate the aggressive nature of subclonal expansions.

In population genetics, the relative "fitness" of a sample can be defined as the growth advantage of an individual compared with the rest of the population (Williams et al., 2018). The fine-scale structure of our lineages offers us the opportunity to predict fitness at single-cell resolution (Figure 2F; STAR Methods, Neher et al., 2014). This analysis revealed a spectrum of intratumoral fitness distributions across tumors (Figure 2G) with expanding cells consistently having higher single-cell fitness scores (Mann-Whitney U test p < 0.0001, Figures 2F and 2H). Overall, these results argue that we can quantitatively infer the relative fitness of individual cells within a tumor and that cell fitness is consistent with the subclonal dynamics revealed by the tumor phylogeny.

Integration of phylodynamics and transcriptome uncovers fitness-associated gene programs for KP tumors

With quantitative measurements of single-cell fitness in each tumor, we next sought to identify the molecular features consistently associated with subclonal expansions. Consistent with KP tumor progression being driven largely by epigenetic rather than genetic changes (LaFave et al., 2020; Arnal-Estapé et al., 2020; Marjanovic et al., 2020), we observed that CNV profiles within expansions were largely inconsistent across tumors (Figure S2L). We therefore examined the transcriptomic differences underpinning expansion. By integrating the scRNA-seq data across tumors, we detected 15 distinct subpopulations characterized by marker genes consistent with previous work in the KP model: spanning from an early-stage alveolar type 2 (AT2)-like population, characterized by expression of *Lyz2* and *Sftpc*, to late-stage Epithelial-Mesenchymal transition (EMT)-related clusters characterized by expressions of *Vim, Twist1*, and *Zeb2* ((Marjanovic et al., 2020; LaFave et al., 2020); Figures 3A and S3A; Table S2). Notably, although normal AT2 cells appeared similar to the tumor AT2-like state, the transcriptome of cancer cells could be clearly distinguished from normal AT2 cells (Figure S3B; STAR Methods). Together, the agreement of transcriptomic states observed here and in previous studies implies that the continuous lineage-tracing system did not strongly perturb tumor progression.

Combining the aforementioned single-cell fitness scores with single-cell transcriptomes for each tumor, we next identified genes associated with changes in fitness for each tumor (Figure 3B; STAR Methods). We then utilized a majority vote meta-analysis of differentially expressed genes across tumors to find genes consistently associated with fitness differences (Figure 3C; STAR Methods; Table S3). The resulting consensus genes associated with elevated fitness revealed broad transcriptomic changes and were enriched for gene sets associated with ribosome biogenesis, stem cell differentiation, and wound healing (Table S3).

The genes detected in our majority vote meta-analysis represented a transcriptional program (hereafter referred to as the "FitnessSignature") consistently associated with tumor expansions that could be used to describe state trajectories underlying tumor evolution. Indeed, the AT2-like cluster had the lowest FitnessSignature score, whereas the Mesenchymal clusters scored highest (Figures 3D and 3E; STAR Methods). Interestingly, the ranking of Leiden clusters in between these extremes suggested that an increase in FitnessSignature was concomitant with transitions from the AT2-like state through various Gastric, Endoderm-like, or Lung Mixed states to an eventual Mesenchymal state (Figures 3D and 3E). Importantly, the FitnessSignature scores were significantly associated with poor prognosis in patients with lung adenocarcinoma from The Cancer Genome Atlas (TCGA; The Cancer Genome Atlas Research Network, 2014; Figure 3F; STAR Methods).

Consistent with previous studies showing increased transcriptional heterogeneity during KP tumor evolution (Marjanovic et al., 2020), we observed that tumors occupied qualitatively different transcriptional states (Figure S3E). This progression could be categorized into three nonoverlapping gene modules decomposed from the FitnessSignature (Figures S3F and S3G; STAR Methods): Module 1 contained genes enriched for gastric and endoderm signatures (*Tff1*, *Hnf4a*, and *Gkn2*), Module 2 contained a subset of EMT marker genes and some neuronal genes (*Hmga2*, *Inhba*, and *Gap43*), and Module 3 contained classical mesenchymal and prometastasis genes (*Vim*, *Twist1*, *Cdh2*, *Cd109*, and *Runx2*) (Figures 3G and 3H; Table S3). Additionally, tumor subclonal expansions could preferentially employ a particular module, although some expansions exhibited coexpression of multiple modules (Figures 3I, S3I, and S3J; STAR Methods). Importantly, the expression of each of these modules was predictive of worse patient survival in the TCGA lung adenocarcinoma cohort (Figure S3H; STAR Methods). Collectively, these results argue that increased cell fitness in lung adenocarcinoma can be achieved via at least three distinct transcriptional modules.

Intratumoral transcriptional heterogeneity is driven by transient increases in plasticity of cell states

We next investigated the dynamics of intratumoral transcriptional diversity, as such behavior can be a driver of tumor

---

(I) Personality plots of three representative tumors displaying the fold change in fitness module scores of individual expansions compared with the nonexpanding regions. Vertices indicate individual fitness modules. Axes are normalized to 0.4-fold to 2.2-fold change observed across tumors. Inner circle represents a fold change of 1 (no change), and values greater than 1 indicate the cells in expansions exhibiting enriched usage of the particular fitness gene module. Colors (see (H)) reflect the module a tumor expansion is characterized by.

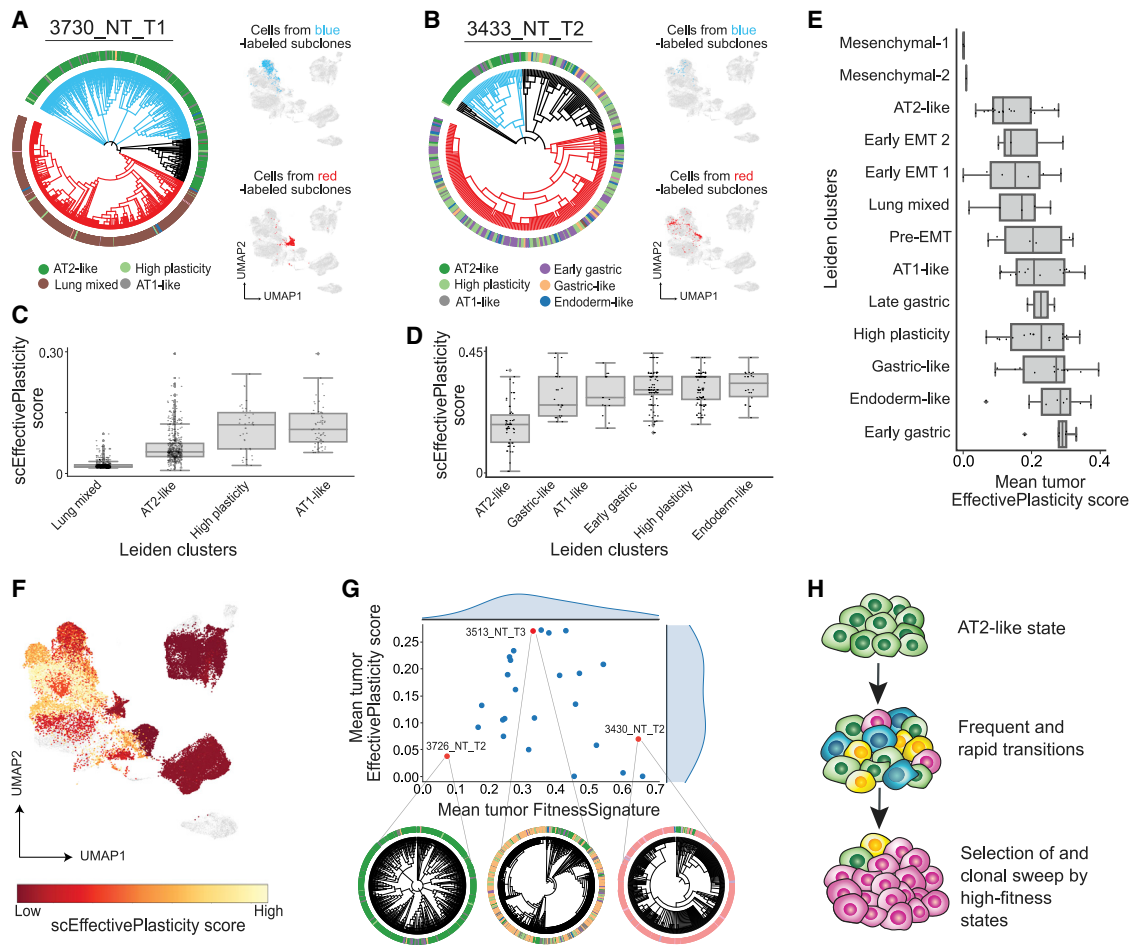See also Figure S3 and Tables S2 and S3.

Figure 4. Intratumoral transcriptional heterogeneity is driven by transient increases in plasticity of cell states

(A and B) Representative tumors with (A) low EffectivePlasticity and (B) high EffectivePlasticity. Outer bar indicates the Leiden cluster of single cells (as in 3A). Selected clades are highlighted on the gene expression UMAP to the right of phylogenies.

(C and D) Quantification of scEffectivePlasticity for each transcriptional state (Leiden cluster) for tumors in (A) and (B).

Each dot represents a single cell's EffectivePlasticity.

(E) Distribution of mean EffectivePlasticity scores for each Leiden cluster across KP tumors. Each dot represents a Leiden cluster's mean EffectivePlasticity within a tumor. Leiden clusters are ranked by the mean of the distribution across tumors.

(F) scEffectivePlasticity score overlaid onto the gene expression UMAP. Cells marked in gray are from metastases and not included.

(G) Relationship between tumor average FitnessSignature and EffectivePlasticity. Three representative phylogenies are displayed with Leiden cluster annotations (outer circle).

(H) A model describing changes of transcriptome heterogeneity and EffectivePlasticity following tumor progression.

See also Figure S4.

aggressiveness and therapeutic resistance (Patel et al., 2014; Rathert et al., 2015; Shaffer et al., 2017; Kim et al., 2018; Marjanovic et al., 2020; Maynard et al., 2020). In our model, tumors varied widely in the transcriptional states they occupied, rarely being dominated by a single state. Although tumors with low FitnessSignature scores were enriched for the AT2-like state, increases in the fitness score were associated with Gastric-like, Lung Mixed, and Mesenchymal states (Figure S4A). Moreover, tumors had generally similar levels of transcriptional state heterogeneity, as measured by the Shannon's Entropy Index ((Marjanovic et al., 2020; LaFave et al., 2020); Figure S4B).

How is this intratumoral diversity established and maintained? In principle, this diversity reflected by the entropy index can be achieved either by rare transitions and stable commitment to distinct states or by frequent transitions between these states. Lineage tracing is uniquely positioned to distinguish these two models as it directly reports how intermixed transcriptomic states are in subclonal lineages, thus providing a measure of effective plasticity. Interestingly, tumor subclones exhibited varying amounts of plasticity: some tumor subclones were dominated by a single-transcriptomic state, suggesting strong stability (Figure 4A), whereas others were characterized by strong mixing between transcriptomic states (Figure 4B). Using tumor phylogenies, we estimated the frequency of cellular state changes for each tumor to create an empirical measurement of the tree plasticity (hereafter referred to as the "EffectivePlasticity" score) and

extended this measure to a single-cell statistic ("scEffectivePlasticity") by averaging together the EffectivePlasticity scores for all the subclades that contained a particular cell (Quinn et al., 2021; STAR Methods). Importantly, this scEffectivePlasticity statistic was consistent with alternative approaches that quantified the effective plasticity by comparing transcriptional states between cells with similar indel states (without relying on trees; Figures S4C–S4E) or by computing dissimilarity in gene expression profiles between nearest neighbors on the phylogeny (Figures S4F–S4H; STAR Methods).

In two representative tumors, we observed that cells from the AT2-like state exhibited consistently low scEffectivePlasticity, whereas other states like the Gastric- and AT1-like state had elevated scEffectivePlasticity scores (Figures 4C and 4D). To systematically quantify the relative effective plasticity of different cell states, we averaged scEffectivePlasticity scores for each Leiden cluster on a tumor-by-tumor basis (Figure 4E). Mesenchymal (Leiden clusters 1 & 2) and AT2-like clusters (Leiden cluster 4) represented the most stable states, whereas the previously reported "High-Plasticity Cell State" (Marjanovic et al., 2020; Leiden cluster 5), Gastric-like (Leiden clusters 3, 8, 12), and Endoderm-like states (Leiden cluster 0) exhibited high EffectivePlasticity (Figure 4F).

We next investigated the relationship of tumor plasticity, as measured by EffectivePlasticity, and aggressiveness, as measured by the FitnessSignature. Although previous studies have indicated that transcriptional heterogeneity is a hallmark of tumor progression (Marjanovic et al., 2020), we found that the average EffectivePlasticity score was maximized when the FitnessSignature score was in the intermediate regime and minimized when the FitnessSignature was on the low or high extremes (Figures 4G, S4I, and S4J). Taken together, these findings support a model of tumor progression, whereby the loss of AT2-like state was accompanied by rapid, parallel transitions to generate high transcriptomic heterogeneity, which permitted selection of increasingly stable states with higher-fitness and ultimately resulted in subclonal expansion and tumor progression (Figure 4H).

Mapping the phylogenetic relationships between cell states reveals common paths of tumor evolution

In principle, the observed cellular plasticity and subsequent transcriptional heterogeneity in the KP model could arise from either random or structured evolutionary paths through transcriptional states. To investigate the consistency of evolutionary paths across tumors, we developed a statistic termed "Evolutionary Coupling," which extends a clonal coupling statistic (Weinreb et al., 2020; Wagner et al., 2018) to quantify the phylogenetic distance between pairs of cell states (STAR Methods).

Applying this approach to individual tumors uncovered distinct coupling patterns between transcriptomic states. In one example tumor, the Lung Mixed state was more closely related to the High-Plasticity state than to the AT2-like state (Figures 5A and 5B). In another tumor, the Gastric-like and High-Plasticity states clustered together, whereas the AT1-like and Early Gastric states clustered together (Figures 5C and 5D). Relationships for these two tumors were consistent with alternative definitions for interstate coupling, inferred directly from the indel information (without

relying on trees; Figures S5A and S5B; STAR Methods) or based on local neighborhoods on the tree (Figure S5C and S5D; STAR Methods); these statistics were generally consistent across trees (Figure S5E).

A data-driven hierarchical clustering of the full set of tumors based on their transcriptional state occupancy and Evolutionary Couplings revealed that tumors could be classified into three distinct groups ("Fate Clusters"; Figures 5E and S5F; STAR Methods; Table S4). Although some transcriptional states were shared between Fate Clusters 1 and 2 (including the AT2-like, AT1-like, and High-Plasticity states), Fate Cluster 1 was predominantly distinguished by couplings that include the Gastric-like (Leiden clusters 3, 8, and 12) and Endoderm-like states (Leiden cluster 0; Figure 5F, left, Figure S5G) and Fate Cluster 2 by evolution toward the Lung Mixed state (Leiden cluster 10; Figure 5F, middle, Figure S5G). Fate Cluster 3 was more difficult to interpret as it lacked couplings with the AT2-like state and instead was dominated by high-fitness states, such as early EMT (Leiden clusters 7 and 13) and Mesenchymal states (Leiden clusters 1 and 2; Figure 5F, right, Figure S5G).

We thus hypothesized that the majority of differences between tumors was driven by tendencies toward Fate Clusters 1 or 2. Indeed, Principal Component Analysis (PCA) on Evolutionary Couplings and state composition revealed that the first two principal components explained a substantial amount of the observed variance (~32%; Figure S5H), and couplings involving the Gastric & Endoderm states (Fate Cluster 1; Leiden clusters 3, 8, 0) or the Lung Mixed state (Fate Cluster 2; Leiden cluster 10) were among the strongest features distinguishing tumors (Figure S5I). Taken together, these distinct coupling patterns argue that tumor progression from the initial AT2 state preferentially follows one of two nonoverlapping evolutionary paths, characterized by Fate Clusters 1 and 2, to aggressive states like those found in Fate Cluster 3.

To characterize the transcriptional changes that underlie these two alternative fates (Fate Clusters 1 & 2), we developed "Phylotime": a single-cell statistic that quantifies the evolutionary distance between an individual cell and cells in the progenitor, AT2-like state (STAR Methods). Importantly, estimates of Phylotime were consistent with different metrics for approximating distances on the tree: either by the absolute number of mutations or the number of mutation-bearing edges (Figures S5J and S5K). Integrating Phylotimes from tumors within Fate Clusters 1 and 2 confirmed two separate evolutionary routes (Figure 5G) and highlighted distinct transcriptional changes associated with Phylotime along each route (Figure 5H; STAR Methods; Table S5). Specifically, although expressions of early markers like *Lyz2* and *Sftpc* were shared in early Phylotime of both Fate Clusters, late Phylotime in Fate Cluster 1 was enriched for gastric and endoderm markers like *Gkn2*, whereas late Phylotime in Fate Cluster 2 was characterized by markers of airway progenitors, such as *Sox2* and *Scgb1a1* (Leeman et al. 2014), and markers of tumor propagating cells, like *Cd24a* and *Itgb4* (Zheng et al. 2013; Bierie et al. 2017). Although Fate Cluster 3 tumors generally had poor couplings with earlier states, our data suggest that tumors can evolve from either the Fate Cluster 1 or Fate Cluster 2 into an EMT state and progress to late-stage Mesenchymal states (Figure S5L). Overall, our analysis provides
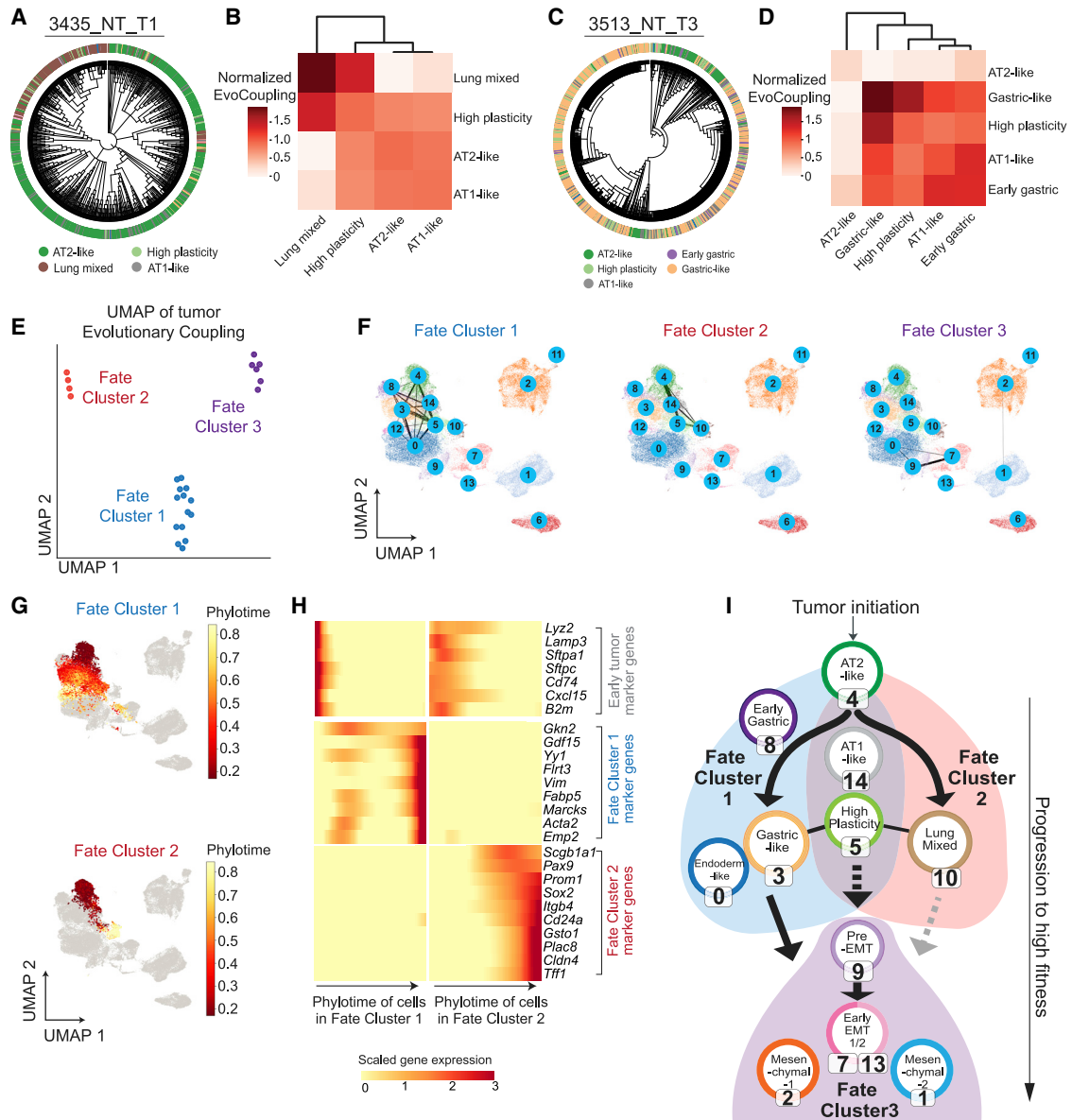
Figure 5. Mapping the phylogenetic relationships between cell states reveals common paths of tumor evolution

(A–D) Transcriptional state relationships of representative tumors are quantified with Evolutionary Couplings.

(A and C) phylogenies of tumors 3435_NT_T1 and 3513_NT_T3 with overlaid Leiden cluster annotations (colors from Figure 3A).

(B and D) Corresponding normalized Evolutionary Couplings between Leiden clusters in each tumor.

(E) UMAP projection of KP tumor Evolutionary Couplings annotated by identified "Fate Clusters" (see Figure S5F). Dots correspond to tumors.

(F) Aggregated Evolutionary Couplings between transcriptional states of tumors from each Fate Cluster visualized on the gene expression UMAP. Thickness of bars reflect the average magnitude of couplings across tumors in a Fate Cluster.

(G) Gene expression UMAP annotated by Phylotime of single cells from tumors in Fate Cluster 1 (top) and 2 (bottom) (normalized to 0–1). Cells from tumors that do not appear in the Fate Cluster of interest are shown in gray.

(H) Significant gene expression changes along Phylotime for Fate Clusters 1 and 2 across Phylotime quantiles. Genes are annotated by their assigned Fate Cluster. Colors in heatmap are library-normalized gene expression, Z-normalized across quantiles of both Fate Clusters.

(I) Summary of major paths of KP tumor progression. Solid lines indicate direct evidence of Evolution Couplings; dotted lines indicate couplings likely involving unobserved intermediate states; and gray lines indicate couplings that are supported by rare examples.

See also Figure S5 and Tables S4 and S5.

evidence that KP tumors could evolve predominantly through one of two major paths with one toward Gastric-like and Endo-derm-like state and the other through the Lung Mixed state, with distinct transcriptional changes associated with each evolutionary trajectory (summarized in Figure 5I).

Loss of tumor suppressors alters tumor transcriptome, plasticity, and evolutionary trajectory

Tumor suppressor genes regulate diverse cellular activities, and their loss is associated with increased tumor aggressiveness (Weinberg, 1991; Sherr, 2004); however, it remains unclear how these genes affect tumor evolutionary dynamics *in vivo*. Here, we combined genetic perturbations with our quantitative phylodynamic approaches to interrogate how additional onco-genic mutations altered KP tumor evolutionary trajectories.

We focused on two frequently mutated tumor suppressors in human lung adenocarcinoma, *LKB1* and *APC* (Ding et al., 2008; The Cancer Genome Atlas Research Network, 2014; Skoulidis et al., 2015). Both genes have been studied extensively in both human and mouse models and appear to regulate progression through distinct mechanisms (Ji et al., 2007; Carretero et al., 2010; Nguyen et al., 2009; Hollstein et al., 2019; Tammela et al., 2017; Murray et al., 2019; Kerk et al., 2021; Parsons et al., 2021). We engineered our lenti-Cre-BC vector to carry an additional sgRNA targeting *Lkb1* or *Apc*, such that delivery of this vector simultaneously initiated tumor induction, lineage tracing, and disruption of the targeted tumor suppressor gene. With this system, we collected data from 18,321 cells across 57 KP tumors with *Lkb1* knockout (24 primary and 33 metastatic tumors; referred to as KPL tumors) and 13,825 cells across 35 KP tumors with *Apc* knockout (23 primary and 12 metastatic tumors; referred to as KPA tumors). Targeting of either *Lkb1* or *Apc* increased tumor burden (Rogers et al., 2018), but did not appear to alter the number and relative size of subclonal expansions (Figures S6A and S6B). However, genes associated with tumor fitness were largely distinct across genetic backgrounds (Figure S6C; Table S3).

To examine whether perturbations alter the transcriptional landscape of KP tumors, we integrated transcriptional states of KPL and KPA tumors with the prior KP dataset. Although many cells could be classified into existing Leiden clusters identified in the KP analysis, the additional perturbations also created four new transcriptional states (Figure 6A; STAR Methods). As expected from *Apc*'s role as a negative regulator of *Wnt* signaling (Barker et al., 2009), *Axin2* expression was high in the three KPA-specific clusters, indicative of elevated *Wnt* signaling (Figure S6D), as was the expression of *Wnt* antagonists such as *Notum* and *Nkd1* that were recently reported to increase the ability of cancer cells to compete with the neighboring niche in human *APC* mutant colon tumors ((Flanagan et al., 2021; Neerven et al., 2021); Figure S6D; Table S3). Moreover, targeting of *Lkb1* or *Apc* resulted in changes to the relative occupancies of transcriptomic states: KPL tumors were primarily enriched in the Pre-EMT state (Leiden cluster 9), whereas KPA tumors were enriched in Apc-specific early, mesenchymal, and metastatic states (Leiden clusters 15, 16, and 17; Figures 6B, 6C, and S6E).

Interestingly, although most cell states had comparable EffectivePlasticity across tumor genotypes (Figure S6F), the

Pre-EMT state (Leiden cluster 9) in KPL tumors had significantly less EffectivePlasticity, indicating stabilization of this cell state (p < 0.05, Mann-Whitney U test; Figure 6D). We next identified genes differentially expressed in cells from KPL tumors in the Pre-EMT cluster (Figure 6E; Table S2; STAR Methods), which included gene programs that can promote prometastatic chromatin remodeling (*Sox17*; Pierce et al., 2021), tumor progression (*Ifitm1* and loss of *Gata6*; Yan et al., 2019; Cheung et al., 2013), metastatic ability (*Mmp7*; He et al., 2018), and tumor fitness by modulating cancer-immune cell interaction (*Cd24a*, *Il33*, and loss of *Apoe*; Sinjab et al., 2021; Li et al., 2019; Tavazoie et al., 2018). These together potentially explain why the Pre-EMT state was uniquely stabilized in KPL tumors.

To examine how loss of tumor suppressors altered evolutionary trajectories, we performed PCA on the transcriptional state occupancy and Evolutionary Couplings of individual tumors and found that tumors broadly segregated according to their genotypes (Figure 6F; STAR Methods; Table S4). Specifically, KPA tumors created a unique trajectory including a coupling between the AT2-like and the Apc-early states (Leiden clusters 4 and 16), whereas KPL tumors were characterized by couplings between the Pre-EMT state and nearby states (Figure 6G).

In summary, although the targeting of the tumor suppressors *Lkb1* or *Apc* both increased tumor growth, their effects on cell states, plasticity, and paths of evolution varied substantially. Specifically, KPL tumors quickly progressed to and became stabilized in the Pre-EMT state, whereas KPA tumors largely exploited a distinct path through new *Apc*-specific states (Figure S6G and summarized in Figure 6H; Table S4). Together, our analyses highlight how lineage tracing offers rich information for dissecting the multifaceted role of tumor suppressors in tumor evolution.

Metastases originate from spatially localized, expanding subclones of primary tumors

Metastases account for 90% of cancer mortality, yet remain difficult to study because of their spatially and temporally sporadic nature (Ganesh and Massagué, 2021). An outstanding question is how metastases originate from the primary tumor. Here, we integrated lineage tracing with spatial and transcriptomic information to investigate the subclonal origins and evolution of metastases.

We first focused on a single-primary tumor, which consisted of two independent subclonal expansions (3724_NT_T1; Figure 2B), and its four related metastases (three in liver and one in soft tissue; Figures 7A and S7A). We performed multiregional analysis of the primary tumor (Figure 7A, inset) and inferred a combined phylogeny relating all cells in the primary tumor and metastases. Integrating lineage-spatial information revealed that individual metastases originated from distinct spatial locations (Figures 7A–7C; STAR Methods) and phylogenetically originated from specific subclonal expansions in the primary tumor (Figures 7C and 7D).

To investigate the consistency of these results, we extended this phylogenetic analysis to five other tumor-metastasis families, across KP, KPL, and KPA backgrounds. Importantly, metastases were consistently more closely related phylogenetically
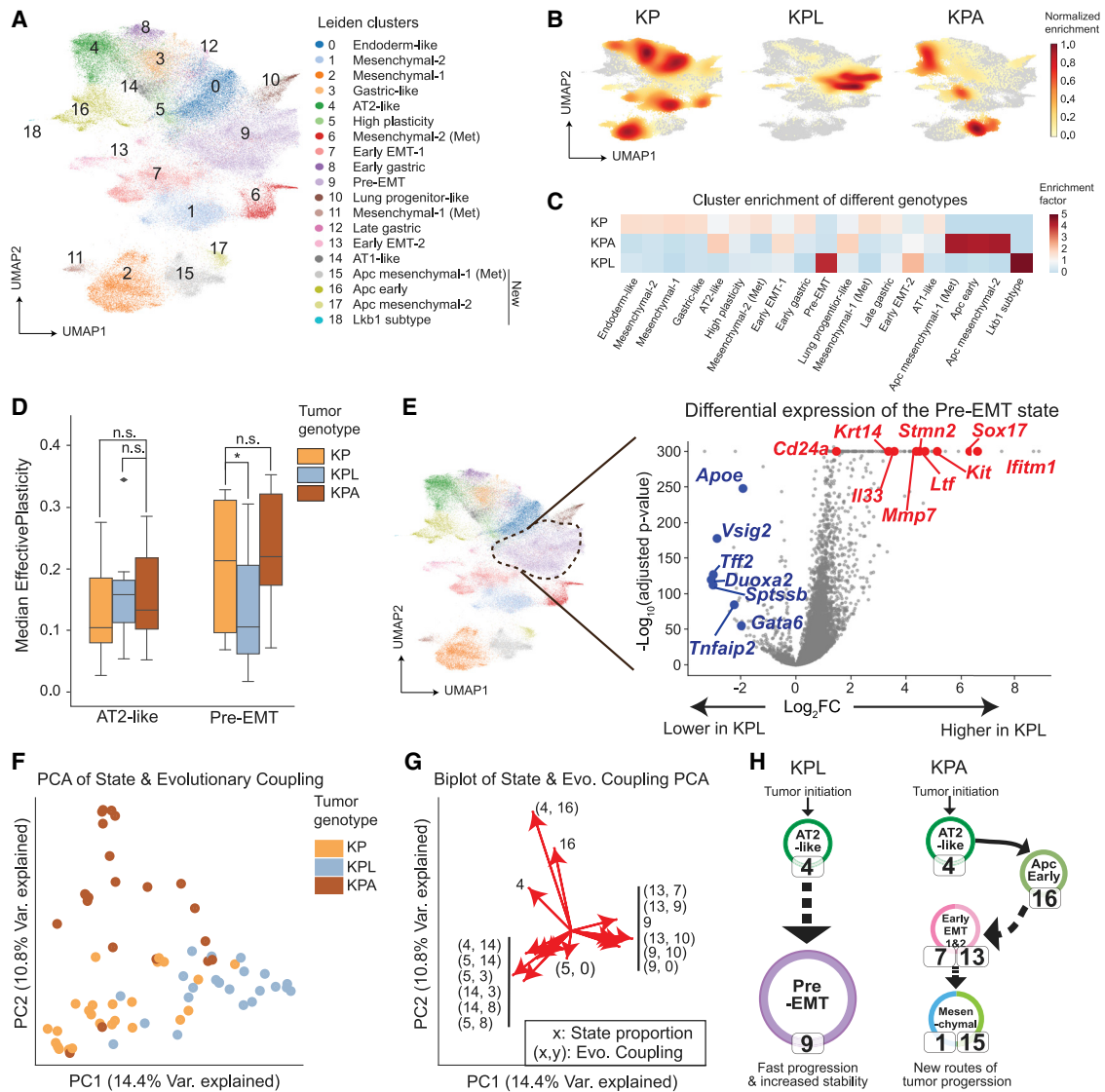
Figure 6. Loss of tumor suppressors alters tumor transcriptome, plasticity, and evolutionary trajectory

(A) Batch corrected and integrated gene expression UMAP of all cancer cells from KP, KPL, and KPA tumors annotated by 19 Leiden clusters (STAR Methods).

(B) Density plots of cancer cells from KP, KPL, and KPA tumors on the UMAP.

(C) Enrichment of genotypes in each Leiden cluster. Enrichments below 1 are colored blue; enrichments above 1 are colored red.

(D) Median EffectivePlasticity scores in selected Leiden clusters across genotypes (one-sided Mann-Whitney U test, *$p \leq 0.05$, n.s. = not significant).

(E) Genes up-regulated (red) and down-regulated (blue) in the Pre-EMT state of KPL tumors compared with KP and KPA tumors combined.

(F) PCA of Evolutionary Coupling and transcriptional state proportion vectors for all tumors analyzed across genotypes. Each dot represents a tumor.

(G) Biplot of top 10 features per principal component from PCA analysis shown in (F).

Evolutionary Couplings are shown as tuples (x, y); transcriptional state proportions are shown as a single number *x* indicating Leiden cluster ID.

(H) Summary of major evolutionary paths in KPL and KPA tumors. Solid lines indicate direct evidence of Evolution Couplings between transcriptome states and dotted lines indicate couplings that likely involve unobserved intermediate cell states.

See also Figure S6 and Tables S2, S3, and S4.

to specific subclonal expansions, regardless of the tumor genotype (Figures 7D and S7D). Collectively, our results argue that metastases generally originated from subclonal expansions within primary tumors. Independent metastases from the same primary tumor could arise from spatially and phylogenetically distinct subclones.

We next evaluated to what degree metastases preserved the transcriptional state of their origins in the primary tumor. Analysis of metastases arising from an example primary tumor (3724_NT_T1) revealed that liver metastases were more similar to the subclone from which they originated, whereas the soft tissue metastasis evolved to a new transcriptional state (Figures 7E
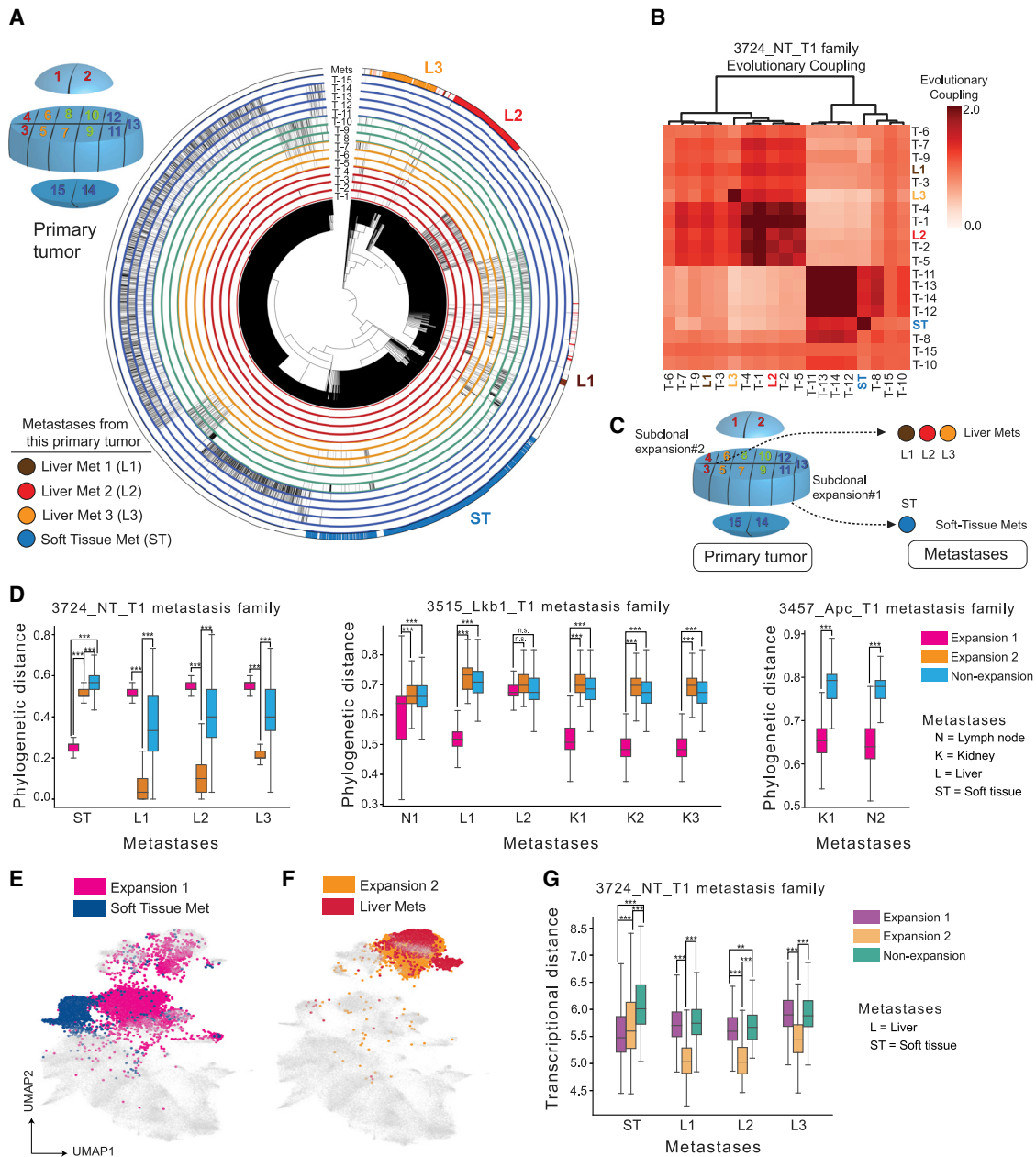
Figure 7. Metastases originate from spatially localized, expanding subclones of primary tumors

(A) Multiregion analysis of tumor-metastasis family 3724_NT_T1. Top left inset showed the relative spatial location of tumor pieces. The phylogeny of the primary tumor and metastases is annotated via peripheral radial tracks for each color-coded region of the tumor (matching the inset) and four metastases.

(B) Heatmap of Evolutionary Couplings of primary tumor pieces (black) and 4 related metastases (matching colors in (A)) from the 3724_NT_T1 tumor-metastasis family.

(C) Summary of the spatial-phylogenetic relationship of the tumor-metastasis family 3724_NT_T1. (D) Single-cell phylogenetic distance of each metastasis to the nonexpanding and expanding subclones in its related primary tumor. Each box represents the distribution of phylogenetic distances from a metastasis to a defined region of its related primary tumor (one-sided Mann-Whitney U test are indicated: ***p < 0.0001, n.s. = not significant).

(E and F) Gene expression UMAP annotated by metastases and their original subclones in 3724_NT_T1. Cells that are not relevant to the comparison in each panel are shown in gray.

(G) Transcriptional distances between expanding regions of 3724_NT_T1 and its four metastases (one-sided Mann-Whitney U test are indicated: **p < 0.001, ***p < 0.0001).

See also Figure S7.

and 7F). This was further quantified by measurements of total transcriptional distance between each metastasis and the subclonal expansions in the metastatic primary tumor (Figure 7G). Liver metastases were significantly more similar to its originating subclonal expansion (p < 0.0001, one-sided Mann-Whitney U test), whereas the soft tissue metastasis did not clearly resemble its subclonal origin (Figure 7G; STAR Methods). Consistently, metastases from KP, KPL, and KPA mice were significantly more similar, as measured by transcriptional state, to their respective expanding subclades in the primary tumor as compared with nonexpanding regions, further suggesting that progression at the primary site is a prerequisite for metastasis (LaFave et al., 2020; Figure S7E).

In addition, our high-resolution lineage tracing offered evidence of complex metastatic behaviors, including multisubclonal seeding from a primary tumor to the lymph node, and cross-seeding from one metastatic primary tumor to another primary tumor, or from one metastasis to another (Figures S7A–S7C). Collectively, these results highlight the ability of phylogenetic analysis to trace the origins and evolution of metastases.

DISCUSSION

In this study, we developed a genetically engineered mouse model of lung adenocarcinoma that allows Cre-inducible initiation of oncogenic mutations and simultaneous continuous *in vivo* lineage tracing of tumor development over many months, paired with a single-cell transcriptomic readout. This model system enabled us to track at an unprecedented resolution the recurring patterns of tumor evolution from activation of oncogenic mutations in single cells as they grow into large, aggressive, and ultimately metastatic tumors. Three principles emerged from our study, linking together tumor phylodynamics, fitness, plasticity, parallel evolutionary trajectories, origins of metastasis, and genetic determinants of tumor evolution.

First, tumors were driven by rare subclonal expansions that utilized distinct fitness-associated transcriptional programs and enabled both tumor progression at the primary site and metastasis to distant tissues. The expansions identified by tree topology argue for subclonal selection, distinct from evolutionary models lacking selective sweeps observed in other cancer types (Sottoriva et al., 2015). The identification of gene expression states associated with tumor fitness revealed a set of transcriptional fitness modules underlying KP-Tracer tumor development. Importantly, these signatures of aggressive tumors found in our mouse model were predictive of the outcome of human disease. Despite the higher somatic mutation burden and longer developing timescales of human tumors (Campbell et al., 2017; Jamal-Hanjani et al., 2017; Gerstung et al., 2020; Hill et al., 2021), our data uncovered critical fitness gene programs that are conserved in both mouse and human lung adenocarcinomas. Notably, we found that metastases consistently originated from expanding subclones, regardless of additional loss of *Lkb1* or *Apc*. They often retained the same transcriptional state as their original subclones but could further adopt distinct transcriptional states. This underscored the importance of tumor progression at the primary site in enabling metastasis (Caswell et al., 2014; Turajlic and Swanton, 2016; Hu et al., 2020; LaFave

et al., 2020) and argues against alternative models in which metastases arise early during tumor evolution (Hüsemann et al., 2008; Podsypanina et al., 2008; Klein, 2009; Rhim et al., 2012; Sottoriva et al., 2015).

Second, our analysis revealed that tumor progression is accompanied by transient increases in lineage plasticity. This period of high plasticity is followed by clonal sweeps of subclones with aggressive cell states that can remain stable even following metastasis to new environments. Our ability to monitor how often cells are transitioning between transcriptomic states also allowed us to untangle the relationship between intratumoral heterogeneity and lineage plasticity and shed light on the dynamics of the transcriptomic heterogeneity observed in the KP mouse model and human NSCLC (Marjanovic et al., 2020; Laughney et al., 2020). The finding that KP tumors progress via parallel, rapid transitions between cell states is consistent with previous work suggesting that epigenetic instability is a major driver of tumor progression in this model (LaFave et al., 2020; Marjanovic et al., 2020). Given the essential role of cellular plasticity in tumor progression and therapeutic resistance (Chaffer et al., 2013; Easwaran et al., 2014; Ge et al., 2017; Flavahan et al., 2017; Yuan et al., 2019; Quintanal-Villalonga et al., 2020), the ability of our lineage-tracing system to quantitatively explore plasticity provides a critical tool for understanding the role that cell state plasticity plays in various aspects of tumor evolution.

Third, tumors evolved through stereotypical trajectories and introduction of additional oncogenic mutations increased the speed of tumor evolution by creating new evolutionary trajectories. Traditionally, although cellular trajectories inferred by pseudotemporal approaches have proved to be a versatile tool for scRNA-seq datasets (Trapnell et al., 2014; La Manno et al., 2018), they make the inviolable assumption that transcriptional similarity indicates developmental relationship (Tritschler et al., 2019). Overcoming this, our measurement of cell state coupling directly from phylogenies enabled the discovery of two distinct evolutionary paths that are substantiated by transcriptional differences. Moreover, CRISPR targeting of tumor suppressors *Lkb1* and *Apc* altered the cellular plasticity and observed evolutionary paths in a genotype-specific way, which can be explained by alterations in transcriptional landscape. Collectively, our approach offers an orthogonal and more quantitative evaluation of the multifaceted role genes play in tumor evolution as compared with traditional growth-based fitness analysis. Future studies combining the KP-Tracer model and high-throughput *in vivo* functional genomics will be foundational in assessing the evolutionary consequences of any genes of interest in lung adenocarcinoma progression (Winters et al., 2018).

In summary, our results represent the first report of tracing the evolutionary history of a tumor from a single-transformed cell to an aggressive tumor using a CRISPR-based lineage tracer in an autochthonous mouse model. The continuous and high-resolution tumor lineage tracing in this setting offers a major advance in tumor evolution modeling by enabling quantitative inference of fitness landscapes, cellular plasticity, evolutionary paths, origins of metastases, and the role of tumor suppressors in altering all these facets of tumor development. With the expanding lineage-tracing toolkit and integration of other emerging data

modalities, we expect that the experimental and computational framework presented here will greatly improve future efforts at building high-dimensional, quantitative, and predictive models of tumor evolution, thus shedding light on new therapeutic strategies.

Limitations of the study

Our findings highlight several opportunities for future efforts. First, we were limited in our ability to describe the directionality of transitions or to rule out the possibility of unobserved intermediates. This issue could be resolved experimentally by harvesting samples from multiple time points of tumor development or expanding our lineage-tracing technology to develop multichannel molecular recorders for simultaneous recording of marker gene expression of intermediate states (Frieda et al., 2017; Tang and Liu, 2018). Alternatively, enhancing the interpretability of branch lengths by engineering a "molecular clock" or probabilistic models of Cas9 editing (Park et al., 2021) could aid in the reconstruction of unobserved intermediate states (Ouardini et al., 2021). Second, our fitness-inference approach assumes that evolution occurs via small effect size mutations, which may overlook the impact of mutations with large impact such as CNVs in other tumor models (Neher et al., 2014). Third, future integration of emerging data modalities with lineage tracing, such as combined genomic, multiomic, and spatial analyses (Mimitou et al., 2021; Ma et al., 2020; Lee et al., 2014; Stickels et al., 2021; Chow et al., 2021), will illuminate how genetic and epigenetic changes and the tumor microenvironment influence tumor evolution.

STAR★METHODS

Detailed methods are provided in the online version of this paper and include the following:

- KEY RESOURCES TABLE
- RESOURCE AVAILABILITY
  - Lead contact
  - Materials availability
  - Data and code availability
- EXPERIMENTAL MODEL AND SUBJECT DETAILS
  - Chimeric lineage tracing mouse model
- METHOD DETAILS
  - Lenti-sgRNA-Cre-Barcode vector
  - Lineage tracer vector (Target site & triple sgRNAs)
  - Lineage tracing embryonic stem cell engineering
  - Sample preparation and purification of cancer cells
  - Single-cell RNAseq library preparation
  - Target site library preparation
  - MULTI-seq library preparation
  - Lenti_Cre_BC library preparation
  - Sequencing
- QUANTIFICATION AND STATISTICAL ANALYSIS
  - Single-cell lineage tracing preprocessing pipeline and quality control filtering
  - Calling clonal populations and creating character matrices
  - Creating a consensus intBC set for mESC clones

- Tree Reconstruction with Cassiopeia
- Compatibility-based greedy heuristic for tree reconstruction
- Cell filtering with Lenti-Cre-BC

SUPPLEMENTAL INFORMATION

Supplemental information can be found online at https://doi.org/10.1016/j.cell.2022.04.015.

AUTHOR CONTRIBUTIONS

D.Y., M.G.J., T.J., N.Y., and J.S.W. conceived of, designed, and led the analysis of the KP-Tracer project. D.Y. constructed lineage-tracing targeting vectors and engineered the mouse ES cells with the help from J.L.P. and W.F-P. W.M.R. III generated the KP-Tracer chimeric mice, and S.N. transduced the mice. D.Y. and S.N. harvested tumors. D.Y. generated the single-cell RNA-seq data with help from C.S.M., D.M.P., Z.J.G., and E.D.C.; W.W. and T.G.B analyzed the TCGA data. M.G.J. and N.Y. conceived of computational approaches, and M.G.J. implemented these approaches. M.G.J., K.H.(J.)M., and D.Y. analyzed the data with help from F.H., X.Q., J.J.Q., R.H., M.Z.C., and M.M.C.; D.Y., M.G.J., N.Y., T.J., and J.S.W. interpreted results. D.Y., M.G.J., T.J., N.Y., and J.S.W. wrote the manuscript with input from all authors. J.S.W., T.J., and N.Y. supervised the project.

DECLARATION OF INTERESTS

J.S.W. declares outside interest in 5 AM Venture, Amgen, Chroma Medicine, KSQ Therapeutics, Maze Therapeutics, Tenaya Therapeutics, and Tessera Therapeutics. T.J. is a member of the Board of Directors of Amgen and Thermo Fisher Scientific, is a co-founder of Dragonfly Therapeutics and T2 Biosystems, and is the president of Break Through Cancer. T.J. serves on the Scientific Advisory Board of Dragonfly Therapeutics, SQZ Biotech, and Skyhawk

INCLUSION AND DIVERSITY

One or more of the authors of this paper self-identifies as an underrepresented ethnic minority in science. One or more of the authors of this paper self-identifies as a member of the LGBTQ+ community. One or more of the authors of this paper received support from a program designed to increase minority representation in science.

REFERENCES

Abbosh, C., Birkbak, N.J., Wilson, G.A., Jamal-Hanjani, M., Constantin, T., Salari, R., Le Quesne, J., Moore, D.A., Veeriah, S., Rosenthal, R., et al. (2017). Phylogenetic ctDNA analysis depicts early-stage lung cancer evolution. Nature 545, 446–451.

Adamson, B., Norman, T.M., Jost, M., Cho, M.Y., Nuñez, J.K., Chen, Y., Villalta, J.E., Gilbert, L.A., Horlbeck, M.A., Hein, M.Y., et al. (2016). A multiplexed single-cell CRISPR screening platform enables systematic dissection of the unfolded protein response. Cell 167, 1867–1882.e21.

Alemany, A., Florescu, M., Baron, C.S., Peterson-Maduro, J., and van Oudenaarden, A. (2018). Whole-organism clone tracing using single-cell sequencing. Nature 556, 108–112.

Amirouchene-Angelozzi, N., Swanton, C., and Bardelli, A. (2017). Tumor evolution as a therapeutic target. Cancer Discov. 7, 805–817.

Arnal-Estapé, A., Cai, W.L., Albert, A.E., Zhao, M., Stevens, L.E., López-Giráldez, F., Patel, K.D., Tyagi, S., Schmitt, E.M., Westbrook, T.F., et al. (2020). Tumor progression and chromatin landscape of lung cancer are regulated by the lineage factor GATA6. Oncogene 39, 3726–3737.

Barker, N., Ridgway, R.A., van Es, J.H., van de Wetering, M., Begthel, H., van den Born, M., Danenberg, E., Clarke, A.R., Sansom, O.J., and Clevers, H. (2009). Crypt stem cells as the cells-of-origin of intestinal cancer. Nature 457, 608–611.

Benjamini, Y., and Hochberg, Y. (1995). Controlling the false discovery rate: A practical and powerful approach to multiple testing. Journal of the Royal Statistical Society: Series B (Methodological) 57, 289–300.

Bhang, H.-E.C., Ruddy, D.A., Krishnamurthy Radhakrishna, V.K., Caushi, J.X., Zhao, R., Hims, M.M., Singh, A.P., Kao, I., Rakiec, D., Shaw, P., et al. (2015). Studying clonal dynamics in response to cancer therapy using high-complexity barcoding. Nat. Med. 21, 440–448.

Bierie, B., Sarah, E.P., Cornelia, K., Daniel, G.S., Diwakar, R.P., Prathapan, T., Joana, L.D., et al. (2017). "Integrin-β4 Identifies Cancer Stem Cell-Enriched Populations of Partially Mesenchymal Carcinoma Cells.". Proceedings of the National Academy of Sciences of the United States of America 114, E2337–E2346.

Black, J.R.M., and McGranahan, N. (2021). Genetic and non-genetic clonal diversity in cancer evolution. Nat. Rev. Cancer 21, 379–392.

Bowling, S., Sritharan, D., Osorio, F.G., Nguyen, M., Cheung, P., Rodriguez-Fraticelli, A., and Patel, S. (2020). An engineered CRISPR-Cas9 mouse line for simultaneous readout of lineage histories and gene expression profiles in single cells. Cell 181, 1410–1422.

Campbell, B.B., Light, N., Fabrizio, D., Zatzman, M., Fuligni, F., de Borja, R., Davidson, S., Edwards, M., Elvin, J.A., Hodel, K.P., et al. (2017). Comprehensive analysis of hypermutation in human cancer. Cell 171, 1042–1056.e10.

Cancer Genome Atlas Research Network (2014). Comprehensive molecular profiling of lung adenocarcinoma. Nature 511, 543–550.

Carretero, J., Shimamura, T., Rikova, K., Jackson, A.L., Wilkerson, M.D., Borgman, C.L., Buttarazzi, M.S., Sanofsky, B.A., McNamara, K.L., Brandstetter, K.A., et al. (2010). Integrative genomic and proteomic analyses identify targets for LKB1-deficient metastatic lung tumors. Cancer Cell 17, 547–559.

Caswell, D.R., Chuang, C.-H., Yang, D., Chiou, S.-H., Cheemalavagu, S., Kim-Kiselak, C., Connolly, A., and Winslow, M.M. (2014). Obligate progression precedes lung adenocarcinoma dissemination. Cancer Discov. 4, 781–789.

Chaffer, C.L., Marjanovic, N.D., Lee, T., Bell, G., Kleer, C.G., Reinhardt, F., D'Alessio, A.C., Young, R.A., and Weinberg, R.A. (2013). Poised chromatin at the ZEB1 promoter enables breast cancer cell plasticity and enhances tumorigenicity. Cell 154, 61–74.

Chan, M.M., Smith, Z.D., Grosswendt, S., Kretzmer, H., Norman, T.M., Adamson, B., Jost, M., Quinn, J.J., Yang, D., Jones, M.G., et al. (2019). Molecular recording of mammalian embryogenesis. Nature 570, 77–82.

Cheung, W.K.C., Zhao, M., Liu, Zongzhi, Stevens, L.E., Cao, P.D., Fang, J.E., Westbrook, T.F., and Nguyen, D.X. (2013). Control of alveolar differentiation by the lineage transcription factors GATA6 and HOPX inhibits lung adenocarcinoma metastasis. Cancer Cell 23, 725–738.

Chow, K.K., Budde, M.W., Granados, A.A., Cabrera, M., Yoon, Shinae, Cho, S., Huang, T.-H., et al. (2021). Imaging cell lineage with a synthetic digital recording system. Science 372, p.eabb3099.

Chuang, C.H., Greenside, P.G., Rogers, Z.N., Brady, J.J., Yang, D., Ma, R.K., Caswell, D.R., Chiou, S.H., Winters, A.F., and Grüner, B.M. (2017). Molecular definition of a metastatic lung cancer state reveals a targetable CD109–Janus kinase–Stat Axis. Nat. Medicine 23, 291–300.

Davis, A., Gao, Ruli, and Navin, N. (2017). Tumor evolution: linear, branching, neutral or punctuated? Biochim. Biophys. Acta Rev. Cancer 1867, 151–161.

Denny, S.K., Yang, D., Chuang, C.-H., Brady, J.J., Lim, J.S., Grüner, B.M., Chiou, S.-H., Schep, A.N., Baral, J., Hamard, C., et al. (2016). Nfib promotes metastasis through a widespread increase in chromatin accessibility. Cell 166, 328–342.

DeTomaso, D., Jones, M.G., Subramaniam, M., Ashuach, T., Ye, C.J., and Yosef, N. (2019). Functional interpretation of single cell similarity maps. Nat. Commun. 10, 4376.

DeTomaso, D., and Yosef, N. (2021). Hotspot identifies informative gene modules across modalities of single-cell genomics. Cell Syst. 12, 446–456.e9.

Ding, L., Getz, G., Wheeler, D.A., Mardis, E.R., McLellan, M.D., Cibulskis, K., Sougnez, C., Greulich, H., Muzny, D.M., Morgan, M.B., et al. (2008). Somatic mutations affect key pathways in lung adenocarcinoma. Nature 455, 1069–1075.

Driessens, G., Beck, B., Caauwe, A., Simons, B.D., and Blanpain, C. (2012). Defining the mode of tumour growth by clonal analysis. Nature 488, 527–530.

DuPage, M., Dooley, A.L., and Jacks, T. (2009). Conditional mouse lung cancer models using adenoviral or lentiviral delivery of Cre recombinase. Nat. Protoc. 4, 1064–1072.

Easwaran, H., Tsai, H.C., and Baylin, S.B. (2014). Cancer epigenetics: tumor heterogeneity, plasticity of stem-like states, and drug resistance. Mol. Cell 54, 716–727.

El-Kebir, M., Satas, G., Oesper, L., and Raphael, B.J. (2016). Inferring the mutational history of a tumor using multi-state perfect phylogeny mixtures. Cell Syst. 3, 43–53.

Fitch, W.M. (1971). Toward defining the course of evolution: minimum change for a specific tree topology. Syst. Biol. 20, 406–416.

Flanagan, D.J., Pentinmikko, N., Luopajärvi, K., Willis, N.J., Gilroy, K., Raven, A.P., Mcgarry, L., Englund, J.I., Webb, A.T., Scharaw, S., et al. (2021). NOTUM from Apc-mutant cells biases clonal competition to initiate cancer. Nature 594, 430–435.

Flavahan, W.A., Gaskell, E., and Bernstein, B.E. (2017). Epigenetic plasticity and the hallmarks of cancer. Science *357*, p.eaal2380.

Frese, K.K., and Tuveson, D.A. (2007). Maximizing mouse cancer models. Nat. Rev. Cancer *7*, 645–658.

Frieda, K.L., Linton, J.M., Hormoz, S., Choi, Joonhyuk, Chow, K.K., Singer, Z.S., Budde, M.W., Elowitz, M.B., and Cai, L. (2017). Synthetic recording and in situ readout of lineage information in single cells. Nature *541*, 107–111.

Ganesh, K., and Massagué, J. (2021). Targeting metastatic cancer. Nat. Med. *27*, 34–44.

Gao, R., Bai, S., Henderson, Y.C., Lin, Y., Schalck, A., Yan, Y., Kumar, T., Hu, M., Sei, E., Davis, A., et al. (2021). Delineating copy number and clonal substructure in human tumors from single-cell transcriptomes. Nat. Biotechnol. *39*, 599–608.

Gayoso, A., Lopez, R., Xing, G., Boyeau, P., Valiollah Pour Amiri, V., Hong, J., Wu, K., Jayasuriya, M., Mehlman, E., Langevin, M., et al. (2022). A Python library for probabilistic analysis of single-cell omics data. Nat. Biotechnol. *40*, 163–166.

Ge, Y., Gomez, N.C., Adam, R.C., Nikolova, M., Yang, H., Verma, A., Lu, C.P.-J., Polak, L., Yuan, S., Elemento, O., et al. (2017). Stem cell lineage infidelity drives wound repair and cancer. Cell *169*, 636–650.e14.

Gerlinger, M., McGranahan, N., Dewhurst, S.M., Burrell, R.A., Tomlinson, I., and Swanton, C. (2014). Cancer: evolution within a lifetime. Annu. Rev. Genet. *48*, 215–236.

Gerstung, M., Jolly, C., Leshchiner, I., Dentro, S.C., Gonzalez, S., Daniel Rosebrock, D., Mitchell, T.J., Rubanova, Y., and Anur, P. (2020). The evolutionary history of 2,658 cancers. Nature *578*, 122–128.

Griffiths, R.C., and Tavaré, S. (1998). The age of a mutation in a general coalescent tree. Commun. Stat. Stochast. Models *14*, 273–295.

Hanahan, D., and Weinberg, R.A. (2011). Hallmarks of cancer: the next generation. Cell *144*, 646–674.

Hann, B., and Balmain, A. (2001). Building 'validated' mouse models of human cancer. Curr. Opin. Cell Biol. *13*, 778–784.

Hartigan, J.A. (1973). Minimum mutation fits to a given tree. Biometrics *29*, 53–65.

He, W., Zhang, H., Wang, Y., Zhou, Y., Luo, Y., Cui, Y., Jiang, N., Jiang, W., Wang, H., Xu, D., et al. (2018). CTHRC1 induces non-small cell lung cancer (NSCLC) invasion through upregulating MMP-7/MMP-9. BMC Cancer *18*, 400.

Hill, W., Caswell, D.R., and Swanton, C. (2021). Capturing cancer evolution using genetically engineered mouse models (GEMMs). Trends Cell Biol *31*, 1007–1018.

Hollstein, P.E., Eichner, L.J., Brun, S.N., Kamireddy, A., Svensson, R.U., Vera, L.I., Ross, D.S., Rymoff, T.J., Hutchins, A., Galvez, H.M., et al. (2019). The AMPK-related kinases SIK1 and SIK3 mediate key tumor-suppressive effects of LKB1 in NSCLC. Cancer Discov. *9*, 1606–1627.

Hu, Z., and Curtis, C. (2020). Looking backward in time to define the chronology of metastasis. Nat. Commun. *11*, 3213.

Hu, Z., Li, Z., Ma, Z., and Curtis, C. (2020). Multi-cancer analysis of clonality and the timing of systemic spread in paired primary tumors and metastases. Nat. Genet. *52*, 701–708.

Hüsemann, Y., Geigl, J.B., Schubert, F., Musiani, P., Meyer, M., Burghart, E., Forni, G., Eils, R., Fehm, T., Riethmüller, G., et al. (2008). Systemic spread is an early step in breast cancer. Cancer Cell *13*, 58–68.

Jackson, E.L., Olive, K.P., Tuveson, D.A., Bronson, R., Crowley, D., Brown, M., and Jacks, T. (2005). The differential effects of mutant p53 alleles on advanced murine lung cancer. Cancer Res. *65*, 10280–10288.

Jackson, E.L., Willis, N., Mercer, K., Bronson, R.T., Crowley, D., Montoya, R., Jacks, T., and Tuveson, D.A. (2001). Analysis of lung tumor initiation and progression using conditional expression of oncogenic K-Ras. Genes Dev. *15*, 3243–3248.

Jamal-Hanjani, M., Wilson, G.A., McGranahan, N., Birkbak, N.J., Watkins, T.B.K., Veeriah, S., Shafi, S., Johnson, D.H., Mitter, R., Rosenthal, R., et al.

(2017). Tracking the evolution of non-small-cell lung cancer. N. Engl. J. Med. *376*, 2109–2121.

Ji, H., Ramsey, M.R., Hayes, D.N., Fan, C., McNamara, K., Kozlowski, P., Torrice, C., Wu, M.C., Shimamura, T., Perera, S.A., et al. (2007). LKB1 modulates lung cancer differentiation and metastasis. Nature *448*, 807–810.

Jones, M.G., Khodaverdian, A., Quinn, J.J., Chan, M.M., Hussmann, J.A., Wang, R., Xu, C., Weissman, J.S., and Yosef, N. (2020). Inference of single-cell phylogenies from lineage tracing data using Cassiopeia. Genome Biol. *21*, 92.

Jones, M., Rosen, Y., and Yosef, N. (2022). Interactive, integrated analysis of single-cell transcriptomic and phylogenetic data with PhyloVision. Cell Reports Methods *2*, 100200.

Kalhor, R., Kalhor, K., Mejia, L., Leeper, K., Graveline, A., Mali, P., and Church, G.M. (2018). Developmental barcoding of whole mouse via homing CRISPR. Science *361*, eaat9804.

Kerk, S.A., Papagiannakopoulos, T., Shah, Y.M., and Lyssiotis, C.A. (2021). Metabolic networks in mutant KRAS-driven tumours: tissue specificities and the microenvironment. Nat. Rev. Cancer *21*, 510–525.

Kim, C., Gao, Ruli, Sei, E., Brandt, R., Hartman, J., Hatschek, T., Crosetto, N., Foukakis, T., and Navin, N.E. (2018). Chemoresistance evolution in triple-negative breast cancer delineated by single-cell sequencing. Cell *173*, 879–893.e13.

Klein, C.A. (2009). Parallel progression of primary tumours and metastases. Nat. Rev. Cancer *9*, 302–312.

La Manno, G., Soldatov, R., Zeisel, A., Braun, E., Hochgerner, H., Petukhov, V., Lidschreiber, K., Kastriti, M.E., Lönnerberg, P., Furlan, A., et al. (2018). RNA velocity of single cells. Nature *560*, 494–498.

LaFave, L.M., Kartha, V.K., Ma, S., Meli, K., Del Priore, I., Lareau, C., Naranjo, S., Westcott, P.M.K., Duarte, F.M., Sankar, V., et al. (2020). Epigenomic State transitions characterize tumor progression in mouse lung adenocarcinoma. Cancer Cell *38*, 212–228.e13.

Lan, X., Jörg, D.J., Cavalli, F.M.G., Richards, L.M., Nguyen, L.V., Vanner, R.J., Guilhamon, P., Lee, L., Kushida, M.M., Pellacani, D., et al. (2017). Fate mapping of human glioblastoma reveals an invariant stem cell hierarchy. Nature *549*, 227–232.

Laughney, A.M., Hu, J., Campbell, N.R., Bakhoum, S.F., Setty, M., Lavallée, V.-P., Xie, Y., Masilionis, I., Carr, A.J., Kottapalli, S., et al. (2020). Regenerative lineages and immune-mediated pruning in lung cancer metastasis. Nat. Med. *26*, 259–269.

Lee, J.H., Daugharthy, E.R., Scheiman, J., Kalhor, R., Yang, J.L., Ferrante, T.C., Terry, R., Jeanty, S.S., Li, C., Amamoto, R., et al. (2014). Highly multiplexed subcellular RNA sequencing in situ. Science *343*, 1360–1363.

Leeman, K.T., Christine, M.F., and Carla, F.K. (2014). "Lung Stem and Progenitor Cells in Tissue Homeostasis and Disease". Current Topics in Developmental Biology *107*, 207–233.

Li, A., Herbst, R.H., Canner, D., Schenkel, J.M., Smith, O.C., Kim, J.Y., Hillman, M., Bhutkar, A., Cuoco, M.S., Rappazzo, C.G., et al. (2019). IL-33 signaling alters regulatory T cell diversity in support of tumor development. Cell Rep. *29*, 2998–3008.e8.

Livet, J., Weissman, T.A., Kang, H., Draft, R.W., Lu, J., Bennis, R.A., Sanes, J.R., and Lichtman, J.W. (2007). Transgenic strategies for combinatorial expression of fluorescent proteinS in the nervous system. Nature *450*, 56–62.

Lopez, R., Regier, J., Cole, M.B., Jordan, M.I., and Yosef, N. (2018). Deep generative modeling for single-cell transcriptomics. Nat. Methods *15*, 1053–1058.

Ludwig, L.S., Lareau, C.A., Ulirsch, J.C., Christian, E., Muus, C., Li, L.H., Pelka, K., Ge, W., Oren, Y., Brack, A., et al. (2019). Lineage tracing in humans enabled by mitochondrial mutations and single-cell genomics. Cell *176*, 1325–1339.e22.

Ma, S., Zhang, B., LaFave, L.M., Earl, A.S., Chiang, Z., Hu, Y., Ding, J., Brack, A., Kartha, V.K., Tay, T., et al. (2020). Chromatin potential identified by shared single-cell profiling of RNA and chromatin. Cell *183*, 1103–1116.e20.

Malikic, S., Jahn, K., Kuipers, J., Sahinalp, S.C., and Beerenwinkel, N. (2019). Integrative inference of subclonal tumour evolution from single-cell and bulk sequencing data. Nat. Commun. *10*, 2750.

Marjanovic, N.D., Hofree, M., Chan, J.E., Canner, D., Wu, K., Trakala, M., Hartmann, G.G., Smith, O.C., Kim, J.Y., and Evans, K.V. (2020). Emergence of a high-plasticity cell state during lung cancer evolution. Cancer Cell *38*, 229–246.e13.

Maynard, A., McCoach, C.E., Rotow, J.K., Harris, L., Haderk, F., Kerr, D.L., Yu, E.A., Schenk, E.L., Tan, W., Zee, A., et al. (2020). Therapy-induced evolution of human lung cancer revealed by single-cell RNA sequencing. Cell *182*, 1232–1251.e22.

McFadden, D.G., Politi, K., Bhutkar, A., Chen, F.K., Song, X., Pirun, M., Santiago, P.M., Kim-Kiselak, C., Platt, J.T., Lee, E., et al. (2016). Mutational landscape of EGFR-, MYC-, and Kras-driven genetically engineered mouse models of lung adenocarcinoma. Proc. Natl. Acad. Sci. USA *113*, E6409–E6417.

McGinnis, C.S., Patterson, D.M., Winkler, J., Conrad, D.N., Hein, M.Y., Srivastava, V., Hu, J.L., Murrow, L.M., Weissman, J.S., Werb, Z., et al. (2019). MULTI-Seq: sample multiplexing for single-cell RNA sequencing using lipid-tagged indices. Nat. Methods *16*, 619–626.

McGranahan, N., and Swanton, C. (2017). Clonal heterogeneity and tumor evolution: past, present, and the future. Cell *168*, 613–628.

McInnes, L., Healy, J., and Melville, J. (2018). UMAP: uniform manifold approximation and projection for dimension reduction. arXiv. 1802.03426.

McKenna, A., Findlay, G.M., Gagnon, J.A., Horwitz, M.S., Schier, A.F., and Shendure, J. (2016). Whole-organism lineage tracing by combinatorial and cumulative genome editing. Science *353*, p.aaf7907.

McKenna, A., and Gagnon, J.A. (2019). Recording development with single cell dynamic lineage tracing. Development *146*, dev169730. https://doi.org/10.1242/dev.169730.

Mimitou, E.P., Lareau, C.A., Chen, K.Y., Zorzetto-Fernandes, A.L., Hao, Y., Takeshima, Y., Luo, W., Huang, T.S., Yeung, B.Z., Papalexi, E., et al. (2021). Scalable, multimodal profiling of chromatin accessibility, gene expression and protein levels in single cells. Nat. Biotechnol. *39*, 1246–1258.

Murray, C.W., Brady, J.J., Tsai, M.K., Li, C., Winters, I.P., Tang, R., Andrejka, L., Ma, R.K., Kunder, C.A., Chu, P., et al. (2019). An LKB1–SIK axis suppresses lung tumor growth and controls differentiation. Cancer Discov. *9*, 1590–1605.

Neerven, S.M. van, de Groot, N.E., Nijman, L.E., Scicluna, B.P., van Driel, M.S., Lecca, M.C., Warmerdam, D.O., Kakkar, V., Moreno, L.F., Vieira Braga, F.A., et al. (2021). Apc-mutant cells act as supercompetitors in intestinal tumour initiation. Nature *594*, 436–441.

Neftel, C., Laffy, J., Filbin, M.G., Hara, T., Shore, M.E., Rahme, G.J., Richman, A.R., Silverbush, D., Shaw, M.L., Hebert, C.M., et al. (2019). An integrative model of cellular states, plasticity, and genetics for glioblastoma. Cell *178*, 835–849.e21.

Neher, R.A., Russell, C.A., and Shraiman, B.I. (2014). Predicting evolution from the shape of genealogical trees. eLife *3*, e03568.

Nguyen, D.X., Chiang, A.C., Zhang, X.H.-F., Kim, J.Y., Kris, M.G., Ladanyi, M., Gerald, W.L., and Massagué, J. (2009). WNT/TCF signaling through LEF1 and HOXB9 mediates lung adenocarcinoma metastasis. Cell *138*, 51–62.

Nowell, P.C. (1976). The clonal evolution of tumor cell populations. Science *194*, 23–28.

Ouardini, K., Lopez, R., Jones, M.G., Prillo, S., Zhang, R., Jordan, M.I., and Yosef, N. (2021). Reconstructing unobserved cellular states from paired single-cell lineage tracing and transcriptomics data. Preprint at bioRxiv. https://doi.org/10.1101/2021.05.28.446021.

Park, J., Lim, J.M., Jung, I., Heo, S.-J., Park, J., Chang, Y., Kim, H.K., Jung, D., Yu, J.H., Min, S., et al. (2021). Recording of elapsed time and temporal information about biological events using Cas9. Cell *184*, 1047–1063.e23.

Parsons, M.J., Tammela, T., and Dow, L.E. (2021). WNT as a driver and dependency in cancer. Cancer Discov. *11*, 2413–2429.

Patel, A.P., Tirosh, I., Trombetta, J.J., Shalek, A.K., Gillespie, S.M., Wakimoto, H., Cahill, D.P., Nahed, B.V., Curry, W.T., Martuza, R.L., et al. (2014). Single-cell RNA-Seq highlights intratumoral heterogeneity in primary glioblastoma. Science *344*, 1396–1401.

Pei, W., Feyerabend, T.B., Rössler, J., Wang, X., Postrach, D., Busch, K., Rode, I., Klapproth, K., Dietlein, N., Quedenau, C., et al. (2017). Polylox barcoding reveals haematopoietic stem cell fates realized in vivo. Nature *548*, 456–460.

Pierce, S.E., Granja, J.M., Corces, M.R., Brady, J.J., Tsai, M.K., Pierce, A.B., Tang, R., Chu, P., Feldser, D.M., Chang, H.Y., et al. (2021). LKB1 inactivation modulates chromatin accessibility to drive metastatic progression. Nat. Cell Biol. *23*, 915–924.

Podsypanina, K., Du, Y.-C.N., Jechlinger, M., Beverly, L.J., Hambardzumyan, D., and Varmus, H. (2008). Seeding and propagation of untransformed mouse mammary cells in the lung. Science *321*, 1841–1844.

Potter, N.E., Ermini, L., Papaemmanuil, E., Cazzaniga, G., Vijayaraghavan, G., Titley, I., Ford, A., Campbell, P., Kearney, L., and Greaves, M. (2013). Single-cell mutational profiling and clonal phylogeny in cancer. Genome Res. *23*, 2115–2125.

Powles, T., Assaf, Z.J., Davarpanah, N., Banchereau, R., Szabados, B.E., Yuen, K.C., Grivas, P., Hussain, M., Oudard, S., Gschwend, J.E., et al. (2021). ctDNA guiding adjuvant immunotherapy in urothelial carcinoma. Nature *595*, 432–437.

Premsrirut, P.K., Dow, L.E., Kim, S.Y., Camiolo, M., Malone, C.D., Miething, C., Scuoppo, C., Zuber, J., Dickins, R.A., Kogan, S.C., et al. (2011). A rapid and scalable system for studying gene function in mice using conditional RNA interference. Cell *145*, 145–158.

Quinn, J.J., Jones, M.G., Okimoto, R.A., Nanjo, S., Chan, M.M., Yosef, N., Bivona, T.G., and Weissman, J.S. (2021). Single-cell lineages reveal the rates, routes, and drivers of metastasis in cancer xenografts. Science *371*, p.eabc1944.

Quintanal-Villalonga, Á., Chan, J.M., Yu, H.A., Pe'er, D., Sawyers, C.L., Sen, T., Rudin, C.M., and Charles, L. (2020). Nat. Rev. Clin. Oncol. *17*, 360–371.

Raj, B., Wagner, D.E., McKenna, A., Pandey, S., Klein, A.M., Shendure, J., Gagnon, J.A., and Schier, A.F. (2018). Simultaneous single-cell profiling of lineages and cell types in the vertebrate brain. Nat. Biotechnol. *36*, 442–450.

Rathert, P., Roth, M., Neumann, T., Muerdter, F., Roe, J.-S., Muhar, M., Deswal, S., Cerny-Reiterer, S., Peter, B., Jude, J., et al. (2015). Transcriptional plasticity promotes primary and acquired resistance to BET inhibition. Nature *525*, 543–547.

Rhim, A.D., Mirek, E.T., Aiello, N.M., Maitra, A., Bailey, J.M., McAllister, F., Reichert, M., Beatty, G.L., Rustgi, A.K., Vonderheide, R.H., et al. (2012). EMT and dissemination precede pancreatic tumor formation. Cell *148*, 349–361.

Rogers, Z.N., McFarland, C.D., Winters, I.P., Naranjo, S., Chuang, C.-H., Petrov, D., and Winslow, M.M. (2017). A quantitative and multiplexed approach to uncover the fitness landscape of tumor suppression in vivo. Nat. Methods *14*, 737–742.

Rogers, Z.N., McFarland, C.D., Winters, I.P., Seoane, J.A., Brady, J.J., Yoon, S., Curtis, C., Petrov, D.A., and Winslow, M.M. (2018). Mapping the in vivo fitness landscape of lung adenocarcinoma tumor suppression in mice. Nat. Genet. *50*, 483–486.

Van den Berge, Koen, Roux de Bézieux, H., Street, K., Saelens, W., Cannoodt, R., Saeys, Y., Dudoit, S., and Clement, L. (2020). Trajectory-based differential expression analysis for single-cell sequencing data. Nat. Commun. *11*, 1–13.

Saitou, N., and Nei, M. (1987). The neighbor-joining method: A new method for reconstructing phylogenetic trees. Mol. Biol. Evol. *4*, 406–425.

Salehi, S., Kabeer, F., Ceglia, N., Andronescu, M., Williams, M.J., Campbell, K.R., Masud, T., Wang, B., Biele, J., Brimhall, J., et al. (2021). Clonal fitness inferred from time-series modelling of single-cell cancer genomes. Nature *595*, 585–590.

Satas, G., Zaccaria, S., Mon, G., and Raphael, B.J. (2020). SCARLET: single-cell tumor phylogeny inference with copy-number constrained mutation losses. Cell Syst *10*, 323–332.e8.

Schepers, A.G., Snippert, H.J., Stange, D.E., van den Born, M., van Es, J.H., van de Wetering, M., and Clevers, H. (2012). Lineage tracing reveals Lgr5+ stem cell activity in mouse intestinal adenomas. Science *337*, 730–735.

Schwartz, R., and Schäffer, A.A. (2017). The evolution of tumour phylogenetics: principles and practice. Nat. Rev. Genet. *18*, 213–229.

Shaffer, S.M., Dunagin, M.C., Torborg, S.R., Torre, E.A., Emert, B., Krepler, C., Beqiri, M., Sproesser, K., Brafford, P.A., Xiao, M., et al. (2017). Rare cell variability and drug-induced reprogramming as a mode of cancer drug resistance. Nature *546*, 431–435.

Sherr, C.J. (2004). Principles of tumor suppression. Cell *116*, 235–246.

Simeonov, KamenP., Byrns, C.N., Clark, M.L., Norgard, R.J., Martin, B., Stanger, B.Z., Shendure, J., McKenna, A., and Lengner, C.J. (2021). Single-cell lineage tracing of metastatic cancer reveals selection of hybrid EMT states. Cancer Cell *39*, 1150–1162.e9.

Sinjab, A., Han, G., Treekitkarnmongkol, W., Hara, K., Brennan, P.M., Dang, M., Hao, D., Wang, R., Dai, E., Dejima, H., et al. (2021). Resolving the spatial and cellular architecture of lung adenocarcinoma by multiregion single-cell sequencing. Cancer Discov. *11*, 2506–2523.

Sjöblom, T., Jones, S., Wood, L.D., Parsons, D.W., Lin, J., Barber, T.D., Mandelker, D., Leary, R.J., Ptak, J., Silliman, N., et al. (2006). The Consensus coding sequences of human breast and colorectal cancers. Science *314*, 268–274.

Skoulidis, F., Byers, L.A., Diao, L., Papadimitrakopoulou, V.A., Tong, P., Izzo, J., Behrens, C., Kadara, H., Parra, E.R., Canales, J.R., et al. (2015). Co-occurring genomic alterations define major subsets of KRAS-mutant lung adenocarcinoma with distinct biology, immune profiles, and therapeutic vulnerabilities. Cancer Discov. *5*, 860–877.

Sottoriva, A., Kang, H., Ma, Z., Graham, T.A., Salomon, M.P., Zhao, Junsong, Marjoram, P., Siegmund, K., Press, M.F., Shibata, D., et al. (2015). A big bang model of human colorectal tumor growth. Nat. Genet. *47*, 209–216.

Spanjaard, B., Hu, B., Mitic, N., Olivares-Chauvet, P., Janjuha, S., Ninov, N., and Junker, J.P. (2018). Simultaneous lineage tracing and cell-type identification using CRISPR-Cas9-induced genetic scars. Nat. Biotechnol. *36*, 469–473.

Speidel, L., Forest, M., Shi, S., and Myers, S.R. (2019). A method for genome-wide genealogy estimation for thousands of samples. Nat. Genet. *51*, 1321–1329.

Stadler, T., Pybus, O.G., and Stumpf, M.P.H. (2021). Phylodynamics for cell biologists. Science *371*, p.eaah6266.

Stickels, R.R., Murray, E., Kumar, P., Li, J., Marshall, J.L., Di Bella, D.J., Arlotta, P., Macosko, E.Z., and Chen, F. (2021). Highly sensitive spatial transcriptomics at near-cellular resolution with slide-seqV2. Nat. Biotechnol. *39*, 313–319.

Tammela, T., and Sage, J. (2020). Investigating tumor heterogeneity in mouse models. Annu. Rev. Cancer Biol. *4*, 99–119.

Tammela, T., Sanchez-Rivera, F.J., Cetinbas, N.M., Wu, K., Joshi, N.S., Helenius, K., Park, Y., Azimi, R., Kerper, N.R., Wesselhoeft, R.A., et al. (2017). A Wnt-producing niche drives proliferative potential and progression in lung adenocarcinoma. Nature *545*, 355–359.

Tang, W., and Liu, D.R. (2018). Rewritable multi-event analog recording in bacterial and mammalian cells. Science *360*, p.eaap8992.

Tarabichi, M., Salcedo, A., Deshwar, A.G., Ni Leathlobhair, M., Wintersinger, J., Wedge, D.C., Van Loo, P., Morris, Q.D., and Boutros, P.C. (2021). A practical guide to cancer subclonal reconstruction from DNA sequencing. Nat. Methods *18*, 144–155.

Tavazoie, M.F., Pollack, I., Tanqueco, R., Ostendorf, B.N., Reis, B.S., Gonsalves, F.C., Kurth, I., Andreu-Agullo, C., Derbyshire, M.L., Posada, J., et al. (2018). LXR/ApoE activation restricts innate immune suppression in cancer. Cell *172*, 825–840.e18.

Traag, V.A., Waltman, L., and van Eck, N.J. (2019). From Louvain to Leiden: guaranteeing well-connected communities. Sci. Rep. *9*, 5233.

Trapnell, C., Cacchiarelli, D., Grimsby, J., Pokharel, P., Li, S., Morse, M., Lennon, N.J., Livak, K.J., Mikkelsen, T.S., and Rinn, J.L. (2014). The dynamics and regulators of cell Fate decisions are revealed by pseudotemporal ordering of single cells. Nat. Biotechnol. *32*, 381–386.

Tritschler, S., Büttner, M., Fischer, D.S., Lange, M., Bergen, V., Lickert, H., and Theis, F.J. (2019). Concepts and limitations for learning developmental trajectories from single cell genomics. Development *146*. p.dev, 170506.

Turajlic, S., and Swanton, C. (2016). Metastasis as an evolutionary process. Science *352*, 169–175.

Vogelstein, B., Papadopoulos, N., Velculescu, V.E., Zhou, S., Diaz, L.A., and Kinzler, K.W. (2013). Cancer genome landscapes. Science *339*, 1546–1558.

Vogelstein, B., Fearon, E.R., Hamilton, S.R., Kern, S.E., Preisinger, A.C., Leppert, M., Nakamura, Y., White, R., Smits, A.M., and Bos, J.L. (1988). Genetic alterations during colorectal-tumor development. N. Engl. J. Med. *319*, 525–532.

Wagner, D.E., and Klein, A.M. (2020). Lineage tracing meets single-cell omics: opportunities and challenges. Nat. Rev. Genet. *21*, 410–427.

Wagner, D.E., Weinreb, C., Collins, Z.M., Briggs, J.A., Megason, S.G., and Klein, A.M. (2018). Single-cell mapping of gene expression landscapes and lineage in the zebrafish embryo. Science *360*, 981–987.

Weinberg, R.A. (1991). Tumor suppressor genes. Science *254*, 1138–1146.

Weinreb, C., Rodriguez-Fraticelli, A., Camargo, F.D., and Klein, A.M. (2020). Lineage tracing on transcriptional landscapes links state to Fate during differentiation. Science *367*, p.eaaw3381.

Westcott, P.M.K., Halliwill, K.D., To, M.D., Rashid, M., Rust, A.G., Keane, T.M., Delrosario, R., Jen, K.Y., Gurley, K.E., Kemp, C.J., et al. (2015). The mutational landscapes of genetic and chemical models of kras-driven lung cancer. Nature *517*, 489–492.

Williams, M.J., Werner, B., Heide, T., Curtis, C., Barnes, C.P., Sottoriva, A., and Graham, T.A. (2018). Quantification of subclonal selection in cancer from bulk sequencing data. Nat. Genet. *50*, 895–903.

Winslow, M.M., Dayton, T.L., Verhaak, R.G.W., Kim-Kiselak, C., Snyder, E.L., Feldser, D.M., Hubbard, D.D., DuPage, M.J., Whittaker, C.A., Hoersch, S., et al. (2011). Suppression of lung adenocarcinoma progression by Nkx2-1. Nature *473*, 101–104.

Winters, I.P., Murray, C.W., and Winslow, M.M. (2018). Towards quantitative and multiplexed in vivo functional cancer genomics. Nat. Rev. Genet. *19*, 741–755.

Wolf, F.A., Angerer, P.A., and Theis, F.J. (2018). SCANPY: large-scale single-cell gene expression data analysis. Genome Biol. *19*, 15.

Xu, C., Lopez, R., Mehlman, E., Regier, J., Jordan, M.I., and Yosef, N. (2021). Probabilistic harmonization and annotation of single-cell transcriptomics data with deep generative models. Mol. Syst. Biol. *17*, e9620.

Yan, J., Jiang, Y., Lu, J., Wu, J., and Zhang, M. (2019). Inhibiting of proliferation, migration, and invasion in lung cancer induced by silencing interferon-induced transmembrane Protein 1 (IFITM1). BioMed Res. Int. *2019* (May), 9085435. https://doi.org/10.1155/2019/9085435.

Yuan, S., Norgard, R.J., and Stanger, B.Z. (2019). Cellular plasticity in cancer. Cancer Discov. *9*, 837–851.

Zhang, W., Bado, I.L., Hu, J., Wan, Y.-W., Wu, L., Wang, H., Gao, Y., Jeong, H.H., Xu, Z., Hao, X., et al. (2021). The bone microenvironment invigorates metastatic seeds for further dissemination. Cell *184*, 2471–2486.e20.

Zheng, Y., Cecile, C., Leanne, C.S., Chris, A.-C., Dedeepya, V., Tim, D.K., Marty, B., et al. (2013). "A Rare Population of CD24+ ITGB4+ Notchhi Cells Drives Tumor Propagation in NSCLC and Requires Notch3 for Self-Renewal". Cancer Cell *24*, 59–74.

Zhou, Y., Rideout, W.M., 3rd, Zi, T., Bressel, A., Reddypalli, S., Rancourt, R., Woo, J.-K., Horner, J.W., Chin, L., Chiu, M.I., et al. (2010). Chimeric mouse tumor models reveal differences in pathway activation between ERBB family- and KRAS-dependent lung adenocarcinomas. Nat. Biotechnol. *28*, 71–78.

STAR★METHODS

KEY RESOURCES TABLE

REAGENT or RESOURCE	SOURCE	IDENTIFIER
Chemicals, enzymes, and antibodies		
Collagenase Type IV	Thermo Fisher Scientific	Cat#: 17104019
Dispase	Thermo Fisher Scientific	Cat#: 17105041
Trypsin	Thermo Fisher Scientific	Cat#: 25200056
ACK	Thermo Fisher Scientific	Cat#: A1049201
DNase I	Millipore Sigma	SKU 11284932001
UltraPure BSA	Thermo Fisher Scientific	Cat#: AM2618
Anti-mouse CD45 Monoclonal Antibody, APC	BioLegend	Cat#: 103111; RRID:AB_312976
Anti-mouse CD31 Monoclonal Antibody, APC	BioLegend	Cat#102410; RRID:AB_312905
Anti-mouse CD11b Monoclonal Antibody, APC	BioLegend	Cat#: 101212; RRID:AB_312795
Anti-mouse F4/80 Monoclonal Antibody, APC	BioLegend	Cat#: 123116; RRID:AB_893481
Anti-mouse Ter119 Monoclonal Antibody, APC	BioLegend	Cat#: 116212; RRID:AB_313713
MULTI-seq lipid anchor and co-anchor	McGinnis et al. 2019	Generated by the Gartner lab
Knockout DMEM	Gibco	Cat#10829-018
Fetal Bovine Serum	Hyclone	Cat#SV30014
GlutaMax	Gibco	Cat#35050-061
Non-essential amino acids	Thermo Fisher Scientific	Cat#11140050
2-mercaptoethanol	Sigma	Cat#M-7522
Recombinant Mouse LIF Protein	Millipore	Cat#ESG1107
Critical commercial assays		
SPRI Bead	Beckman Coulter	A63881
KAPA HiFi HotStart ReadyMix	KAPA Biosystems	KK2601
Chromium Single Cell 3' Library & Gel Bead Kit v2	10x Genomics	PN-120237
Chromium Single Cell A Chip Kit	10x Genomics	PN-1000009
Chromium i7 Multiplex Kit	10x Genomics	PN-120262
Qiagen Plasmid Giga kit	Qiagen	cat. no. 12191
Site-directed mutagenesis kit	New England Biolabs	E0554S
Agilent Technologies High Sensitivity DNA Kit	Fisher Scientific	NC1738319
Super PiggyBac transposase	System Biosciences	PB210PA-1
Deposited data		
Raw data from KP-Tracer mice (scRNA-seq, MULTI-seq, target site, and Lenti-Cre-BC)	This manuscript	NCBI BioProject: PRJNA803321
Processed data for KP-Tracer tumors	This manuscript	https://doi.org/10.5281/zenodo.5847461
Interactive VISION and PhyloVision Reports	This manuscript	https://doi.org/10.5281/zenodo.5888895
Oligonucleotides		
oDYT011 sgNT oligo top tTAGCTCTtAAACCGCGGAGCCGAATACCTCGCCAACAag	This manuscript	N/A
oDYT012 sgNT oligo bottom TTGGCGAGGTATTCGGCTCCGCGGTTTaAGAGC	This manuscript	N/A
oDYT013 sgLkb1 oligo top tTAGCTCTtAAACTTGTGACTGCGGCCCACCACCAACAag	This manuscript	N/A
oDYT014 sgLkb1 oligo bottom TTGGTGGTGGGCCGCAGTCACAAGTTTaAGAGC	This manuscript	N/A

(Continued on next page)

Continued

REAGENT or RESOURCE	SOURCE	IDENTIFIER
oDYT015 sgApc oligo top tTAGCTCTtAAACCGGAGTGAAACTACGCTCAAcCAACAag	This manuscript	N/A
oDYT016 sgApc oligo bottom TTGgTTGAGCGTAGTTTCACTCCGGTTTaAGAGC	This manuscript	N/A
oDYT019 gibson_3xsg_piggy FWD GACTGGATTCCTTTTTTAGGGCCCATTGGTctagaCGTGA CCGAGCTTGTC	This manuscript	N/A
oDYT020 gibson_3xsg_piggy REV CGGGGAAAAAGCCATGTTTAAACGcggccgcctaatggatcct agtactcgaG	This manuscript	N/A
oDYT021 gibson_TS1.1gB_ FWD catggacgagctgtacaagtaaTGAATTAATtaaGTCACGAATCC AGCTAGCTG	This manuscript	N/A
oDYT022 gibson_TS1.1gB_ REV CCATTATAAGCTGCAATAAACAAGTTTCCTTAGCCGCTA ATAGGTGAGCAGTTAACACCTGCAGGAGCGATGG	This manuscript	N/A
oDYT023-030 10x_target site amplification_primer_F AATGATACGGCGACCACCGAGATCTACACNNNNNNNN TCTTTCCCTACACGACGCTCTTCCGATCT	This manuscript	N/A
oDYT031-038 10x_target site amplification_primer_R CAAGCAGAAGACGGCATACGAGANNNNNNNNTGTCTC GTGGGCTCGGAGATGTGTATAAGAGACAGAATCCAGC TAGCTGTGCAGC	This manuscript	N/A
oDYT039 MULTIseq spike-in CCTTGGCACCCGAGAATTCC	This manuscript	N/A
oDYT040 MULTIseq P5 AATGATACGGCGACCACCGAGATCTACACTCTTTCCCTA CACGACGCTCTTCCGATCT	This manuscript	N/A
oDYT041-48 MULTIseq P7 CAAGCAGAAGACGGCATACGAGATNNNNNNNNGTGACT GGAGTTCCTTGGCACCCGAGAATTCC	This manuscript	N/A
oDYT049 P5 universal for Lenti-BC AATGATACGGCGACCACCGAGATCTACACTCTTTCCCTA CACGACGCTCTTCCGATCT	This manuscript	N/A
oDYT050-059 P7 for Lenti-BC CAAGCAGAAGACGGCATACGAGATNNNNNNNNAGTCTC GTGGGCTCGGAGATGTGTATAAGAGACAGGACCTCCCT AGCAAACTGGGGCACAAG	This manuscript	N/A
Software and code		
10X cellranger	https://support.10xgenomics.com/ single-cell-gene-expression/ software/pipelines/latest/installation	v2.1.1
deMULTIplex	https://github.com/chris-mcginnis- ucsf/MULTI-seq	v1.0.2
inferCNV	https://github.com/broadinstitute/ infercnv	v1.11.1
Scanpy	https://github.com/theislab/scanpy	1.7.0rc1
Jungle	https://github.com/felixhorns/jungle	N/A
Hotspot	DeTomaso & Yosef, 2021	v0.9.1
Evolutionary Coupling	This study	https://doi.org/10.5281/zenodo.6354596
Phylotime	This study	https://doi.org/10.5281/zenodo.6354596
EffectivePlasticity	This study	https://doi.org/10.5281/zenodo.6354596
Subclonal expansion detection	This study	https://doi.org/10.5281/zenodo.6354596
Cassiopeia tree reconstruction algorithms	Jones et al, 2020 and this study	https://doi.org/10.5281/zenodo.6354596

RESOURCE AVAILABILITY

Lead contact
Further information and requests for resources and reagents should be directed to and will be fulfilled by the Lead Contact Jonathan Weissman (weissman@wi.mit.edu).

Materials availability
Plasmids generated in this study are being submitted to Addgene. All unique/stable reagents generated in this study are available from the lead contact with a completed Materials Transfer Agreement.

Data and code availability
Raw single-cell RNA-sequencing data has been deposited at the NCBI Sequence Read Archive database and are publicly available as of the date of the publication. Accession numbers are listed in the key resources table. Processed single-cell data, reconstructed phylogenies, derived statistics, interactive VISION (DeTomaso et al., 2019) and PhyloVision (Jones et al., 2022) reports have been deposited at Zenodo and are publicly available as of the date of the publication. DOIs are listed in the key resources table.

All original code is available on Github (https://github.com/mattjones315/KPTracer-release) and has been deposited at Zenodo and is publicly available as of the date of the publication. DOIs are listed in the key resources table.

Any additional information required to reanalyze the data reported in this paper is available from the lead contact upon request.

EXPERIMENTAL MODEL AND SUBJECT DETAILS

Chimeric lineage tracing mouse model
All mouse experiments described in this study were approved by the Massachusetts Institute of Technology Institutional Animal Care and Use Committee (IACUC) (institutional animal welfare assurance no. A-3125-01). A male mouse embryonic stem cell (mESC) line harboring the conditional alleles $Kras^{LSL-G12D/+}$ and $Trp53^{fl/fl}$ (KP) was engineered with the lineage tracer cassettes. The engineered and selected mESC clones were injected into blastocysts from albino B6 or CD1 background for chimera making as previously described (Zhou et al. 2010). We chose to use the chimeric mice strategy because the multiple, random integration of lineage tracing target sites in the genome makes it challenging for breeding stable strains. Both male and female mice with more than 10% chimerism based on coat color were used in this study. Tumors were initiated by intratracheal infection of mice with lentiviral vectors expressing Cre recombinase (DuPage, Dooley, and Jacks 2009). Five total mESC clones were used in this study to avoid idiosyncrasy in clonal behavior and analyses were performed on all tumors combined. Lenti-Cre-BC vector was co-transfected with packaging vectors (delta8.2 and VSV-G) into HEK-293T cells using polyethylenimine (Polysciences). The supernatant was collected at 48h posttransfection, ultracentrifuged at 25,000 r.p.m. for 90 min at 4C, and resuspended in phosphate-buffered saline (PBS). 8-12-week-old chimeras were infected intratracheally with lentiviral vectors, including lenti-Cre-BC-sgNT ($2x10^7$ PFU) or lenti-Cre-BC-sgLkb1 ($4x10^6$ PFU) or lenti-Cre-BC-sgApc ($1x10^7$ PFU) to achieve similar aging time after tumor initiation.

METHOD DETAILS

Lenti-sgRNA-Cre-Barcode vector
The lenti_sgRNA_Cre_barcode vector was derived from a previously described Perturb-seq lentiviral vector (Adamson et al., 2016), pBA439, with the following changes: the two loxP sites were removed by site-directed mutagenesis (SDM) using oDYT001 and oDYT002 followed by oDYT009 and oDYT010; the Puro-BFP was removed using restriction sites NheI and PacI and was replaced by Cre that was PCR amplified using oDYT003 and oDYT004 via Gibson assembly; a ubiquitous chromatin opening element (UCOE) that was PCR amplified using oDYT005 and oDYT006 was introduced using restriction sites NsiI and NotI via Gibson assembly. oDYT007 and oDYT008 (containing EcoRI and SbfI sites for subsequent barcode cloning) were then annealed and ligated using restriction sites BclI and PacI. Three different sgRNAs of interest were then cloned into the resulting vector using pairs of top and bottom strand sgRNA oligos: sgNT (non-targeting) (oDYT011 and oDYT012), sgLkb1 (oDYT013 and oDYT014), and sgApc (oDYT015 and oDYT016) were each annealed and ligated using restriction sites BlpI and BstXI to form pDYT003, pDYT004, and pDYT005 respectively. These sgRNAs have been used and validated previously (Rogers et al. 2017, 2018). Finally, a whitelist barcode oligo pool consisting of 249,959 unique 16-nucleotide barcodes where every barcode has a Levenshtein distance of >3 from every other barcode was designed. The whitelist barcode library was PCR amplified then introduced at the 3'UTR region of Cre in each of the three constructs using restriction sites EcoRI and SbfI.

Lineage tracer vector (Target site & triple sgRNAs)
The lineage tracer vectors pDYT001 and pDYT002 were derived from previously described target site plasmids, PCT 60-62 (Chan et al. 2019; Quinn et al. 2021; Jones et al. 2020). A loxP site was first removed from both PCT61 and PCT62 using oDYT017 and

oDYT018 via site-directed mutagenesis. The triple sgRNA cassettes driven by distinct U6 promoters in PCT61 and PCT62 were then PCR amplified using oDYT019 and oDYT020 and introduced into the PCT60 backbone using restriction sites XbaI and NotI via Gibson assembly. Finally, the target site barcode library was PCR amplified from a previously described gene fragment from PCT48 (Jones et al. 2020), using oDYT021 and oDYT022 and introduced into the two resulting vectors above using restriction sites PacI and HpaI to form pDYT001 and pDYT002, which contain the triple guide cassette from PCT61 and PCT62 respectively. The target site library consists of a 14-bp random integration barcode and three target sites (ade2, bri1, whtB), which are complementary to the three sgRNAs.

Lineage tracing embryonic stem cell engineering

KP*17 is an embryonic stem (ES) cell line derived from C57BL/6-129/Sv F1 background engineered with conditional alleles $Kras^{LSL\_G12D/+}; p53^{fl/fl}$. ES cells were maintained with JM8 media (500mL: 82.9% Knockout DMEM (Gibco Cat#10829-018), 15% FBS (Hyclone Cat#SV30014), 1% GlutaMax (Gibco Cat#35050-061), 1% Non-essential amino acids (Thermo Fisher Scientific Cat#11140050), 0.1% 2-mercaptoethanol (Sigma Cat#M-7522), 500,000U Recombinant Mouse LIF Protein (Millipore Cat#ESG1107)) with feeders. KP*17 was first targeted using CRISPR-assisted HDR to generate $Rosa26^{LSL-Cas9-P2A-mNeonGreen}$ which was validated for correct targeting by PCR and southern blot and validated for Cas9 activity. The lineage tracing transposon vectors were then introduced together with transposase vector (SBI) by transfection. Three passages after transfection, mESCs were purified by FACS based on mCherry expression and expanded as individual clones.

Target site integration number was quantified as the following: We first used fluorescence-based readout to examine mCherry expression of each ES cell clone in 96 well format, which allowed us to narrow down the ES clone candidates with relatively high expression of mCherry (the reporter of lineage tracer library). Then we used quantitative genomic PCR to count the number of lineage tracer genome integration in each ES cell clone by amplifying the target site regions (oDYT062 and oDYT063) and normalized to a 2N locus, β-actin, in the genome (oDYT060 and oDYT061). Samples were run in triplicates and the reactions were performed on a QuantStudio 6 Flex Real-Time PCR System. In this study, we used the following ES clones in the tumor analysis due to a combination of high chimeric rate and good target site capture: 1D5, 2E1, 1C4, 2F4 and 2H9. Clones 1D5, 1C4 were engineered with pDYT001 and clones 2E1, 2F4 and 2H9 were engineered with pDYT002. All five clones were used independently for generating chimeric mice in this study and no major difference in their lineage tracing performance was observed.

Sample preparation and purification of cancer cells

Tumors were harvested and single-cell suspension was prepared as described in (Chuang et al. 2017) and (Denny et al. 2016). Primary tumors and metastases were dissociated using a digestion buffer (DMEM/F12, 5mM HEPES, DNase, Collagenase IV, Dispase, Trypsin-EDTA) and incubated at 37 °C for 30 min. After dissociation, the samples were quenched with twice the volume of cold quench solution (L-15 medium, FBS, DNase). The cells were then filtered through a 40um cell strainer, spun down at 1000rpm for 5 min, resuspended in 2mL ACK Lysing Buffer, and incubated at room temperature for 1-2 min. Lysis was then stopped with the addition of 10mL DMEM/F12 followed by the spinning down and resuspending of the samples in 1mL FACS buffer. Cells within the pleural fluid were collected immediately after euthanasia by making a small incision in the ventral aspect of the diaphragm followed by introduction of 1 ml of PBS. Cells were stained with antibodies to CD45 (30-F11, Biolegend Cat#103112), CD31 (390, Biolegend Cat#102410), F4/80 (BM8, Biolegend Cat#123116), CD11b (Biolegend Cat#101212) and Ter119 (Biolegend Cat#116212) to exclude cells from the hematopoietic and endothelial lineages. DAPI was used to stain dead cells.

Cells were then labeled by MULTI-seq (McGinnis et al. 2019) in 100ul PBS buffer containing 5ul lipid anchor (50uM) and 2.5ul of barcode oligos (100uM) for 10 min on ice and then 6ul co-anchor (50uM) 10 min on ice. Cells were washed and resuspended with ice-cold FACS buffer to prevent aggregation. DAPI was used to exclude dead cells. FACS Aria sorters (BD Biosciences) were used for cell sorting. Live cancer cells were sorted based on positive expression of mCherry and mNeonGreen as well as negative expression of hematopoietic and endothelial lineage markers (mCherry+, mNeonGreen+, CD45-, CD31-, Ter119-, F4/80-, DAPI-). High purity of the resulting cancer cells has been confirmed in previous studies using similar fluorescent reporter systems (Caswell et al. 2014; Chuang et al. 2017; LaFave et al. 2020). Live normal lung cells were sorted based on negative expression of mNeonGreen, and hematopoietic and endothelial lineage markers. Datasets were further filtered for normal cells analytically via gene expression analyses (see section below "Single-cell transcriptome processing for KP-Tracer NT data") and by removing cells with low editing efficiencies (see section below "Single-cell lineage tracing preprocessing pipeline and quality control filtering").

Single-cell RNAseq library preparation

Single-cell RNA-seq libraries were prepared using 10x_3'_V2 kit according to the 10x user guide, except for the following modification. After cDNA amplification, the cDNA pool is split into two fractions. Half of the cDNA pool are used for scRNA-seq library construction and proceed as directed in the 10x user guide.

Target site library preparation

To prepare the Target Site libraries, the amplified cDNA libraries were further amplified with Target Site-specific primers containing Illumina-compatible adapters and sample indices (oDYT023-oDYT038, forward:5′CAAGCAGAAGACGGCATACGAGATNNNNNN NNGTCTCGTGGGCTCGGAGATGTGTATAAGAGACAGAATCCAGCTAGCTGTGCAGC;

reverse:5′-AATGATACGGCGACCACCGAGATCTACACNNNNNNNNNTCTTTCCCTACACGACGCTCTTCCGATCT; "N" denotes sample indices) using Kapa HiFi ReadyMix (Roche), as described in (Jones et al. 2020). Approximately 30 fmol of template cDNA was used per sample, divided between four identical reactions to avoid possible PCR induced library biases. PCR products were purified and size-selected using SPRI magnetic beads (Beckman) and quantified by BioAnalyzer (Agilent).

MULTI-seq library preparation
The MULTI-seq libraries were prepared as described in (McGinnis et al.), using a custom protocol based on the 10x Genomics Single Cell V2 and CITE-seq workflows. Briefly, the 10x workflow was followed up until complementary DNA amplification, where 1μl of 2.5μM MULTI-seq additive primer (oDYT039) was added to the cDNA amplification master mix. After amplification, MULTIseq barcode and endogenous cDNA fractions were separated using a 0.6X solid phase reversible immobilization (SPRI) size selection. To further purify the MULTI-seq barcode, we increased the final SPRI ratio in the barcode fraction to 3.2X reaction volumes and added 1.8X reaction volumes of 100% isopropanol (Sigma-Aldrich). Eluted barcode cDNA was then quantified using QuBit before library preparation PCR using primers oDYT040 and oDYT041-oDYT048 (95 °C, 5′; 98 °C, 15′; 60 °C, 30′; 72 °C, 30′; eight cycles; 72 °C, 1′; 4 °C hold). TruSeq RPIX:
  5′-CAAGCAGAAGACGGCATACGAGATNNNNNNNGTGACTGGAGTTCCTTGGCACCCGAGAATTCCA-3′
  TruSeq P5 adaptor:
  5′-AATGATACGGCGACCACCGAGATCTACACTCTTTCCCTACACGACGCTCTTCCGATCT-3′
  Following library preparation PCR, the library was size-selected by a 1.6X SPRI clean-up prior to sequencing.

Lenti_Cre_BC library preparation
The Lenti_Cre_BC library amplification protocol was adapted from the Perturb-seq protocol (Adamson et al., 2016). 4 parallel PCR reactions were constructed containing 30ng of final scRNA-seq library as template, oDYT049, and indexed oDYT050-oDYT059, and amplified using KapaHiFi ReadyMix according to the following PCR protocol: (1) 95C for 3 min, (2) 98C for 15 s, then 70C for 10 s (16-24 cycles, depending on final product amount). Reactions were re-pooled during 0.8X SPRI selection, and then fragments of length ~390bp were quantified by bioanalyzer. Lenti_Cre_BC libraries were sequenced as spike-ins alongside the parent RNA-seq libraries.

Sequencing
Sequencing libraries from each sample were pooled to yield approximately equal coverage per cell per sample; scRNA gene expression libraries, Target Site amplicon libraries, MULTI-seq amplicon libraries and Lenti-Cre-BC amplicon libraries were pooled in an approximately 10:3:1:1 molar ratio for sequencing, aiming for at least 70,000 total reads per cell. The libraries were sequenced using a custom sequencing strategy on the NovaSeq platform (Illumina) in order to read the full-length Target Site amplicons. Sample identities were read as indices (I1: 8 cycles, R1: 26 cycles, R2: 290 cycles). Only the first 98 bases per read were used for analysis in the RNA expression libraries to mask the longer reads required to sequence the Target Sites.

QUANTIFICATION AND STATISTICAL ANALYSIS

Single-cell lineage tracing preprocessing pipeline and quality control filtering
Each cell was sequenced in four sequencing libraries: a MULTI-seq library (for identifying sample identity), a target site library (for reconstructing phylogenies), an RNA-seq library (for measuring transcriptional states), and a Lenti-Cre-BC library (for verifying clonal identity). First, the scRNA-seq was processed using the 10X CellRanger pipeline (version 2.1.1) with the mm10 genome build. Then, each cell barcode identified from the 10X pipeline was assigned to a sample using the MULTI-seq library, which was processed with the deMULTIplex R package (version 1.0.2; (McGinnis et al. 2019)). Cells identified as doublets or without a discernible MULTI-seq label were filtered out from downstream analysis.

Next, we processed the Target Site library using the previously described Cassiopeia preprocessing pipeline (Jones et al. 2020; Quinn et al. 2021). Briefly, reads with identical cellBC and UMI were collapsed into a single, error-corrected consensus sequence representing a single-expressed transcript. Consensus sequences were identified within a cell based on a maximum of 10 high-quality mismatches (PHRED score greater than 30) and an edit distance less than 2 (default pipeline parameters). UMIs within a cell reporting more than one consensus sequence were resolved by selecting the consensus sequence with more reads. Each consensus sequence was aligned to the wild-type reference Target Site sequence using a local alignment strategy, and the intBC and indel alleles were called from the alignment. Cells with fewer than 2 reads per UMI on average or fewer than 10 UMIs overall were filtered out. These data are summarized in a molecule table which records the cellBC, UMI, intBC, indel allele, read depth, and other relevant information. Cells that were assigned to Normal lung tissue via a MULTI-seq barcode or had more than 80% of their TargetSites uncut were assigned as "Normal" and not used for downstream lineage reconstruction tasks.

Lenti-Cre-BC libraries were processed using a custom pipeline combining Cassiopeia transcript collapsing, filtering, and quantification and a probabilistic assignment strategy based on the Perturb-seq gRNA calling pipeline (Adamson et al. 2016). First, sequencing reads were collapsed based on a maximum sequence edit distance of 2 and 3 high-quality sequences mismatches

and then cells with fewer than 2 average reads per UMI or 2 UMIs overall were filtered out. Then, Lenti-Cre-BC sequencing reads were compared to the reference sequence and barcode identities were extracted and error-corrected by comparing each extracted barcode to a whitelist of Lenti-Cre-BC sequences, allowing for an edit distance of 3. Then, the count distributions for each unique Lenti-Cre-BC were inspected to remove barcodes that represented background noise. Next, a Lenti-Cre-BC coverage matrix was formed, summarizing the ratio between reads and number of UMIs for each barcode in each cell. Cell coverages were normalized to sum to the median number of coverages across the matrix and log_2-normalized. Finally, with this matrix we adapted the Perturb-seq gRNA calling pipeline to assign barcode identity to cells (Adamson et al. 2016). To do so, we fit a Guassian kernel density function to the coverage distribution for each barcode and then determined a threshold separating "foreground" from "background" based on the relative extrema of the distribution (after removing the 99th percentile of the coverage distribution). Cells whose coverage values fell above the threshold were assigned that particular Lenti-Cre-BC. Cells that received more than one assignment or no assignment at all were marked as ambiguous.

After pre-processing each of these libraries, we called clonal populations, created character matrices, and reconstructed phylogenies for each clonal population (see sections below "Tree Reconstruction with Cassiopeia" and "Calling clonal populations and creating character matrices"). In this, we removed cells that contained few edited sites as this could indicate normal cell contamination (i.e. inactivity of Cas9) and identified consensus sets of intBCs per mES Clone (see section below "Creating a consensus intBC set for mESC clones") that were used for tree reconstruction. After tree reconstruction, we used the Lenti-Cre-BC data to remove cells within each tumor that contained strong evidence of different clonal origin (see section below "Cell Filtering with Lenti-Cre-BC"). Finally, we computed important clone-level quality-control statistics used for identifying clones with sufficient information for phylodynamic analysis (see section below "Tree Quality Control for Fitness Inference").

Across all three datasets (KP, KPL and KPA), this pipeline left us with 72,328 cells with high-quality Target Site information.

Calling clonal populations and creating character matrices

In this study, each clonal population corresponded to a primary tumor or metastatic family. Tumors were identified with two approaches: first, by deconvolution with MULTI-seq (and filtering with Lenti-Cre-BC information; see below in section "Cell Filtering with Lenti-Cre-BC"); and second, by separating cells based on differing intBC sets. In the second approach, we used Cassiopeia to identify non-overlapping intBC sets and classify cells using the "call-lineages" command-line tool. Once clonal populations were identified, consensus intBC sets were identified (see "Creating a consensus intBC set for mESC clones" below). All summarized molecular information for a given cell (cellBC, number of UMI, intBC, indel allele, read depth, etc) along with the assigned clonal identity were summarized in an allele table. Then, character matrices were formed for each clonal population, summarizing mutation information across the N cells in a population and their M cut-sites. Characters (i.e., cut-sites) with more than 80% missing information or containing a mutation that was reported in greater than 98% of cells were filtered out for downstream tree reconstruction.

Creating a consensus intBC set for mESC clones

Given that each mouse is generated from a specific mESC clone, we expected tumors from each mouse would maintain the same set of intBCs as the parental mESC clone. To identify this consensus set of intBCs, we stratified tumors based on which mESC clone they originated from, and within these groups computed the proportion of tumors that reported a given intBC in at least 10% of cells. We determined cutoffs separating reproducible intBCs from irreproducible intBCs for each mES clone separately. These consensus intBC sets were used for downstream reconstruction of phylogenies.

Tree Reconstruction with Cassiopeia

Trees for each clonal population (see "Calling clonal populations and creating character matrices" above) were reconstructed with Cassiopeia-Hybrid (Jones et al. 2020). Briefly, Cassiopeia-Hybrid infers phylogenies by first splitting cells into clusters using a "greedy" criterion (Cassiopeia-Greedy) until a user-defined criteria is met at which point each cluster of cells is reconstructed using a near-optimal Steiner-Tree maximum-parsimony algorithm (Cassiopeia-ILP). We compared the parsimony of trees generated using two different greedy criterions - both criterions employed work by first identifying a mutation and subsequently splitting cells based on whether or not this mutation was observed in a cell. First, we used the original Cassiopeia-Greedy criterion, which identifies mutations to split cells on by using the frequency and probability of mutations. Second we applied a compatibility-based criterion which prioritizes mutations based on character-compatibility (see section "Compatibility-based greedy heuristic for tree reconstruction" below). We proceeded with the more parsimonious tree. In one specific case, (3515_Lkb1_T1), we observed that the lineage tracing alleles were not adequately captured with phylogenetic inference of the primary tumor alone. To handle this, we rebuilt the tree of the tumor-metastasis family and then subset the phylogeny to consist of only the cells from the primary tumor - resulting in a clonal phylogeny that appeared to be better supported by allelic information.

In most inferences, we used indel priors computed with Cassiopeia to select mutations with a Cassiopeia-Greedy algorithm as well as weight edges during the Steiner-Tree search with Cassiopeia-ILP. Generally, we used an LCA-based cutoff to transition between Cassiopeia-Greedy and Cassiopeia-ILP as previously described (Quinn et al. 2021). Clone-specific parameters are reported in Table S1.

Compatibility-based greedy heuristic for tree reconstruction

A rare, but simple case for phylogenetic inference is that of perfect phylogeny in which every character (or cut-site) is binary (that is, can be cut or uncut) and mutates at most one time. In this regime, every pair of characters is "compatible" – that is, given two binary characters i and j, the sets of cells that report a character i as mutated are non-overlapping with the set of cells that report character j as mutated, or one set of cells is completely contained within the other.

In this approach, we used a heuristic, called the compatibility index, to measure how far a pair of characters is from compatibility. To do so, we first "binarized" our character matrices by treating each unique (cut-site, mutation) pair as a binary character. (To note this binarization procedure is possible because of the irreversibility of Cas9 mutations and discussed in our previous work (Jones et al. 2020).) Then, we found the character that had deviated the least from perfect phylogeny, that is violated compatibility the least. To find this character, we first built a directed "compatibility-graph", where individual nodes represented characters and edges between nodes represented deviations from compatibility. Each edge from character i to j was weighted as follows:

$$w_{i,j} \ = \ - \ n_j \log(p_j)$$

where i and j are two incompatible characters, n_j is the number of cells reporting character j, and p_j is the prior probability of character j mutating. For the purposes of building this compatibility matrix, missing data was ignored (this is, no node in the graph corresponded to a missing state). A character c' to split cells with was identified by minimizing the sum of weights emitted from the node:

$$c' \ = \ argmin_{c \in X} \sum_{j \in Out(c)} w_{c,j}$$

where $Out(c)$ denotes the set of edges with c as a source. This process was repeated until the tree was resolved completely, or a criterion was reached as in Cassiopeia-Hybrid.

Cell filtering with Lenti-Cre-BC

After performing tree reconstruction for each clonal population, leaves were annotated with Lenti-Cre-BC information and evaluated manually for filtering. Specifically, in tumors with adequate Lenti-Cre-BC information, we identified subclades (defined here as clades that joined directly to the root) that clearly had divergent Lenti-Cre-BC information. This combined Lenti-Cre-BC and lineage analysis helped minimize the influence of lenti-Cre-BC dropout in single-cell experiments. These subclades were subsequently removed and cells were filtered out from the phylogenetic analysis. In one case (3513_NT_T4 and 3513_NT_T5), two tumor populations were split from a parental tumor (3513_NT_N2), reconstructed, and used in downstream analyses.

CNV analysis

Chromosomal copy number variations (CNV) were inferred with the InferCNV R package (version 1.2.1), which predicts CNVs based on single-cell gene expression data. InferCNV was run in 'subclusters' analysis mode using 'random_trees' as the subclustering method. Genes with less than one cell were filtered with the 'min_cells_per_gene' option, and no clipping was performed on centered values ('max_centered_threshold' set to 'NA'). The cutoff for the minimum average read count per gene among reference cells was set to 0.1, per software recommendation for 10x data. CNV prediction was performed with the 'i6' Hidden Markov Model, whose output CNV states were filtered with the included Bayesian mixture model with a threshold of 0.2 to find the most confident CNVs. All other options were set to their default values.

Each tumor sample was processed independently with normal lung cells (identified solely from the MULTI-seq deconvolution pipeline) as the reference cells. The number of CNVs for each cell was computed by counting the number of CNV regions predicted. We filtered cells with CNV counts greater than three standard deviations away from the mean of each tumor, in addition to cells with greater than or equal to 20 predicted CNVs. When comparing CNV counts of cells in expansions against those of cells in non-expansions, statistical significance was computed with a one-sided permutation test and the Mann-Whitney U-test, both of which yielded the same results.

We applied hierarchical clustering with a euclidean distance metric and the "ward" linkage to identify CNV clusters of cells within each tumor. For each clustering induced by cutting the hierarchical clustering dendrogram at different heights, we computed the probability that a cell and its nearest neighbor on the Cassiopeia tree were in the same hierarchical cluster ("nearest neighbor probability"). These clusters ranged from most coarse-grained (low cutoff height) to the most fine-grained (high cutoff height). When there were multiple nearest neighbors, pseudocounts were used by taking the fraction of nearest neighbors that were in the same cluster. We performed nonparametric Permutation Tests for each unique clustering by shuffling the cluster assignments of the cells and computing the nearest neighbor probability using these assignments.

Tree Quality Control for Fitness Inference

Trees were subjected to quality control before identifying subclones under positive selection and single-cell fitness inference. We employed two quality control metrics: first, a measure of subclonal diversity known as "percent unique indel states", defined as the proportion of cells that reported a unique set of character states (i.e., mutations). Second, we also filter lineage trees based on the level of "unexhausted target sites" defined as the proportion of characters (i.e., specific cut sites) that were not dominated

by a single mutation (i.e, more than 98% of cells contained the same mutation). These metrics describe the diversity and depth of the lineage trees, and enable filtering out tumors with poor lineage tracing quality (i.e., lineage tracing capacity became saturated too early during tumor development). Using these two metrics, we filtered out tumors that had less than 10% unique indel states or less than 20% unexhausted target sites. Additionally, tumors with too few cells recovered (fewer than 100 cells) were ignored for this analysis because of a lack of power to confidently quantify subclonal behavior.

Identifying subclonal selection (i.e., expansions)

Subclones undergoing positive selection were identified by comparing the number of cells contained in the subclone to its direct "sisters" (i.e. branches emanating directly from the parent of a subclone of interest) and computing a probability of this observation with a coalescent model. Specifically, consider a node v in a particular tree with k children stored in the set C. Let n_c denote the number of leaves below a particular node c (and observe that N = nv=c Cnc). Under the coalescent model, we can compute a probability indicating how likely a subclone c under v would have exactly n_c leaves given v had N total leaves as follows:

$$p_{N,k}(n_c) = \frac{\binom{N - n_c - 1}{k - 2}}{\binom{N - 1}{k - 1}}$$

Finally, we computed the probability that a subclone c under v would have *at least* n_c leaves given v had N total leaves is:

$$\widehat{p}_{N,k}(n_c) = \sum_{n = n_c}^{N - k + 1} p_{N,k}(n)$$

Nodes with probabilities $\widehat{p}_{N,k}(n_c) < 0.01$, at least a depth of 1 from the root, and containing subclades with at least 15% of the total tree population were annotated as undergoing an "expansion". In the analysis presented in this study, we additionally filtered out nodes annotated as "expanding" if they contained another node in their subtree that was also expanding. Expansion proportions were calculated as the fraction of the tree consisting of cells residing in any subclade called as "expanding".

Inferring single-cell fitness

To compute single-cell fitness, we used the "infer_fitness" function from the *jungle* package (publicly available at https://github.com/felixhorns/jungle) which implements a previously described probabilistic method for inferring relative fitness coefficients between samples in a clonal population (Neher et al. 2014). Because some trees contained exhausted lineages (i.e., those in which all target sites were saturated with edits), after filtering out trees that did not pass quality control (see section "Tree quality control for fitness inference" above), we pre-processed branch lengths on each phylogeny such that branches had a length of 0 if no mutations separated nodes and 1 if not. In essence, this collapses uninformative edges in the fitness inference and helps control for lineage exhaustion. After this procedure, we were left with fitness estimates for each leaf in a phylogeny, normalized to other cells within the phylogeny.

Tumor fitness differential expression

Genes differentially expressed along the fitness continuum within each tumor were identified with a linear regression approach. Specifically, given a cell i, we can model the expression of some gene j according to the cell's fitness score f_i as follows:

$$\log(1 + e_{i,j}) \sim f_i + size\_factor_i$$

Where e_{ij} is the count-normalized expression of gene j in cell i (we used the median number of UMI counts across the dataset to normalize expression level) and $size\_factor_i$ is the number of genes detected in the cell. Only genes appearing in more than 10 cells were retained for differential expression analysis. Linear models were fit using Julia's GLM package (v1.3.7). Significances were computed using a Likelihood Ratio Test, comparing the model above to a model only using the $size\_factor$ as a predictor. P-values were FDR corrected using the Benjamini-Hochberg procedure (Benjamini and Hochberg 1995). Log$_2$ fold-changes were computed by comparing the average expression of a gene in the top vs bottom 10th percentile of fitness scores.

Meta-analysis and derivation of the FitnessSignature

The transcriptional FitnessSignature was derived from the results of individual tumor fitness differential expressions with a majority-vote meta-analysis. This approach ranks genes based on the number of times that a gene is differentially expressed (FDR < 0.05 and | log$_2$FC| > log$_2$(1.5)) and the consistency of its direction. We used the MetaVolanoR R package (version 1.0.1) to perform this majority-vote analysis, which computed both of these values. We identified consistently differentially expressed genes for our transcriptional FitnessSignature if a gene appeared to show up at least 2 times in the same direction, and if the ratio between frequency and consistency was greater than 0.5.

Fitness module identification

We determined transcriptional fitness gene modules using the *Hotspot* package (version 0.9.0; (DeTomaso and Yosef 2021)). To do so, we first subset our processed single-cell expression matrix (see section below "Single-cell transcriptome analysis for KP-Tracer data") to contain only the 1,183 genes in the FitnessSignature that were positively associated with fitness. Then, using *Hotspot* we identified fitness-related genes that were significantly autocorrelated with the scVI latent space using the "danb" observation model

and 211 neighbors (the square-root of the number of cells in the expression matrix). After this procedure, genes with an FDR of less than 0.05 were retained for downstream clustering. We then computed pairwise local autocorrelations with *Hotspot* and clustered genes using these pairwise statistics with the "create_modules" function in *Hotspot* (minimum gene threshold of 100, FDR threshold of 0.05, core_only=False). This procedure identified three modules that were used for downstream analysis.

Single-cell transcriptome processing for KP-Tracer NT data

The scRNA-seq was processed using the 10X CellRanger pipeline (version 2.1.1) with the mm10 genome build. Cells were assigned to a sample using the MULTI-seq pipeline described above (see section "Single-cell preprocessing pipeline"). After quantification, informative genes were identified using the Fano filtering process implemented in *VISION* (DeTomaso et al. 2019), and raw counts were batch-corrected (using the batch-harvest data, indicating when a batch of mice were sacrificed as the batch variable) and projected into a shared latent space of 10 dimensions with scVI (Gayoso et al., 2022; Lopez et al., 2018). Cells were initially clustered with the Leiden algorithm as implemented in Scanpy (Wolf et al. 2018; Traag et al. 2019), and two clusters dominated by cells annotated as normal and cells that could not be confidently mapped to a tumor via MULTI-seq or Lenti-Cre-BC analysis (see section "Single-cell preprocessing pipeline" and "Cell Filtering with Lenti-Cre-BC" above) were removed from downstream analysis. Clusters were then manually re-clustered to obtain segmentations that aligned with gene expression patterns. After this process, we were left with a total of high-quality 58,022 cells with single-cell transcriptomic profiles from KP mouse tumors. Single-cell counts were normalized by the median UMI count across cells and logged to obtain log-normalized data. Gene markers for each Leiden cluster were identified using the Wilcox rank-sums test on the log-normalized gene counts with the Scanpy package (Wolf et al. 2018).

Integration of normal lung epithelium transcriptomes

scRNA-seq data of cells obtained from various tissues in sample L46 were quantified using the 10X CellRanger pipeline (version 2.1.1) with the mm10 genome build. Cells were assigned to a sample (one of 4 tissues) using the CellRanger multi procedure. After quantification and sample assignment, cells with fewer than 200 UMIs and genes appearing in fewer than 1% of cells were filtered out. This left us with 14,424 high-quality cells. A low-dimensional embedding was inferred using scVI on the dataset with the 4000 most highly-variable genes (using the "seurat_v3" flavor of Scanpy's highly_variable_genes function). Transcriptional clusters were identified using the Leiden community detection algorithm. One cluster of 329 cells consisted of normal lung cells and expressed gene markers *Nkx2-1*, *Sftpc*, and *Scgb1a1*; we isolated and annotated this cluster as normal lung epithelial cells (primarily AT2 and club cells).

This dataset of 329 normal lung epithelial cells (isolated from the L46 sample, as described above) was integrated into the scRNA-seq dataset of KP tumors (see section "Single-cell transcriptome processing for KP-Tracer NT data") using scVI (Gayoso et al., 2022; Lopez et al., 2018). Specifically, we used scVI to batch-correct these two datasets and project all cells into a common coordinate system. Then, we visualized this scVI batch-corrected embedding with UMAP.

Differential expression analysis of Chuang et al

TPM-normalized RNA-seq data were downloaded from GEO accession GSE84447. Samples were split into early and late-stage tumor groups based on the author annotations: tumors annotated with "KPT-E" were assigned to the early stage group and tumors with "TnonMet" or "TMet" annotations were assigned to the late group. Then, we log-normalized the TPM counts and used the limma R package (version 3.36.3) to infer differentially expressed genes with the "eBayes" function. Genes passing an FDR threshold of 0.05 and $\log_2$-fold-change threshold of 1 (in either direction) were called differentially expressed and used for comparison with the FitnessSignature described in this study.

FitnessSignature analysis of Marjanovic et al

Raw expression count matrices were downloaded directly from GEO, accession number GSE152607. Gene counts were normalized to transcript length, to account for read depth artifacts in the Smart-Seq2 protocol. *VISION* (DeTomaso et al. 2019) was used to compute FitnessSignature scores (using the FitnessSignature gene set described in our study) for each cell in the dataset and scores were averaged within time points of KP mice.

Survival analysis with TCGA lung adenocarcinoma tumors

The fitness signature genes including 1183 up-regulated genes and 1027 down-regulated genes from mice experiments were converted to corresponding genes from the *H. sapiens* genome (build hg19), resulting in 1126 up- and 970 down-regulated human genes, respectively. FitnessSignature with only up-related genes was denoted as FSU, FitnessSignature with only down-related genes was denoted as FSD. TCGA Lung adenocarcinoma cohort with RNAseq data (n=495) were stratified into FSU-High, FSU-Low, FSD-High, and FSD-Low according to median expression of sum of FitnessSignature genes, then, patients harboring genes with FSU-High and FSD-Low formed a group, patients containing FSU-Low and FSD-High gene expression formed another group. Subsequently, these two groups were used for survival analysis using the survival package in R (version 3.2.11). The survival analysis was invoked with the call "survfit(Surv(Time, Event) ∼ Group)" where "Group" is the FitnessSignature-based stratification. Kaplan–Meier curve is shown with a log-rank statistical test. For fitness gene module 1, 2, and 3 analyses, patients were divided into module gene expression of High and Low based on the median of the sum of gene expression, followed by survival analysis.

Fitness Module Enrichment

Each of the three fitness gene module scores (computed with *VISION*) were normalized to the range [0, 1] across all NT cells. All NT cells in non-expansions were defined as the background cells, and the background module scores were calculated by averaging the

normalized module scores of these cells. Additionally, the module scores of cells in each expansion were averaged to obtain the psuedo-bulk module score for each expansion. These module scores were divided by the background module scores, yielding the module enrichment score (i.e. fold-change versus background) per fitness module. These scores were plotted on a personality plot for visualization. Every expansion was assigned (non-exclusively) to the three fitness modules using a permutation test to test whether the cells in the expansion exhibited a significant increase in fitness module score compared to non-expanding background cells ($p < 0.05$).

Calculation of single-cell and Leiden cluster EffectivePlasticity

EffectivePlasticity for each tumor was computed by first calculating a normalized parsimony score for the tumor tree, with respect to the Leiden cluster identities at the leaves, using the Fitch-Hartigan algorithm (Fitch 1971; Hartigan 1973). Briefly, this procedure begins by assigning cluster identities to the leaves of the tree, and then calculates the minimum number of times a transition between cluster identities must have happened ancestrally in order to account for the pattern observed at the leaves. To compare scores across trees, we normalize these parsimony scores by the number of edges in the tree, thus giving the EffectivePlasticity score. In all analyses, we filtered out cells that were part of Leiden clusters that were represented in less than 2.5% of the total size of the tree.

In order to generate single-cell EffectivePlasticity ("scEffectivePlasticity"), we computed the EffectivePlasticity for each subtree rooted at a node on the path from the root to a leaf and averaged these scores together. This score thus represents the average EffectivePlasticity of every subtree that contains a single cell.

To generate average EffectivePlasticity for each Leiden cluster, we first stratified cells in each tumor according to the Leiden cluster. Then, we averaged together scores within each tumor for each Leiden cluster, thus providing a distribution of EffectivePlasticity for each Leiden cluster.

Calculation of the Allelic EffectivePlasticity score

The Allelic EffectivePlasticity score provided a "tree-agnostic" measurement of a cell's effective plasticity. Qualitatively, the score measures the proportion of cells that are found in a different Leiden cluster than their closest relative (as determined by the modified edit distance between two cells' character states; see section "Allelic Coupling" for the definition of this distance metric). Importantly, if a cell has more than one closest relative, each of their votes are normalized by the number of equally close relatives this cell has. More formally, the single-cell Allelic EffectivePlasticity was defined as:

$$a(i) = \frac{1}{|K|} \sum_{k \in K} I(leiden(k) == leiden(i))$$

Where K indicates the set of a cell's closest relatives, as measured by modified edit distance, $leiden(i)$ indicates the Leiden cluster that cell i resides in, and $I()$ is an indicator function that is 1 if the two Leiden clusters are the same and 0 otherwise. The Allelic EffectivePlasticity of a tumor is the average of these scores:

$$A(tumor) = \frac{1}{|L|} \sum_{l \in L} a(l)$$

Calculation of the L2 EffectivePlasticity score

The L2 EffectivePlasticity score served as an alternative tree-based score that accounted for random noise at the boundary between two Leiden clusters, as opposed to treating each Leiden Cluster as a point. As with the EffectivePlasticity score, we first found nearest-neighbors of each cell i using the phylogenies and considered neighbors found in a different Leiden cluster than i. Yet, in contrast to the EffectivePlasticity score, we distinctly used an L2-distance in the 10 dimensional scVI latent space to obtain a measure of how distinct the neighbor was. Mathematically, the single-cell L2 EffectivePlasticity score was defined as:

$$l_2(i) = \frac{1}{|K|} \sum_{k \in K} ||x_i - x_k||_2$$

Where K indicates the set of a cell's closest relatives, as found with the phylogeny, and x_i indicates the 10-dimensional embedding of cell i's single-cell expression profile in scVI space. The L2 EffectivePlasticity of a tumor was defined as the average across all leaves in the tumor.

Evolutionary Coupling

Evolutionary Coupling is the normalized phylogenetic distance between any pair of variables on a tree. Mathematically, given two states M and K that can be used to label a subset of the leaves of the tree, we compute the average distance between these states:

$$D(M,K) = \frac{1}{n_m n_k} \sum_{m \in \{M\}, k \in (K)} d_T(m,k)$$

where n_M is the number of leaves with state M, $\{M\}$ denotes the set of cells in set M, and $d_T(i, j)$ denotes the phylogenetic distance between leaves. There are multiple ways to score $d_T(i, j)$, and here we used the number of mutated edges for our analysis (i.e., the number of edges separating two leaves i and j that carried at least one mutation). To normalize these distances, we compare $D(M, K)$ to a random background generated by shuffling the leaf assignments 2000 times. Then, to obtain background-normalized scores, we Z-normalize to the random distribution D_R:

$$D'(M,K) = \frac{D(M,K) - E[D_R(M,K)]}{SD[D_R(M,K)]}$$

This score is obtained for all pairs of states in a tumor that pass a 2.5% proportion threshold (i.e., we filter out cells in states that fall below this threshold). Then, from the matrix of all background-normalized phylogenetic distances, P (such that $P_{M,K}$ is equal to $D'(M,K)$), we compute the Evolutionary Couplings between two states M and K by Z-normalizing P:

$$E(M,K) = \frac{P_{M,K} - E[P]}{SD[P]}$$

Evolutionary Couplings presented in Figures 5B and 5D are normalized as:

$$\hat{E}(M,K) = \exp\left(-\frac{E(M,K)}{\max(abs(E))}\right)$$

Where E denotes all the Evolutionary Couplings between states in a given tumor.

Allelic Coupling
We used modified edit distances between cells to compute an Allelic Coupling score that could be used to assess consistency of the Evolutionary Coupling results. Here, we used a modified edit distance, $h'(a_i, b_i)$, that scored the distance between sample a and b at the ith character:

$$h'(a_i, b_i) = \begin{cases} 2 & \text{if } a_i \neq b_i \text{ and } a_i \neq 0 \text{ and } b_i \neq 0 \\ 1 & \text{if } (a_i == 0 \text{ or } b_i == 0) \text{ and } a_i \neq b_i \\ 0 & \text{o.w.} \end{cases}$$

The allelic distance between two samples a and b is $\sum_{i \in X} h'(a_i, b_i)$. We used these distances instead of phylogenetic distances to compute the coupling statistic described in the section above entitled "Evolutionary Coupling" and called this new coupling statistic "Allelic Coupling".

K-nearest-neighbor (KNN) Coupling
K-nearest-neighbor (KNN) coupling was computed by using d_T as the distance to the kth neighbor in the Evolutionary Coupling statistic. We used the same phylogenetic distance described in the section entitled "Evolutionary Coupling" to compute the kth neighbor and used $k=10$ for the analysis.

Fate clustering
To identify separate fates in the KP-Tracer dataset, we first computed Evolutionary Couplings in each tumor for all pairs of states. To remove noise intrinsic to the clustering, we filtered out clusters that accounted for less than 2.5% of the tumor. As a phylogenetic distance metric, we used the number of mutated edges (i.e., any edge that contained at least one mutation was given a weight of 1 and otherwise the edge was weighted as 0). Before computing Evolutionary Couplings, we preprocessed the lineages such that each leaves with the same Leiden cluster were grouped together (see section entitled "Preprocessing lineages with respect to states").

After calculating the Evolutionary Coupling for all pairs of states within each tumor, we concatenated all vectors of Evolutionary Coupling together into a matrix. We additionally converted Evolutionary Couplings to similarities by exponentiating these values (i.e, $E'(M, K) = exp(-E(M,K))$). As additional features for this clustering, we also added Leiden cluster proportions to each tumor's vector of couplings. Then we Z-normalized across features to compare tumors and clustered this transformed matrix using a hierarchical clustering approach in the python scipy package (version 1.6.1). We used a Euclidean metric and the "ward" linkage method. We identified three clusters from this hierarchical clustering, corresponding to our three Fate Clusters. These three Fate Clusters were visualized using Uniform Manifold Approximation and Projection (UMAP) on the Evolutionary Coupling and Leiden cluster proportion concatenated matrix. Important couplings were identified using Principal Component Analysis on the same Evolutionary Coupling concatenated matrix.

Preprocessing lineages with respect to states
In some lineages, we observed that polytomies (or non-bifurcating) subclades were created at the very bottom of the tree due to the saturation of target site edits. Because this could artificially appear to make cellular states more closely related than they actually were, we took a conservative approach to making conclusions about cellular relationships between leaves in such polytomies. Specifically, we first assigned states from a state space Σ to each leaf in a tree according to some function $s(l) \rightarrow \sigma \in \Sigma$ for all l leaves in the tree. Then, for all polytomies that contained at least unique states or more, we created extra splits in the tree for each unique state. More formally:

```
PREPROCESS-LINEAGE (Tree):

        for v in Tree:

    states =

    If len(children(v)) < 3:

        continue

        for c in children(v):

        if is_leaf(c):

        states.append(s(c))

 If len(unique(states)) > 2:

 for state in unique(states):

                Tree.add_edge(v, 'new-node-{state}')

            for c in children(v):

     If s(c) == state:

                    Tree.add_edge('new-node-{state}', c)


                Tree.remove_edge(v, c)

 return Tree
```

Aggregating evolutionary coupling across fate cluster

To create a consensus Evolutionary Coupling map across the tumors in a Fate Cluster, we first computed the average Evolutionary Coupling between all pairs of states in a tumor as described previously. Then, we computed an average Evolutionary Coupling for each pair of states, normalizing by the number of tumors that this pair appeared in above the requisite 2.5% threshold. Critically, we removed patterns that were driven by a small proportion of cells, we only considered states that appeared in at least 2.5% of the total number of cells across all tumors in a Fate Cluster.

Phylotime

Phylotime was defined as the distance to the first ancestor that could have been a particular state. To approximate the Phylotime in this study, we defined the initial AT2-like state (Leiden cluster 4) as the ground state, and inferred the sets of states for each ancestor with the Fitch-Hartigan bottom-up algorithm (Fitch 1971; Hartigan 1973). Then, in each tumor, we computed the phylogenetic distance separating each cell from its closest ancestor that could have been an AT2-like cell, as determined with the Fitch-Hartigan bottom-up algorithm. Phylogenetic distances were defined as the number of non-zero-length branches (though we compare the consistency of Phylotime to a distance metric that uses the number of mutations along each edge in Figures S5J and S5K). In this way, Phylotime is proportional to the number of generations elapsed since the more recent ancestral node that, under a maximum-parsimony approach, could have been an AT2-like cell. Here, the tree structure is advantageous in modeling divergence times from the AT2-like state because it can account for homoplasy (i.e., the same mutation occurring independently) and convergent phenotypic evolution events (i.e., the same transcriptomic state being reached separately, as opposed to pseudotime statistics estimated from single-cell transcriptomes (Trapnell et al., 2014) events. Thus, it is preferable, in principle, to comparing the mutation states directly between a leaf and all AT2-like cells. Phylotime within each tumor was normalized to a 0-1 scale. Once every tumor was analyzed this way, Phylotime across tumors was merged by performing an average-based smoothing across the transcriptional space: specifically, for each cell, we found the 5 closest neighbors in transcriptional space (in the low-dimensional scVI latent space) and averaged Phylotimes within this neighborhood. After integrating together Phylotime in this manner, the final distribution across tumors was normalized once again to a 0-1 scale.

Phylotime differential expression

Genes associated with Phylotime in each Fate Cluster were identified using the *Tradeseq* package (Van den Berge et al. 2020). Specifically, for each Fate Cluster, lowly-expressed genes were filtered if they were detected in fewer than 10% of cells and high-variance genes were identified with the Fano filtering procedure implemented in *VISION* (DeTomaso et al. 2019). Then, in each cluster, expression models were fitted with the "fitGAM" function and genes associated with a specific segment of Phylotime were identified with the "associationTest" function. P-values were FDR corrected using the Benjamini-Hochberg procedure (Benjamini and Hochberg 1995), and significant genes were retained if they had an FDR below 0.05 and a mean $\log_2$-fold-change above 0.5. Smoothed

expression profiles were predicted with the *Tradeseq* package using the models fit from the fitGAM procedure and genes were subsequently clustered into those expressed early and late. Gene set enrichment analysis was performed using the enrichR R package (version 3.0) after converting gene names from mm10 to GRCh38. We used the Biological Process gene ontology, ChEA, and MsigDB Hallmark gene sets. Informative genes were manually selected from the set of genes passing the significance and effect-size thresholds, and manually clustered for display in Figure 5.

Integrating transcriptomes of KP-Lkb1 and KP-Apc data

The scRNA-seq data was processed using the 10X CellRanger pipeline (version 2.1.1) with the mm10 genome build. Cells were assigned to a sample using the MULTI-seq pipeline as described above (see section "Single-cell preprocessing pipeline") to form a raw count matrix consisting of cells from KP, KPL, or KPA mice. Cells with fewer than 200 genes detected, greater than 15% of mitochondrial reads, or greater than 7000 genes detected were filtered out. Cells were batch-corrected and projected into 20 latent dimensions using scVI (Gayoso et al., 2022; Lopez et al., 2018) with 2 hidden layers and the library batch as a batch covariate on the top 4000 most variable genes, as detected with Scanpy's "highly_variable_genes" function with the "seruat_v3" flavor (Wolf, Angerer, and Theis 2018). Clusters were identified with the Leiden algorithm (Traag, Waltman, and van Eck 2019) with manual parameter selection to obtain an acceptable resolution. All normal cells and seven additional clusters with high proportions of normally-annotated cells (as with MULTI-seq or via the lineage-tracing data) were filtered out for downstream analysis (a total of 2,209 cells in the entire dataset).

To perform label transfer from the KP-Tracer dataset, we first labeled all KP cells in the integrated dataset with previous annotations and labeled all new cells with "Unknown". Then, we used scANVI (Xu et al. 2021) to predict labels of cells from KPL and KPA mice using 40 latent dimensions, 2 hidden layers, and a dropout rate of 0.2. Upon inspecting predictions, we elected to keep predictions made by scANVI for the majority of cells, with the exception of 5 new Leiden clusters identified by clustering the scVI latent space. Additionally, we elected to merge one new Leiden cluster with the Pre-EMT state because key gene expression markers across these two states were consistent. After this process, we were left with a total of 104,197 high-quality cell transcriptomes.

Differential expression analysis of Pre-EMT state

The single-cell RNA count matrix was first count-normalized to the median number of UMI counts across cells and log-transformed. Then, cells assigned to the Pre-EMT state were separated into three non-overlapping sets according to their genotype (KP, KPL, or KPA). Differentially expressed genes in the KPL subset of cells in the Pre-EMT cluster were identified by comparing these cells to all other cells with Scanpy using a t-test on log-normalized count matrix with the top 5000 most variable genes. Highlighted genes were selected from the set genes passing an FDR cutoff of 0.05 and a $\log_2$FC cutoff of 1.

Evolutionary Trajectory Analysis of KPL and KPA Tumors

The evolutionary trajectories from KPL and KPA mice were analyzed identically to the KP tumors as described in the previous section entitled "Fate Clustering". Briefly, each tumor was described as a vector of Leiden cluster proportions and exponentiated Evolutionary Couplings (i.e, $E'(M, K) = exp(-E(M,K))$). Vectors were concatenated together and Z-normalized across features. The resulting matrix was decomposed and analyzed using Principal Component Analysis (PCA) and informative features were identified by evaluating the features with highest principal component loadings.

Evolutionary Coupling of 3724_NT_T1 Tumor-Metastasis Family

Using the tumor-metastasis family tree for 3724_NT_T1 and associated metastases, we computed the Evolutionary Couplings between each microdissected piece of the primary tumor (T1-15) and each metastasis (the statistic is described in the section entitled "Evolutionary Coupling"). Normalized Evolutionary Couplings (E) were computed as described previously.

Phylogenetic distances on Tumor-Metastasis Family trees

In each of the tumor-metastasis families (defined as a tumor containing both a primary tumor and a large enough metastatic population) analyzed in Figures 7 and S7, we first reconstructed trees encompassing all cells in the primary and metastatic tumors (referred to as a "tumor-metastasis family" tree). Then, we stratified cells in the primary tumor by the expansions called with our expansion-calling statistic (see above, "Identifying subclonal selection"). If a cell was not part of an expansion, it was labeled as "non-expansion". Then, for each cell in a metastatic tumor, we computed the average modified phylogenetic distance to all primary tumor cells in the tumor-metastasis family tree. The modified phylogenetic distance was computed as the sum of branch lengths, where each branch length was defined as the number of mutations separating each node from one another (as inferred using Camin-Sokal parsimony - i.e., irreversibility of mutations).

Transcriptional distances on Tumor-Metastasis Family trees

Tumor-metastasis family trees were inferred and stratified as described above (see "Phylogenetic distances on Tumor-Metastasis Family trees") and Euclidean distance was used to measure transcriptomic differences between metastatic cells and primary tumor subpopulations.

Distribution comparisons and statistical significance

All statistical tests comparing the distribution of continuous values are indicated in the appropriate figure legend. Mann-Whitney U tests were performed using the *ranksums* function in the scipy.stats python package with sidedness specified in the figure legend. All boxplots present the quartiles of the distribution and whiskers show the rest of the distribution. Outliers of boxplots are determined using as being 1.5x the inter-quantile range.
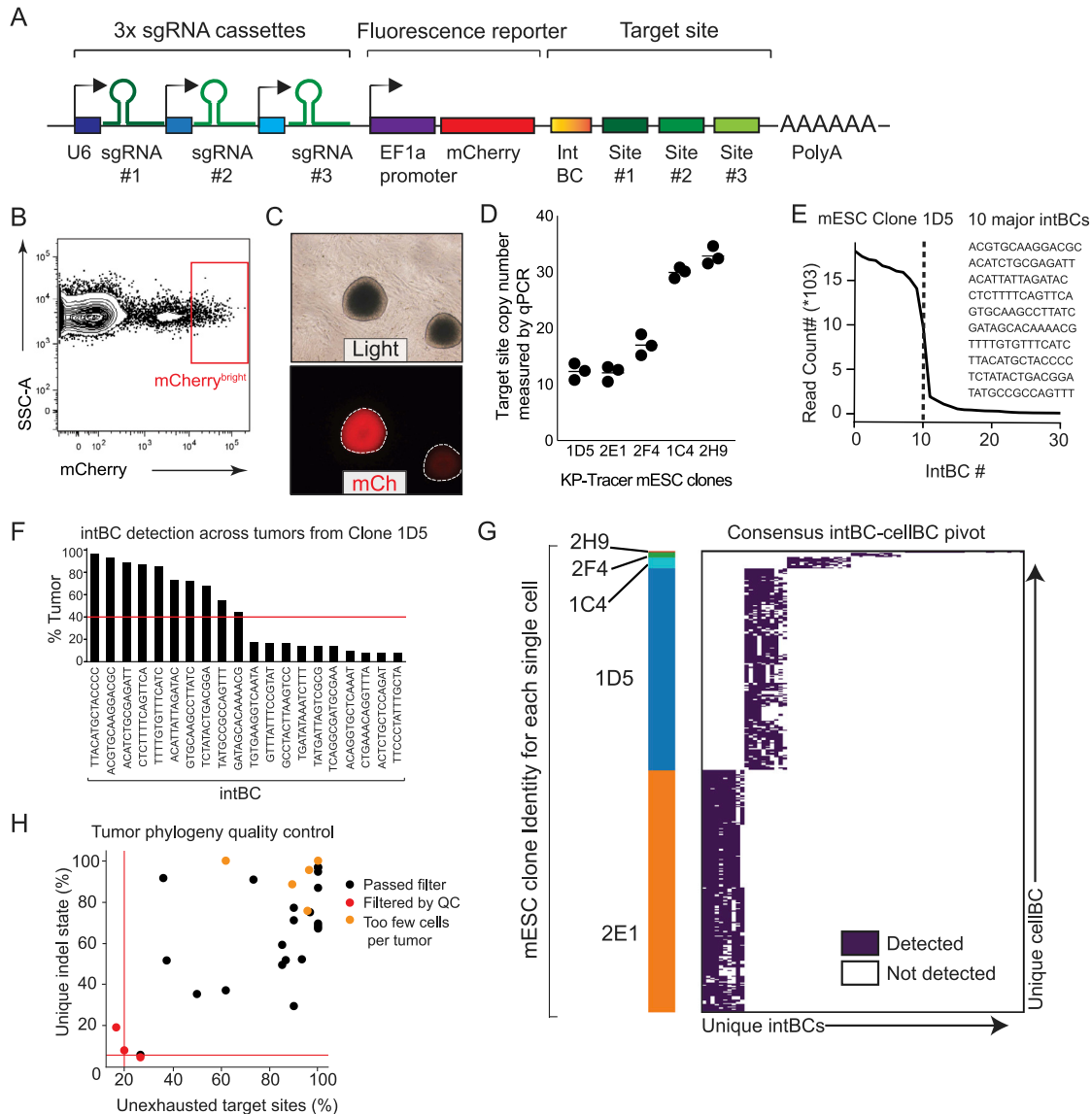
Supplemental figures

Figure S1. KP-Tracer mouse genetic components, validation, and quality control, related to Figure 1

(A) The piggyBac transposon-based lineage-tracing vector libraries used to engineer the KP-Tracer mice contained (1) a triple-guideRNA cassette and (2) a target site library cassette with a 14-bp integration bar code ("intBC") and three CRISPR/Cas9 cut sites on the 3′ UTR of an mCherry reporter gene.

(B) Enrichment of mESC population with high lineage-tracer expression based on high mCherry expression (a reporter indicating lineage-tracer expression). These cells are then single-cell cloned before generating chimeric KP-Tracer mice.

(C) Representative images of specific mCherry positive mESC clones that express the lineage-tracing vectors.

(D) Copy number of lineage-tracing vectors across 5 mouse embryonic stem cell (mESC) clones used in this study measured by genomic qPCR are shown.

(E and F) Detection of unique lineage-tracing target site intBCs for a representative mESC clone (1D5) using (E) DNA sequencing and (F) scRNA-seq. A consensus set of target sites intBCs for each mESC clone was determined by selecting intBCs detected in at least 40% of all tumors derived from that mESC clone.

(G) The consensus intBC pivot table across all five mESC clones used in this study to generate KP-Tracer mice. Each row is a single cell and is annotated with which mESC clone it came from. Each column is a unique intBC. Colors in the heatmap indicate whether or not an intBC was detected in a given cell.

(H) Quality-control filtering of tumor phylogenies for subclonal expansion analyses. Quality of lineage-tracing data was assessed with two metrics: first, the percentage of cells that contained a unique set of mutations ("% unique indel state"; STAR Methods) and second, the percentage of target sites that had to be filtered because of low diversity ("target site saturation"; STAR Methods). Tumors with less than 5% overall unique indel state, greater than 80% target site saturation, or fewer than 100 cells were filtered out.
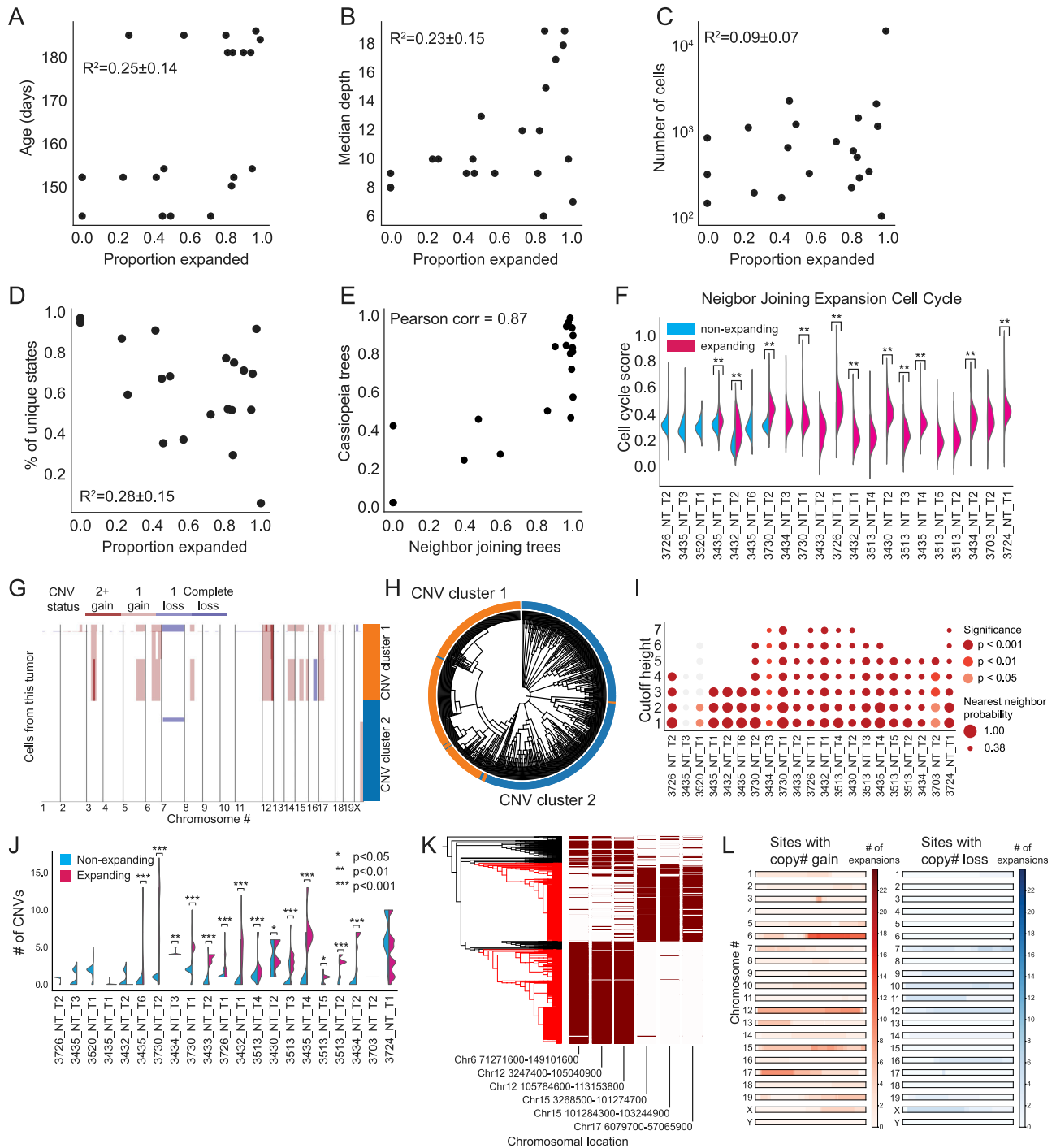
Figure S2. Characterization of tumor subclonal expansions, related to Figure 2

(A–D) phylogenetic features of tumor lineages and their predictiveness (as measured with R^2) on the expansion proportion of a tumor. Features evaluated were (A) age, (B) median tree depth, (C) size measured in the number of cells, and (D) proportion of unique cells.

(E) Expansion proportion of tumors measured from Neighbor-Joining trees versus Cassiopeia trees. The percentage of cells in expansions were highly consistent between these two tree reconstruction strategies (Pearson's correlation = 0.87).

(F) Comparison of cell-cycle scores inferred from transcriptomic profiles in expanding versus nonexpanding tumor subclones, identified from Neighbor-Joining trees (** $p < 0.01$).

(G and H) Representative example of comparison between hierarchical clustering of CNVs and Cassiopeia-reconstructed phylogeny.

(G) The inferred CNVs are shown for the representative tumor, with the largest two clusters, identified via hierarchical clustering, indicated by the color bar.

(legend continued on next page)

(H) These two clusters are also indicated with unique colors on the Cassiopeia-reconstructed tumor phylogeny. The good correlation between CNV status and tumor phylogeny indicates the accuracy of tree reconstruction.

(I) Heatmap displaying the probabilities that a cell and its nearest neighbor on the Cassiopeia-reconstructed phylogeny are in the same CNV cluster (size of circles). These probabilities were calculated for each tumor at various depths of the CNV hierarchical clustering dendrogram. The depth that yielded the most coarse-grained clusters was set to have a cutoff height of 1, with higher cutoff heights indicating finer clusters. The majority of Cassiopeia-reconstructed phylogenies were significantly consistent with CNV clusters (color of circles; permutation test) at all clustering resolutions.

(J) A comparison of CNV counts in expanding versus nonexpanding portions of tumors (* $p < 0.05$, ** $p < 0.01$, *** $p < 0.001$).

(K) An example of distinct CNV regions of cells from a single tumor. This tumor underwent two independent clonal expansions (red branches; left), each of which exhibited distinct CNV patterns (red bars; right).

(L) An aggregated view of the CNV "hotspots" across subclonal expansions from all tumors. Each horizontal bar represents a chromosome, and the intensity of color indicates the number of subclonal expansions exhibiting a CNV in a region (STAR Methods). Regions that more often exhibited copy number gains are indicated in red (left); genomic regions that more often exhibited copy number losses are indicated in blue (right).
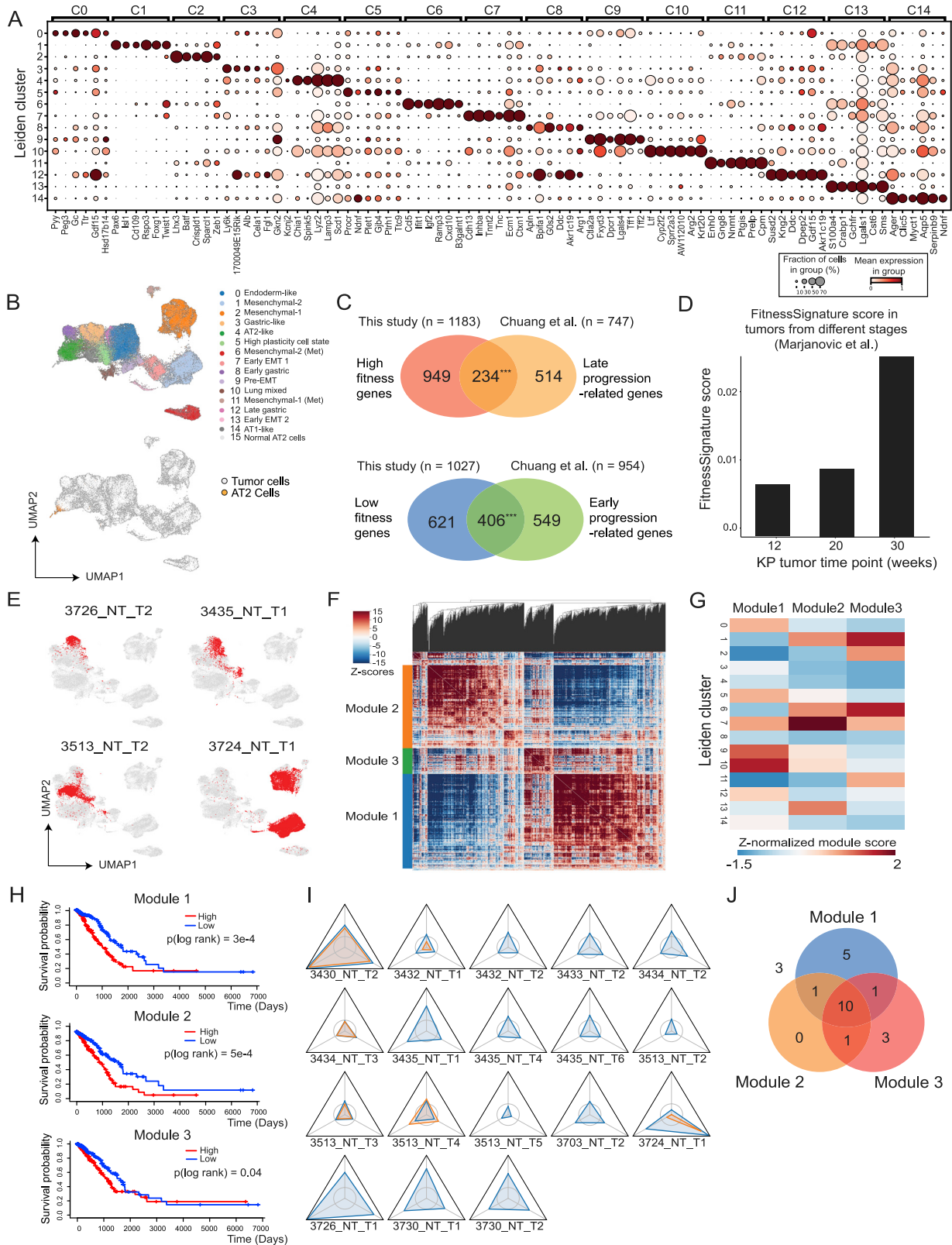
Figure S3. Characterization of transcriptomic fitness landscape, related to Figure 3

(A) Gene markers for each Leiden cluster identified in the processed scRNA-seq latent space. Dot size indicates the percent of cells expressing the marker. Color indicates mean expression level.

(B) Integration of normal lung epithelial cells with KP-Tracer dataset. Normal lung epithelial cells were isolated from an independent dataset and integrated with KP-Tracer tumors using scVI (STAR Methods). Leiden cluster annotations from analysis of KP-Tracer tumors are shown (top), and normal cells are highlighted against tumor cells (bottom).

(C) Gene set comparison between the FitnessSignature described in this study and KP tumor progression-associated genes described in (Chuang et al., 2017). Overlap significance assessed with a hypergeometric test (*** = p < 1e–5).

(D) Average transcriptional FitnessSignature score in KP tumors harvested at 12-week, 20-week, and 30-week time points from (Marjanovic et al., 2020).

(E) Representative examples of tumors occupying distinct regions of the transcriptional space. Cells from the tumor of interest are shown in red, and all other cells are shown in gray.

(F) *Hotspot* autocorrelation heatmap and clustering of genes that appear in the FitnessSignature and are positively associated with fitness. Gene modules are identified by distinct color strips on the left. Values in the heatmap are Z-normalized pairwise autocorrelation scores between genes. The dendrogram linking genes is shown for the columns.

(G) Z-normalized mean fitness gene module signature scores of each Leiden cluster.

(H) Kaplan-Meier plots for TCGA human lung adenocarcinoma patients with respect to genes in each fitness module. Curves are shown comparing overall survival of patient groups whose tumors have high (red) versus low (blue) expression of individual fitness gene modules, as determined by the median fitness module score. p values from a log-rank test are indicated.

(I) Fitness module enrichment personality plots. Each corner of the triangle represents the fold enrichment of an expansion's fitness module expression over expectation (nonexpanding background). Independent expansions in each tumor are shown in unique colors (blue or orange).

(J) Venn diagram illustrating the classification of expansions to gene modules based on a p value threshold of 0.05 using a permutation test against nonexpanding background.
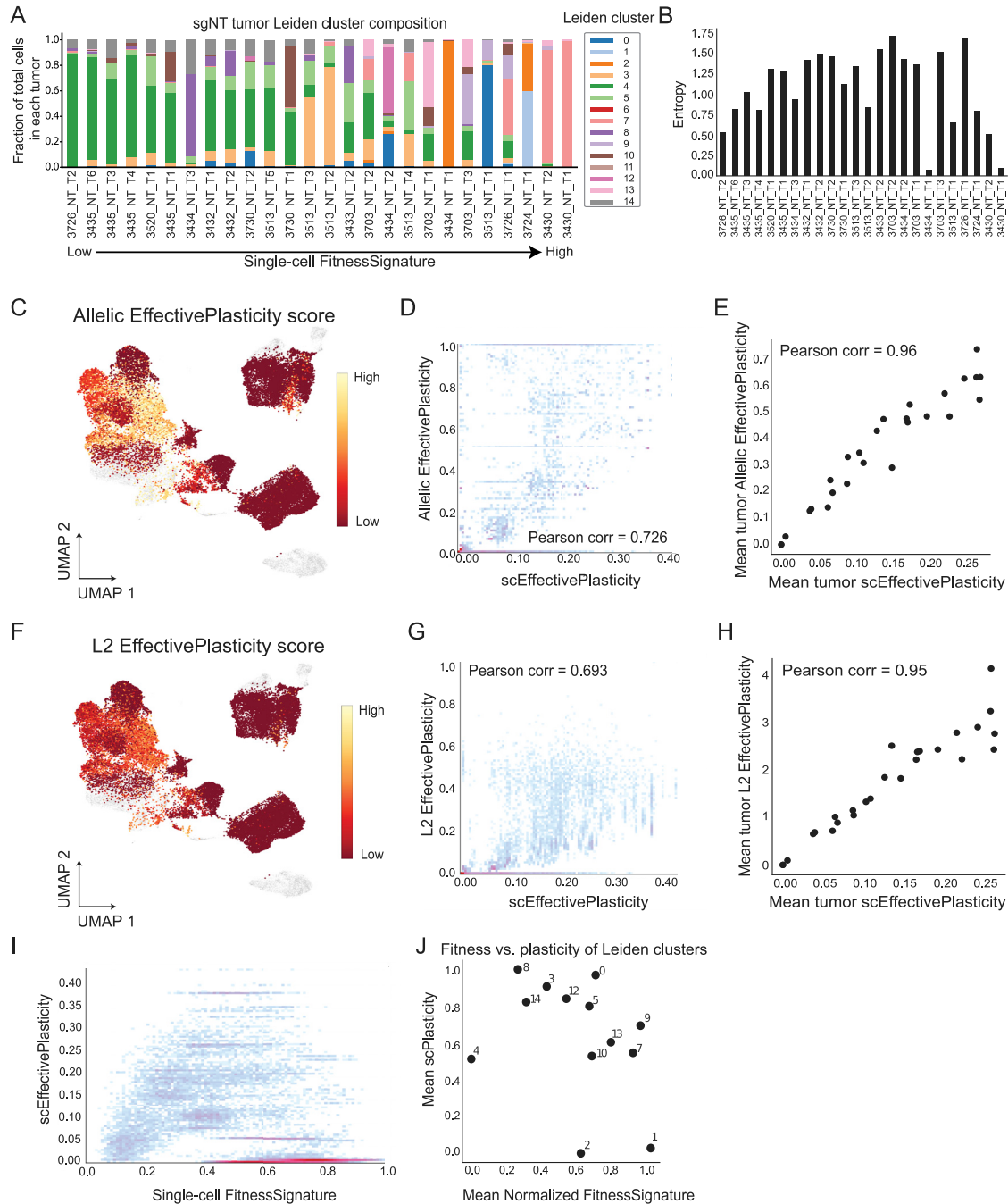
Figure S4. Validation of EffectivePlasticity score and comparison to FitnessSignature, related to Figure 4

(A) Leiden cluster proportions for each KP-Tracer tumor. The fraction of cells in each Leiden cluster is shown for each tumor in a stacked bar plot, where each Leiden cluster is indicated by the unique color introduced in Figure 3A. Tumors are ordered by mean FitnessSignature score.

(B) Shannon's Entropy statistic for each tumor, computed with the Leiden cluster proportions; tumors are ordered by mean FitnessSignature score.

(C) Allelic EffectivePlasticity score overlaid onto two-dimensional gene expression UMAP is shown. Allelic EffectivePlasticity is an alternative way to quantify EffectivePlasticity by comparing transcriptional states between cells with similar lineage-tracing indel states without using lineage trees.

(D) Comparison of Allelic EffectivePlasticity to scEffectivePlasticity (Pearson's correlation = 0.73). Each point represents a single cell.

(E) Comparison of mean tumor Allelic EffectivePlasticity to tumor EffectivePlasticity (Pearson's correlation = 0.96). Each point represents a tumor.

(F) L2 EffectivePlasticity score overlaid onto two-dimensional gene expression UMAP is shown. L2 EffectivePlasticity is another alternative way to quantify EffectivePlasticity by computing dissimilarity in gene expression profiles between nearest neighbors on the phylogeny.

(G) Comparison of single-cell L2 EffectivePlasticity to scEffectivePlasticity (Pearson's correlation = 0.69). Each point represents a single cell.

(H) Comparison of mean tumor L2 EffectivePlasticity with mean tumor EffectivePlasticity (Pearson's correlation = 0.95). Each point represents a tumor.

(legend continued on next page)

(I) Comparison of scEffectivePlasticity to single-cell FitnessSignature scores. Each point represents a single cell.

(J) Weighted mean EffectivePlasticity vs mean FitnessSignature for each transcriptional state (Leiden cluster). The weighted mean EffectivePlasticity for each Leiden cluster was determined by first computing the mean scEffectivePlasticity for each Leiden cluster in a tumor, and then averaging these values together. Each point represents a tumor.
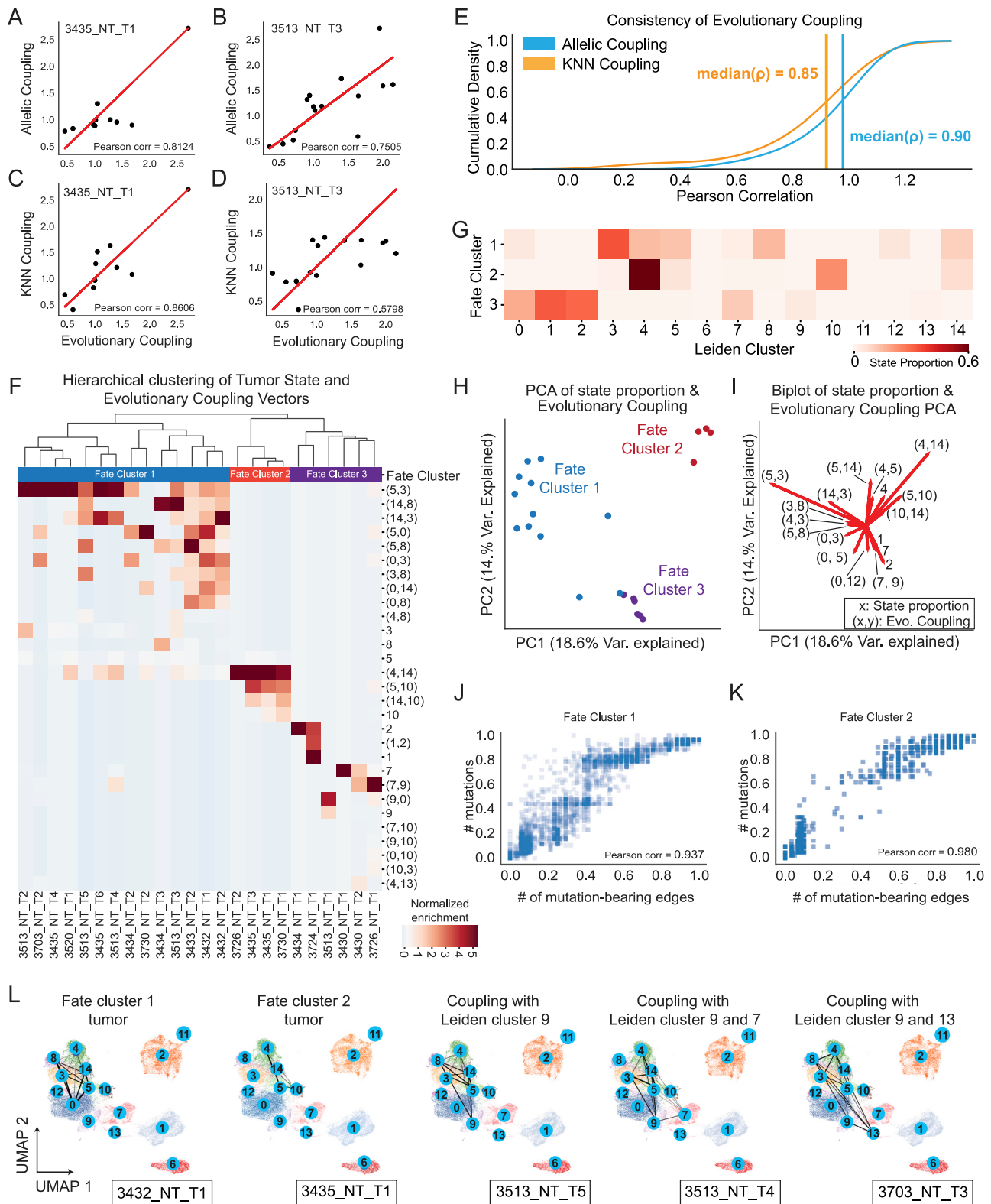
Figure S5. Validation of Evolutionary Coupling and Fate clustering, related to Figure 5

(A–D) Two alternative statistics measuring couplings between states from lineage-tracing data are used to corroborate the Evolutionary Coupling results for the representative tumors 3435_NT_T1 and 3513_NT_T3 shown in Figures 5A–5D. The comparisons between Allelic Coupling and Evolutionary Coupling for (A)

(legend continued on next page)

3435_NT_T1 and (B) 3513_NT_T3 are consistent (Pearson's correlation = 0.94 and 0.99, respectively). The comparisons between KNN Coupling and Evolutionary Coupling for (C) 3435_NT_T1 and (D) 3513_NT_T3 are consistent (Pearson's correlation = 0.97 and 0.86, respectively). Red line indicates the symmetrical $y=x$ relationship.

(E) Cumulative density function for Pearson's correlation of Allelic Coupling and KNN Coupling statistics with Evolutionary Couplings for all KP-Tracer tumors. Median correlations are indicated with vertical bars and annotated with the median correlation value.

(F) Clustering of tumors based on Evolutionary Coupling and Leiden cluster proportion statistics reveals features that distinguish different Fate Clusters. Three clusters are identified by unbiased clustering, corresponding to Fate Clusters 1, 2, and 3. Fate Cluster is annotated on top of each unique color in the first row of the heatmap. Values/colors in the heatmap are normalized across tumors, and each row corresponds to a feature (either an Evolutionary Coupling or Leiden cluster proportion). Evolutionary couplings are indicated by a tuple of the form (x, y), and Leiden cluster proportions are indicated by a single number of the form x. We focus on showing features that distinguish different clusters, and uninformative features, identified as nonsignificant by a Mann-Whitney U test ($p > 0.1$), are not shown.

(G) Heatmap of state proportions for each Fate Cluster across Leiden clusters. The value of the ith row and j^{th} column indicate the fraction of cells found in the jth Leiden cluster across all tumors in the ith Fate Cluster.

(H) Principal component analysis (PCA) of tumor Evolutionary Coupling and Leiden cluster proportion vectors. Each dot is a tumor. Tumors are colored by their Fate Cluster, as identified with the hierarchical clustering shown in Figure S5E. The percent of variance explained is indicated on each axis.

(I) Biplot of PCA of Evolutionary Coupling and Leiden cluster composition vectors, where each arrow indicates the loading of the feature with respect to the first two principal components. The top 10 features for the first two principal components are shown; arrows are annotated with the feature label. The percent of variance explained is indicated on each axis. Features of the form (x, y) represent Evolutionary Couplings between state x and state y; features of the form x represent the proportion of cells found in Leiden cluster x.

(J and K) Comparison of Phylotime statistics computed using weighted and binary tree branch lengths for (J) Fate Cluster 1 and (K) Fate Cluster 2 (STAR Methods). Correlations are strong for both Fate Clusters (Pearson's correlation = 0.94 and correlation = 0.98, respectively).

(L) Selected Evolutionary Couplings of individual tumors displayed on gene expression UMAP illustrating connections between transcriptional states (Leiden clusters) of interest. From left: the first plot shows the Evolutionary Couplings within a representative tumor in Fate Cluster 1. The second plot shows the Evolutionary Couplings within a representative tumor in Fate Cluster 2. The third plot shows couplings between Fate Cluster 1 (Leiden clusters 3 and 5) and Late-stage transcriptome states (Leiden cluster 9). The fourth plot shows couplings between Fate Cluster 1 (Leiden clusters 3 and 5) and high-fitness transcriptome states (Leiden clusters 7 and 9). The last plot shows couplings between Fate Cluster 1 (Leiden clusters 3, 5, and 14) and high-fitness transcriptome states (Leiden cluster 9 and 13). These results offer evidence of potential transition from early, low fitness to late, high-fitness transcriptome states during tumor evolution.
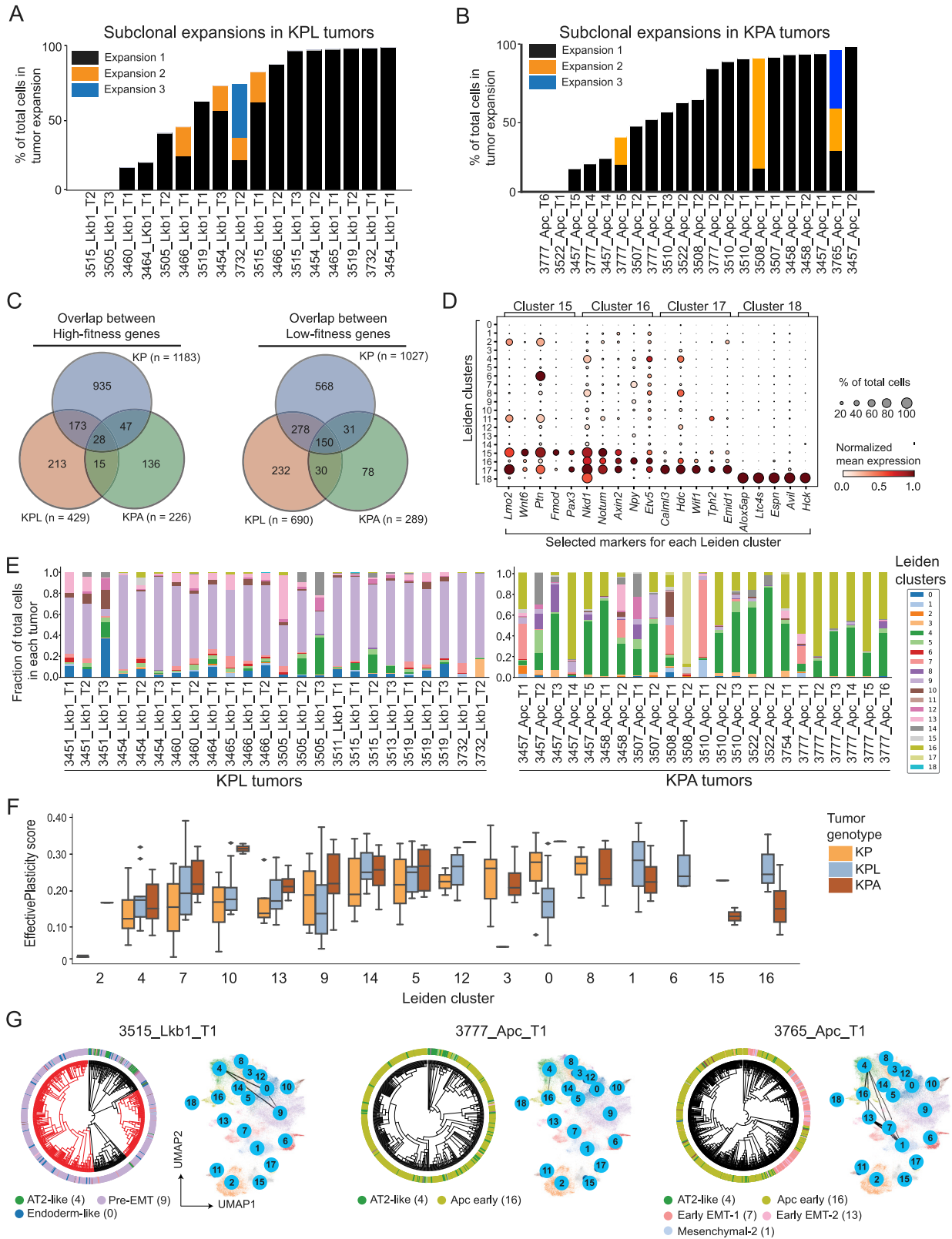
Figure S6. Genetic perturbations shift the transcriptional fitness and plasticity landscape of tumors, related to Figure 6

(A and B) Subclonal expansion dynamics of (A) KPL and (B) KPA tumors. Independent expansions are colored with black, orange, or blue and measured with the percentage of cells in the expanding subclone.

(C) Overlap of genes associated with high and low fitness for KP, KPL, and KPA tumors.

(D) Gene markers for newly identified Leiden clusters in the KP, KPL, and KPA integrated analysis. Dots are sized by the fraction of cells expressing a marker and colored by the mean expression of the gene marker in a Leiden cluster.

(E) Leiden cluster proportions for each KPL (left) and KPA (right) tumor.

(F) Distribution of the mean EffectivePlasticity for each Leiden cluster, averaged within each tumor, compared across genotypes. Leiden clusters 6, 11, 17, and 18 are not shown because they lacked enough tumors across genotypes to make comparisons.

(G) Evolutionary Couplings of different transcriptional states in three representative tumors reveals evolutionary paths in KPL and KPA tumors. Transcriptional states that are represented by at least 2.5% of cells in each tumor are used. 3515_Lkb1_T1 is a representative KPL tumor. The left plot shows the lineage relationship of transcriptional states in this KPL tumor and the right plot summarizes Evolutionary Couplings on the gene expression UMAP illustrating connections between Leiden clusters 4, 0 and 9. 3777_Apc_T1 is a representative KPA tumor. The left plot shows the lineage relationship of transcriptional states in this KPL tumor, and the right plot summarizes Evolutionary Couplings on the gene expression UMAP illustrating connections between Leiden clusters 4 and 16. 3765_Apc_T1 is another representative KPA tumor. The left plot shows the lineage relationship of transcriptional states in this KPL tumor, and the right plot summarizes Evolutionary Couplings on the gene expression UMAP illustrating connections between Leiden clusters 4, 16, 13, 7, and 1.
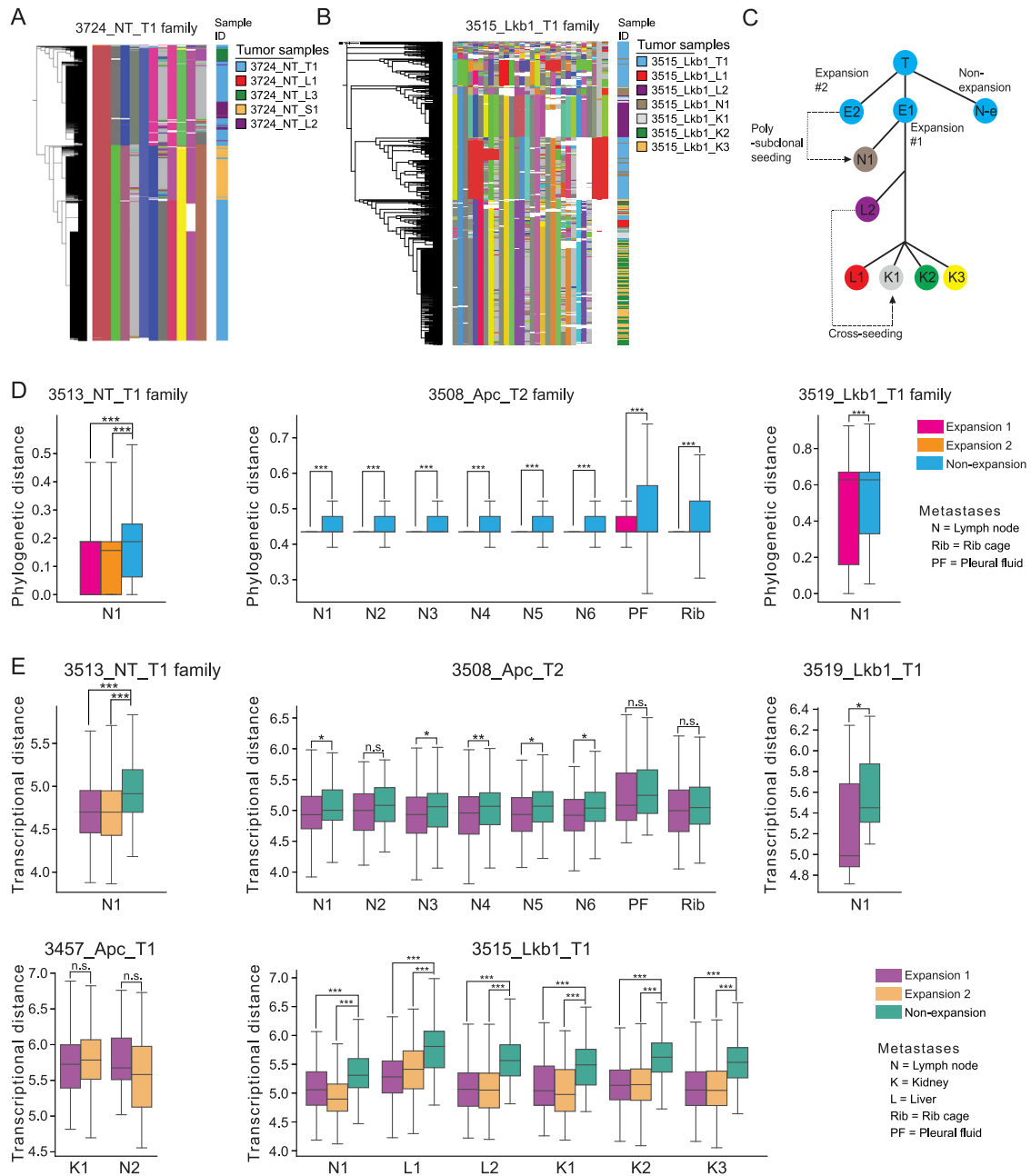
Figure S7. Lineage tracing illuminates the metastatic routes and origins, related to Figure 7

(A) Lineage indel heatmap of the 3724_NT_T1 tumor-metastasis family, summarizing the allelic information (indels) from the target sites confirming the separate origin of the soft tissue and liver metastatic tumors. In the lineage indel heatmap, each row represents a single cell, and each column represents a cut site of the lineage tracer. Unique indels are shown in unique colors, uncut target sites are indicated in gray, and missing data are indicated in white. The reconstructed lineage based on the accumulated indel patterns using Cassiopeia are shown on the left. The corresponding sample ID for each cell is labeled on the right.

(B and C) Subclonal origin and the metastatic routes for 3515_Lkb1_T1 tumor-metastasis family.

(B) Lineage indel heatmap of 3515_Lkb1_T1 tumor-metastasis family, indicating indel alleles supporting the subclonal origins, the relative order, and the routes of metastases, and (C) a model summarizing these metastatic behaviors.

(D) More supporting examples of expanding subclones giving rise to metastases across genotypes for 3513_NT_T1 (left), 3508_Apc_T2 (center), and 3519_Lkb1_T1 (right).

(E) Comparison of transcriptional distance between metastatic tumors and cells in nonexpanding and expanding regions of the primary tumor phylogeny for 3513_NT_T1, 3508_Apc_T2, 3519_Lkb1_T1, 3457_Apc_T1, and 3515_Lkb1_T1 metastasis families. All significances are indicated from a one-sided Mann-Whitney U test: *** indicates $p < 0.001$, ** indicates $p < 0.01$, and * indicates $p < 0.05$.